HyperJet Fusion Corporation

Final Scientific/Technical Report

Plasma Guns for Magnetized Fuel Targets for PJMIF

DOE Grant Number DE-AR0001236

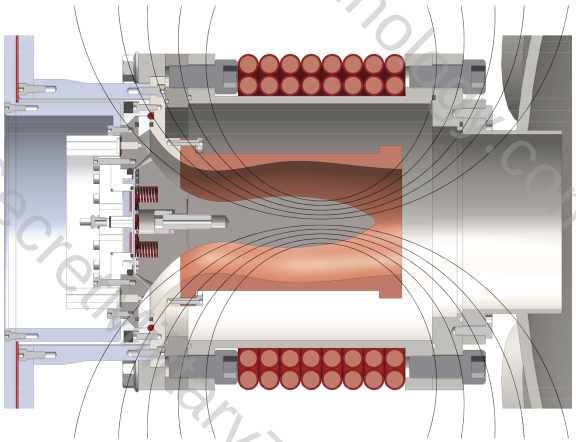

Award:	DE-AR0001236
Sponsoring Agency:	USDOE, Advanced Research Projects Agency - Energy (ARPA-E)
Lead Recipient:	HyperJet Fusion Corporation
Project Team Members:	HyperJet Fusion Corporation
Project Title:	Plasma Guns for Magnetized Fuel Targets for PJMIF
Program Director:	Dr. Robert Ledoux
Principal Investigator:	Dr. F. Douglas Witherspoon
Contract Administrator:	Erin Gilley
Date of Report:	04/21/2021
Reporting Period:	03/27/2020 - 03/26/2021

The information, data, or work presented herein was funded in part by the Advanced Research Projects Agency-Energy (ARPA-E), U.S. Department of Energy, under Award Number DE-AR0001236. The views and opinions of authors expressed herein do not necessarily state or reflect those of the United States Government or any agency thereof.

☒ This Report contains no Protected Data.

Contents

1 Table of Figures/Tables

2 Public Executive Summary

In plasma jet driven magneto-inertial fusion (PJMIF) an array of discrete supersonic plasma jets is used to form a spherically imploding plasma liner, which then compresses a magnetized plasma target to fusion conditions. With funding from ARPA-E's ALPHA program and from Strong Atomics LLC, HyperJet Fusion Corp and HyperV Technologies Corp. previously developed the plasma guns required for an experimental demonstration of the plasma liner formation part of the concept. A 36-gun demonstration of an imploding spherical plasma liner is currently underway on the PLX facility at Los Alamos National Laboratory. This present project addresses the next step required for a complete PJMIF concept, i.e. developing the magnetized plasma target. We proposed to form the target by stagnating a number of magnetized plasma jets in the center of the target chamber. This is accomplished by adding a bias field coil to the plasma liner gun to form a magnetized plasma jet. This experimental development took place at HyperJet in a geometry replicating the bias field environment that will be seen on a PLX port so the results are directly transferrable to the PLX experiment. The objective of this effort was the technical development and characterization of a new magnetized plasma jet using a high-performance, high momentum flux, contoured-gap coaxial plasma gun appropriate for use on the next stage of the PLX experiment.

Electromagnetic modeling of the coil indicated the coil was best placed around the aluminum tubes of the gun transmission line, rather than around the chamber port as originally proposed. This maximized field strength in the breech and yielded much better flux linkage between gun electrodes. A 30-turn coil was ultimately implemented, allowing long pulses that could diffuse through the metal walls on the timescale of interest. MACH2 modeling predicted that less capacitance in the main PFN could potentially improve plasma jet velocities due to better matching of the current to the smaller plasma mass and the existing electrode contour designed to suppress blowby. This proved true, as testing showed markedly improved performance when the original $600\mu F$ bank was reduced to $400\mu F$. A number of diagnostics were built and/or upgraded in order to characterize the plasma jets, inluding laser interferomtery for density, photodiodes for velocity, Bdot probes for magnetic field measurements, a Triple probe for temperature measurements, and spectroscopy for impurity content.

A plasma gun with the 30-turn magnet coil installed, a 70% reduction in gas valve plenum volume, and a 33% reduction in main PFN capacitance produced a dense, high velocity, well magnetized plasma jet. We met or exceeded virtually all of the plasma jet parameter goals. Peak velocity of 135km/s exceeded the 100km/s goal by 35%, while the peak density of over $1.0 \times 10^{15}\text{cm}^{-3}$ was 3.3 times the goal of $> 3.0 \times 10^{14}\text{cm}^{-3}$. Shot-to-shot repeatability is excellent, with a jitter of less than 300ns observed on the arrival fronts of the photodiode signals from one shot to the next. Average plasma jet lengths of 33cm (at 120km/s) were slightly longer than the 20cm goal, but jets as short as 11.8cm were observed at 135km/s. Mass is much higher than the targeted goal, averaging $106\mu g$ per shot compared to $20\mu g$. The magnetic field is still a bit lower than desired, with a maximum to date of ∼811G, compared to the goal of 1000G. Average values, though, were typically in the 300-450G range, when measured further downstream after some expected in flight decay. Temperature measurements are still a work in progress. Increasing the B field and completing temperature measurements will be continued on into the ongoing BETHE project.

3 Acknowledgments

We would like to thank Dr. Robert Ledoux and Dr. Colleen Nehl for many programmatic and technical discussions that helped to make this project a success. We appreciate their intense interest and support of this project. We would also especially like to acknowledge and thank Dr. Samuel Langendorf, Principal Investigator of the BETHE project at Los Alamos National Laboratory, who has been instrumental in keeping us focused and encouraging us onwards during a difficult year. His technical insights and advice have been extremely helpful during weekly and other Zoom meetings. Finally, we would like to thank ARPA-E for its financial support of this project.

4 Accomplishments and Objectives

The main objective was to design, build, and test a magnetized jet with the parameters listed in Table 1 under Milestone 2. We did that and we met or exceeded all those parameters except the B field, which is lower than desired at present, and we still need to make a temperature measurement to confirm we reached the 5eV goal.

Table 1 *Key Milestones and Deliverables*

Key Milestones	**Achieved**
Milestone 1 (go/no-go at 6 months): Demonstrate operational magnetized jet	 Successfully demonstrated magnetized jet
Milestone 2 (at end of SEED project): Magnetized jet parameter goals:	 Magnetized jet parameters achieved:
Velocity >100 km/s	135 km/s
Density $>3 \times 10^{14}$ cm^{-3}	$>1 \times 10^{15}$ cm^{-3}
Mass $>20\mu g$	$>100\mu g$
Length Scale ∼20 cm	11.8 cm (typ 12-30 cm)
B_{jet} ∼1000G	811G (typ 300-450G further downstream)
Temperature >5eV	Measurement is still in progress

5 Project Activities

In plasma jet driven magneto-inertial fusion (PJMIF) an array of discrete supersonic plasma jets is used to form a spherically imploding plasma liner, which then compresses a magnetized plasma target to fusion conditions. This SEED project focuses on initial development of the magnetized plasma jets needed to form the target. The magnetized plasma jets are generated by adding a magnetizing coil to the exterior of the existing plasma liner guns previously developed on the ALPHA program. The coil position, geometry, and driving circuit parameters were developed using EMS electromagnetic modeling software coupled with SolidWorks and bench testing. Three experimental campaigns were performed making diagnostic measurements to confirm the magnetized plasma jets met the desired performance specs. MACH2 modeling indicated that a reduced capacitance pfn would match better to the existing electrode contour and the accelerated mass, and this was confirmed by testing. With the better matched pfn, the spec for density was exceeded by a factor of about four to $> 1.0 \times 10^{15}\text{cm}^{-3}$, velocity of 135 km/s exceeded the 100 km/s goal, the observed mass of $100\mu g$ exceeded the goal of $>20\mu g$, the length range of typically 12-30 cm matched the desired 20cm length (with a best value of 11.8cm), and the maximum observed embedded jet magnetic field of 811G came close to the goal of 1000G, although more typical values were in the range 300-450G. Temperature measurements are still in progress to determine if we met the 5eV goal. A more extensive final technical report has also been prepared which more fully documents project activities and results.

6 Project Outputs

A. Journal Articles
None yet

B. Papers
None yet

C. Status Reports
Quarterly Reports were submitted through ePic.

D. Media Reports
None yet

E. Invention Disclosures
None yet

F. Patent Applications/Issued Patents
None yet

G. Licensed Technologies
None yet

H. Networks/Collaborations Fostered
Los Alamos National Laboratory

I. Websites Featuring Project Work Results
None yet

J. Other Products (e.g. Databases, Physical Collections, Audio/Video, Software, Models, Educational Aids or Curricula, Equipment or Instruments)
None

K. Awards, Prizes, and Recognition
None yet

7 Follow-On Funding

BETHE project "*Target Formation and Integrated Experiments for Plasma-Jet Driven Magneto-Inertial Fusion*" (award DE-AR0001268) is in collaboration with Los Alamos National Laboratory, the University of Alabama - Huntsville, and the University of New Mexico.

Table 2 *Follow-On Funding Received*

Source	Funds Committed or Received
ARPA-E DE-AR0001268	$2,738,034

DOE Grant Number DE-AR0001236

Plasma Guns for Magnetized Fuel Targets for PJMIF

An ARPA-E SEED Project

Final Technical Report
Extended Version

21 April 2021

Prepared for the United States
Department of Energy
Advanced Research Projects Agency - Energy

Edward Cruz, Andrew Case, F. Douglas Witherspoon (PI)
Adam Cook, Marco Luna, Robert Becker

HyperJet Fusion Corporation
Chantilly, VA 20151

The information, data, or work presented herein was funded in part by the Advanced Research Projects Agency-Energy (ARPA-E), U.S. Department of Energy, under Award Number DE-AR0001236. The views and opinions of authors expressed herein do not necessarily state or reflect those of the United States Government or any agency thereof.

Contents

1 Introduction

In plasma jet driven magneto-inertial fusion (PJMIF)[1, 2] an array of discrete supersonic plasma jets is used to form a spherically imploding plasma liner, which then compresses a magnetized plasma target to fusion conditions. With funding from ARPA-E's ALPHA program and from Strong Atomics LLC, HyperJet Fusion Corp. and HyperV Technologies Corp. have been developing the plasma guns required for an experimental demonstration of the plasma liner formation part of the concept[3]. A 36-gun demonstration of an imploding spherical plasma liner is currently underway on the PLX facility at Los Alamos National Laboratory (LANL). We proposed to begin addressing the next step required for a complete PJMIF concept, i.e. developing the magnetized plasma target. We proposed to form the target by stagnating a number of magnetized plasma jets in the center of the target chamber, and to accomplish this by adapting the previously developed plasma liner gun to form a magnetized plasma jet by adding a bias field coil to the gun, as illustrated in Figure 1. This experimental development took place at HyperJet in a geometry properly simulating the bias field environment that will be seen on a PLX port so the results are directly transferrable to the PLX experiment. The objective of this proposed effort was the technical development and experimental characterization of a new magnetized plasma jet using a high-performance, high momentum flux, compact contoured-gap coaxial plasma gun appropriate for use on the next stage of the PLX experiment.

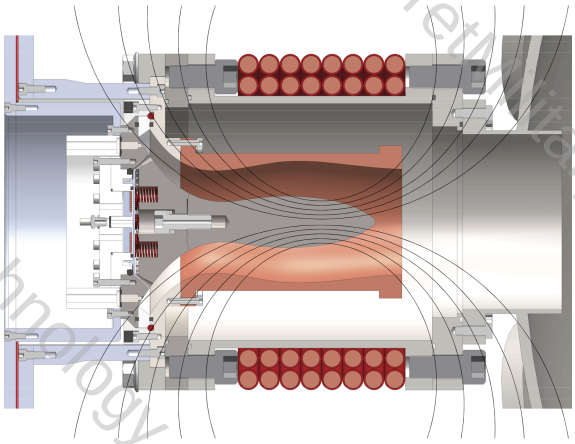

Figure 1 *HJ1 gun with added bias coil so flux links both electrodes. Field lines shown are only illustrative.*

2 Background

2.1 Problem and Proposed Solution

For magneto-inertial fusion (MIF) approaches to be successful, both a suitable liner and target are required. We have made substantial progress in understanding and demonstrating liner formation[3, 4] and now the central challenge we face is the formation of a suitable magnetized plasma target. The target must necessarily be a dense magnetized DT plasma, that can be repetitively formed at the center of a large vacuum chamber. A desirable target behavior is obtained when the plasma electron and ion Hall parameters $\gg 1$ and thus thermal conduction losses from the target are reduced in the cross-field direction, but the plasma beta is also >1 and thus the thermal pressure of the plasma dominates the global stability of the target rather than the magnetic pressure. In this latter way the risk of magnetohydrodynamic (MHD) instabilities leading to a catastrophic loss of confinement is sidestepped, being replaced instead with the risks of hydrodynamic instabilities, which have

historically been survivable at modest convergence ratios[5]. These target criteria are met in the recent successful high-performance MagLIF implosions performed at Sandia National Laboratories, where an axial magnetic field is used owing to the long aspect ratio (axial length over diameter) of the target and achieved multi-keV temperatures, high neutron yields, and thermonuclear burn conditions[6]. For a spherical implosion which has unity aspect ratio by definition, another topology is likely needed to provide similar reduction of thermal losses. Multiple options have been considered, including configurations with closed field lines such as spheromak or field-reversed-configuration (FRC) topologies, or open-field-line configurations in which the field lines become tangled enough to impede electron heat conduction[6].

The requirement for the target to exist at high beta in the center of a large target chamber leads to the idea that the target plasma must be transiently formed, e.g. injected into the chamber ahead of the heavy liner which will do the compression and primary heating. This leads to the idea of using a subset of the guns / injectors to dynamically form the target "just in time" ahead of the liner. To achieve the magnetization of the target, a "stuffing" magnetic flux can be established in the gun via external solenoid coils, enabling them to operate in a similar manner to traditional spheromak guns[8, 9]. The amount of initial magnetic flux present in the gun determines degree of magnetization of the resulting jet, with the limit of high initial stuffing flux leading to the formation of a detached low-beta spheromak. Operation at this low beta may not be advantageous for the ultimate compression as it may increase the chance for MHD instabilities to disrupt the global confinement in the target. Ultimately, simulations and experiments are required to explore this area of transient magnetized target formation to identify if and how a suitable target can be formed, and what its confinement characteristics may be when compressed by the heavy liner.

2.2 State of the Art and the Technical Approach

In this effort, we planned to develop and experimentally characterize magnetized plasma jets using modified versions of our existing plasma guns. The existing HJ1 gun[1] designed and produced by HyperJet/HyperV are the state of the art for high mass, high momentum flux plasma guns. These guns have been used to form small sections of a liner and perform jet merging studies on the PLX facility at LANL[3]. This work was performed under the ARPA-E ALPHA program with additional funding from Strong Atomics LLC. With the installation of 36 plasma guns on PLX, work is currently underway by Dr. Sam Langendorf and his team at Los Alamos National Laboratory performing the first ever demonstration of an imploding fully formed spherical plasma liner with parameters ultimately applicable to a fusion experiment. The LANL/HyperV/HyperJet ALPHA collaboration is expected to generate a spherical liner and obtain experimental data on that liner. This present project will provide the magnetized plasma target for that envisioned liner-on-target integrated experiment which is the goal of the BETHE project.

The basic physics for a magnetized target via magnetized jets have been described in detail in the paper by Hsu and Langendorf[7]. Table 1 details the required jet parameters which are our target. This program is a first step towards experimentally developing such jets.

The basic idea is to add a solenoidal bias field[11, 12] to the already high-performance plasma liner guns to produce a magnetized plasma jet with high velocity and mass (momen-

Table 1 *Plasma parameters for proposed near-term target formation experiments and simulations.*

		Magnetized jets in flight	Merged magnetized jets
Electron Temperature	T_e(eV)	5	25
Ion Temperature	T_i(eV)	5	25
Number Density	n(cm^{-3})	3.00E+14	3.00E+16
Velocity	v ($cm/\mu s$)	10	1
Length Scale	Lm (cm)	20	40
Ion Charge State	Z( )	1	1
Ion Mass Ratio	μ ( )	1	1
Magnetic Field	B(G)	1000	5000

tum). This is illustrated conceptually in Figure 1. The plasma gun is mounted re-entrantly inside a port on the PLX vacuum chamber. For the magnetized jet, we envisioned winding a coil around the port as shown to form the solenoidal magnetic field. The pulse width for the coil current needed to be sufficiently long so that the field "soaks" through the metal and is essentially static during the time of the much shorter plasma jet duration. Since the port structure at HyperJet is slightly different from that on PLX, we duplicated the PLX port by mounting the gun inside an extended port tube with the same thickness and geometry as the PLX port. The innovation in this project is in demonstrating formation of a magnetized plasma jet in a high performance (high momentum flux) compact contoured-gap coaxial gun and determining the optimal operating configuration to achieve the parameters listed above. This had not been achieved before and is critical for the successful formation of a magnetized target plasma needed for the PJMIF concept.

There are currently two main approaches under consideration for forming a magnetized plasma target appropriate for PJMIF. One is to produce an imploding target plasma with an embedded magnetic field produced directly within the plasma guns themselves. The second is to generate a magnetic field in a target plasma by the use of laser beat wave driven currents in the target plasma. Here we propose to address only the first case as being the simpler and more direct.

We leverage the use of an existing spare HJ1 gun for this developmental effort. We also have seven additional operational Alpha2guns (a previous gun design of comparable parameters) which could be pressed into service if the need arises. The electrode profile contours are identical. The Alpha2guns would only need the gas valve upgraded to the latest drop-in version and the original capillary ignitor array replace by the simpler GPI circuit. Reusing existing hardware will save a great deal of time and funds.

Following the discussion in Bellan's book Spheromaks [13], compact toroids (CT) are a class of magnetized plasma with toroidal configurations that are self-stable on time-scales relevant to fusion. The spheromak and field-reversed configuration (FRC) are the most well understood CT configurations and have the greatest potential as fusion targets. The main difference is that the spheromak contains poloidal and toroidal magnetic fields, while the FRC has only the poloidal fields. The FRC has naturally higher β, but requires an external magnet for confinement. The spheromak has shown greater confinement times and temperatures, and thus greater overall potential as a viable target for PJMIF. Spheromaks

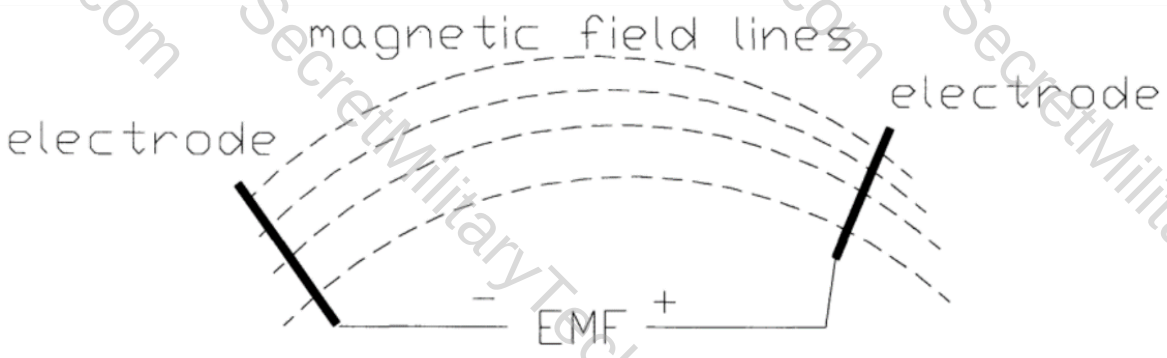

Fig.7.1 Generic spheromak formation scheme: An EMF applied along field lines drives field-aligned current, or equivalently, injects magnetic helicity. When the ratio of field-aligned current to intercepted flux exceeds a threshold, closed field lines are formed, i.e., a spheromak-like configuration is created.

Figure 2 *Figure is from Chapter 7 of Bellan's book "Spheromaks" [13].*

are commonly produced by coaxial plasma guns, which HyperJet has experience developing and manufacturing. FRC's can be formed and accelerated entirely inductively, eliminating any potential contamination from electrodes, which could be advantageous later.

Common among all spheromak formation schemes is that field-aligned plasma current is driven by a field-aligned EMF. As plasma current increases, it remains in a force-free equilibria with the magnetic field according to $\nabla \times B = \lambda B$. The net field, B, is then twisted, and it's twist is an increasing function of λ, which scales with the plasma current. If the rate-of-rise of λ is very slow compared to the characteristic Alfven time, then the system evolves through a sequence of relaxed states. All that is essential for spheromak formation is sufficient build-up of λ, which is referred to as helicity injection.

For a coaxial plasma gun configuration, helicity is injected into the plasma at a rate of $2V\Phi$, where V is the voltage applied across the inner and outer electrodes and Φ is the flux linking these electrodes. HyperJet's HJ1 plasma gun may present a distinct advantage by inherently having a voltage applied across the inner and outer electrodes during plasma formation from its glow-like pre-ionization system (GPI). The GPI voltage can be varied from 0 to 5kV, and the GPI circuit inductance can easily be adjusted to control the rate-of-rise of λ. All that is missing is a magnet to provide the linked flux, Φ.

The work plan is therefore centered around designing and installing a bias field coil along with its power supply, and then performing a detailed experimental campaign to study and elucidate the performance of the magnetized jet formed, with diagnostics being key to understanding the observed results.

3 Modeling (Task 1)

3.1 MHD Modeling of Plasma Gun

Direct computational modeling of the plasma gun performance using He, H, and Ar was done in-house using MACH2 [14]. This was needed to fine tune the gun operational envelope and determine the modified PFN for the lower mass required for the magnetized jets. MACH2 is only a 2D axisymmetric MHD code and therefore cannot directly model the formation of a magnetized jet which is a fully 3D configuration. However, MACH2 is capable of modeling the basic underlying jet, which has much larger magnetic fields (>10 times) in the driving armature than that of the externally applied bias field. This allows MACH2 to be a useful tool to provide guidance on setting up the basic jet parameters and determining the optimal capacitance using the existing hardware. Future fully 3D modeling of the magnetized jet is planned to be accomplished during the BETHE program using thr SPHMax code developed by Prof. Jason Cassibry at University of Alabama - Huntsville. Additional 3D modeling of the jet collisions will be performed by Li at Los Alamos National Laboratory under an INFUSE project.

Previous experience with the liner guns showed operation at ∼1 mg at 50-60 km/s at best. Since these present experiments were designed for an order of magnitude less mass, it was necessary to determine what set of current current profile and mass parameters would be required to match to the existing electrode contour. Too much current and or the wrong time profile would likely lead to blowby on either the inside or outside.

Initial MACH2 modeling confirmed that solutions in the parameter range needed actually existed as shown in Figures 3 and 4. The modeling showed that deuterium plasma jets with velocities in the range 100-150 km/s, $1 \times 10^{14}\text{cm}^{-3}$ density, and 100 μg are possible using only 200-300 μF of capacitance in the PFN. This would represent a significant reduction in capacitance compared to the liner guns, which use $600\mu F$. This is mainly due to the lower current required to drive the mass to high velocity. A shorter pulse leads to faster current rise and better matching to the electrode contour, thus suppressing blowby.

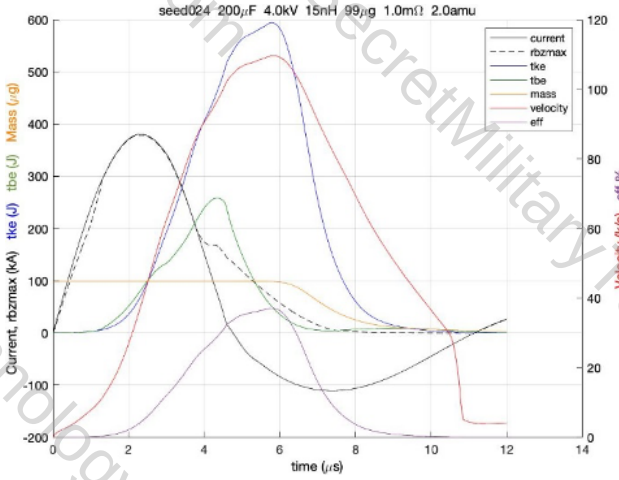

Figure 3 *Representative 200μF case at 4kV.*

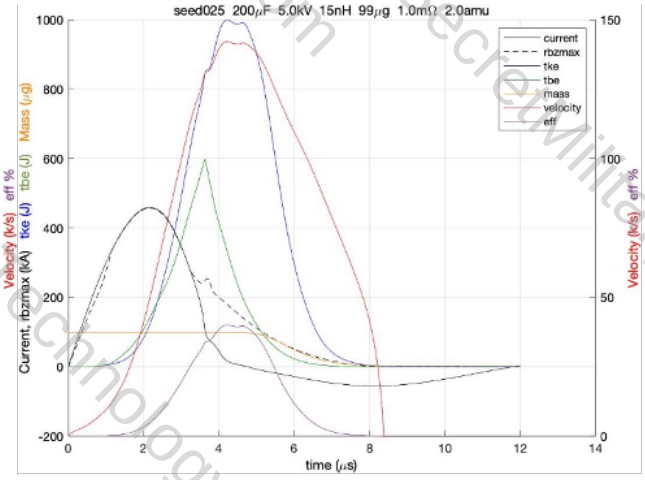

Figure 4 *Representative 200μF case at 5kV.*

As will be described in further detail in Section 6 below, initial experimental testing of the magnetized gun was performed with the already existing $600\mu F$ pfn, which was sufficient for the preliminary stages of testing the magnet coil and diagnostics. Modifying the pfn required some effort, and so we wished to defer that as long as possible to allow time to scan through the performance possibilities with the already existing pfn. This testing revealed that we were indeed making magnetized jets, but the velocities were observed to be low, typically around 70 km/s or so, whereas our goal was greater than 100 km/s.

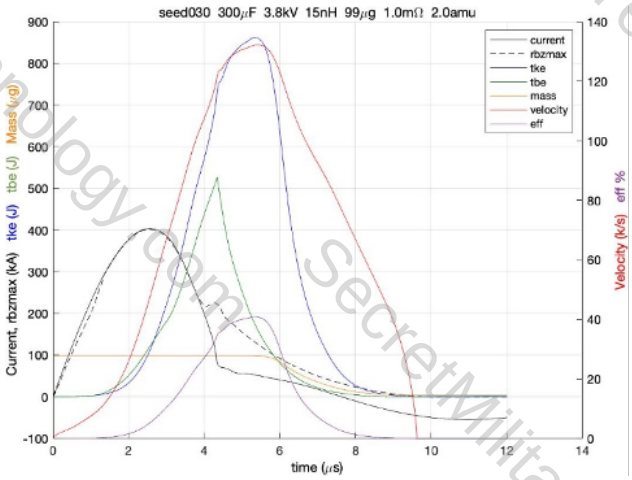

Figure 5 *Representative $300\mu F$ case at 3.8kV.*

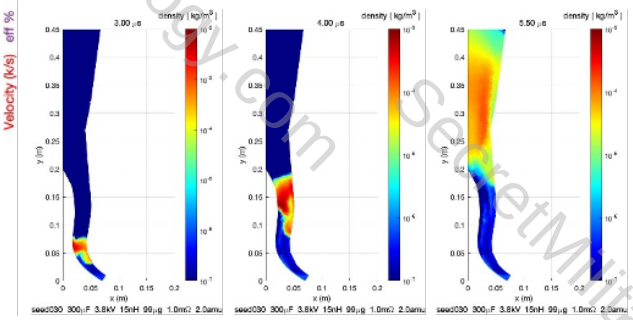

Figure 6 *Density contours for $300\mu F$ case.*

MACH2 modeling had indicated that 200-$300\mu F$ would match the mass and electrode contour better than the $600\mu F$ as seen in the plots of Figures 3, 4 and 5, but unfortunately, the required current exceeded the peak current limitations on each capacitor, limiting the voltage/current at which we could operate.

The solution (see also Section 6.3) was to increase the total capacitance slightly to $400\mu F$ (6 groups of 2 caps), midway between the two extremes of $200\mu F$ and $600\mu F$. Figure 7 shows the resulting performance. At a charging voltage of 4.9kV, this meets the current limitation of 50 kA per capacitor. The experiments confirmed the simulation, showing velocities well over 100 km/s and with densities well above the minimum desired value.

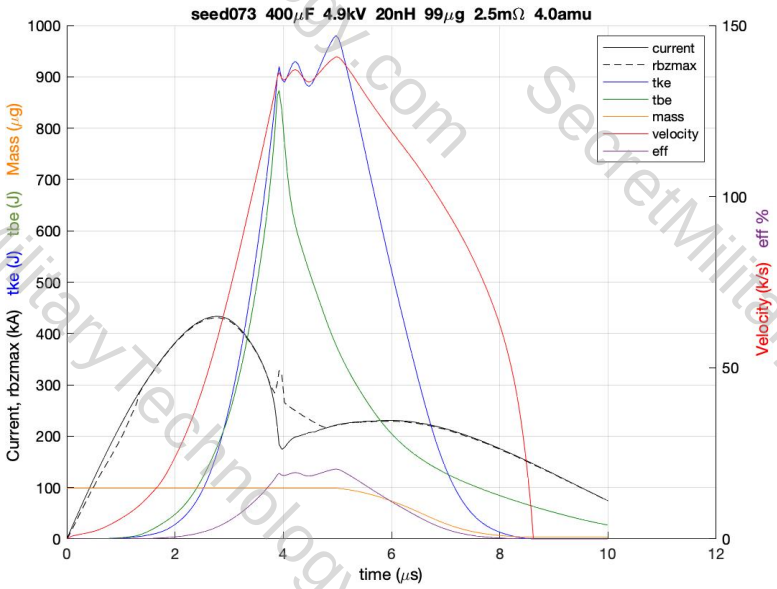

Figure 7 *A $400\mu F$ case using Helium. This performance roughly matches the observed behavior of the magnetized jet.*

3.2 Electromagnetic Modeling of Magnet Bias Coil

Magnetic field modeling of the bias field coil was performed using EMS for SolidWorks. EMS is an electromagnetic field simulation software which calculates fields (electric, magnetic, flux, potential, eddy currents), circuit parameters (inductance, capacitance, resistance, impedance, flux linkage), mechanical parameters (force, torque), and losses (eddy, core, hysteresis, ohmic). EMS was developed by EMWorks and is seamlessly integrated within SolidWorks CAD. In particular, EMS was used to evaluate magnet location, size and energy requirements.

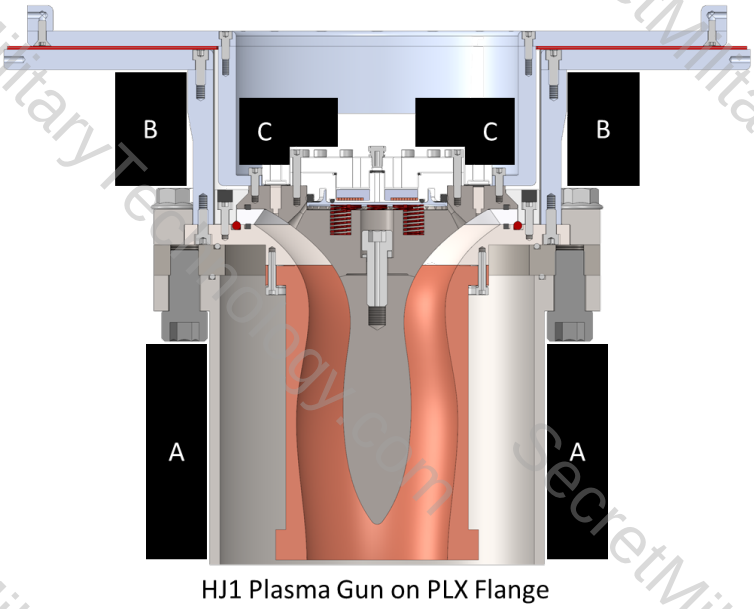

Figure 8 *Possible magnet coil locations. See text for discussion of A, B, and C.*

3.2.1 Coil Location

The first task using EMS was to determine the optimal magnet location. The HJ1 plasma gun has three convenient locations for placing external magnets, identified in Figure 8 as locations A, B and C. Locations A and B allow for a coil wound from flexible cable, using either the gun or flange as a mandrel. Location C is better suited for a rigid coil. The primary goal is to maximize flux linkage between the inner and outer electrodes in the formation region. The formation region corresponds the volume between the inner and outer electrodes around where the gas flows out from the inner electrode, and is referred to as the breech.

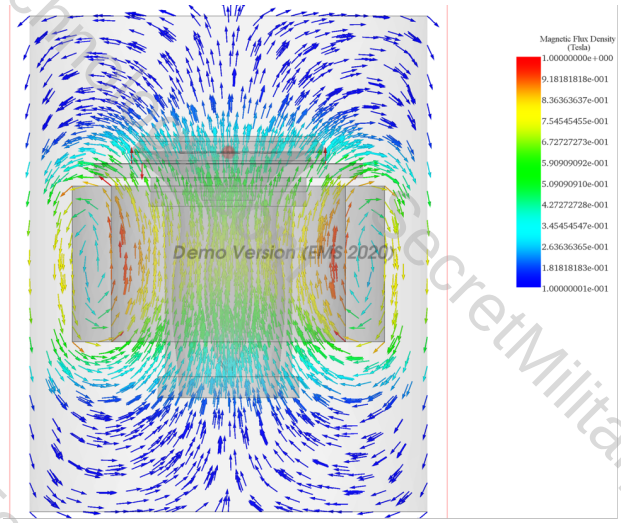

Figure 9 *Static field result from an applied magnet current of 14kA for an 8-axial turn by 2-radial turn coil at Location A.*

Initial steady-state modeling was done with magnets at locations A, B and C to evaluate the merits of each option. Location A was the originally proposed magnet location, and was evaluated with a magnet modeled as an 8-axial turn by 2-radial turn coil wound from 4/0 cable. Static field results for an applied magnet current of 14kA are shown in Figure 9. Overall field intensity is good at ~5kG in the breech, or ~22mG/Amp-turn. Field

orientation is not ideal though, as the perpendicular component linking the inner and outer electrodes in the breech is relatively small compared to the overall field magnitude.

Location B was evaluated with a magnet modeled as a 4-axial turn by 2-radial turn coil wound from 2/0 cable. Static field results for an applied magnet current of 10kA are shown in Figure 10. Overall field intensity is good at ∼2kG in the breech, or ∼25mG/Amp-turn, which is slightly better than location A, which gave ∼22mG/Amp-turn. Field orientation is much improved versus location A, with the field lines more normal to the inner and outer electrodes for significantly improved flux linkage.

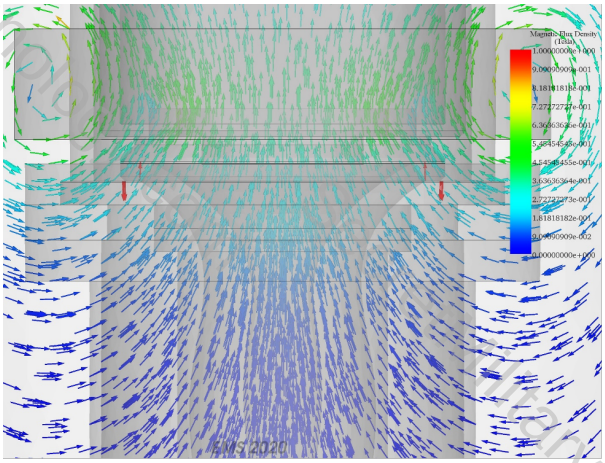

Figure 10 *Static field result from an applied magnet current of 10kA for a 4-axial turn by 2-radial turn coil at Location B.*

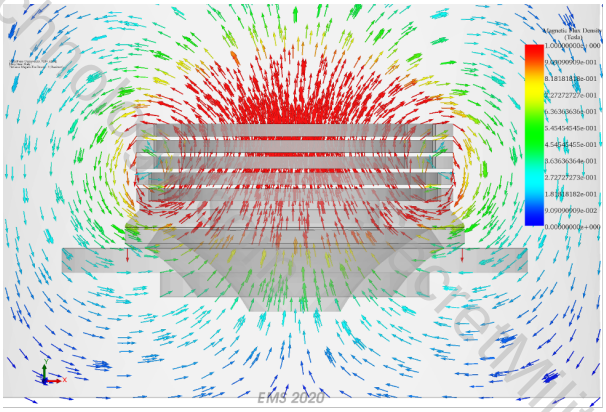

Figure 11 *Static field result from an applied magnet current of 10kA for a two part coil assembly, a lower coil with 2-axial turns by 3-radial turns and an upper coil with 3-axial turns by 6-radial turns, at Location C.*

Location C was evaluated with a magnet modeled as two separate coil assemblies, a lower coil with 2-axial turns by 3-radial turns and an upper coil with 3-axial turns by 6-radial turns. Static field results for an applied magnet current of 10kA are shown in Figure 11. Overall field intensity is good at ∼4kG in the breech, or ∼17mG/Amp-turn, which is somewhat less field in the breech per Amp-turn than locations A or B. Field orientation is as good or better than location B.

Having magnet coils at multiple locations was also evaluated. Static field results from a two-magnet model, with magnets at locations B and C, for an applied magnet current of 10kA are shown in Figure 12. The details of the magnet at each particular location are the same as that of the single magnet models at that location discussed above. Overall field intensity in the breech is >5kG, which is just ok considering how many more Amp-turns are present in this case versus the individual magnet cases discussed above. The magnet at location B alone was giving ∼2kG and the magnet at location C

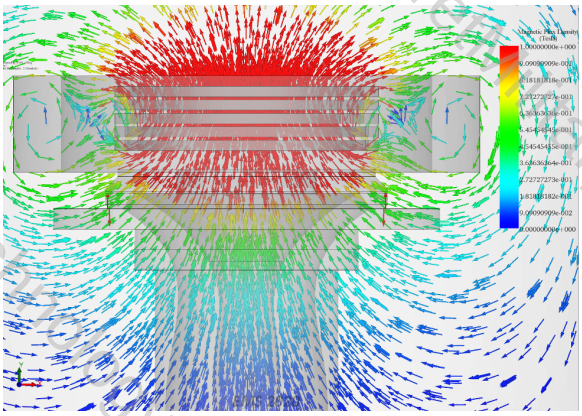

Figure 12 *Static field results from an applied magnet current of 10kA for a two-magnet model, with magnets at locations B and C.*

alone was giving ∼4kG. Field orientation is very good though, with field lines being almost completely normal to the gun electrodes in the breech, providing excellent flux linkage. That being said, field intensity at the center of the combined magnet assembly is very high at ∼40kG, which is undesirable.

The result of this analysis is that a magnet at location B provides the best combination of safety, convenience, field strength and field orientation in the breech. Transient analysis was then done on a simplified gun model to observe the evolution of the field in the breech of the gun. A 15kA, 10ms current pulse was applied to a 4-axial turn by 2-radial turn coil wound from 2/0 cable. Results are shown in Figure 13 at t=5ms, the peak of the current pulse. Figure 14 shows the corresponding flux down the bore of the plasma gun at t=5ms. Overall field intensity is good at ∼3kG in the breech. Field orientation is also good, with the field lines almost directly linking the inner and outer electrodes.

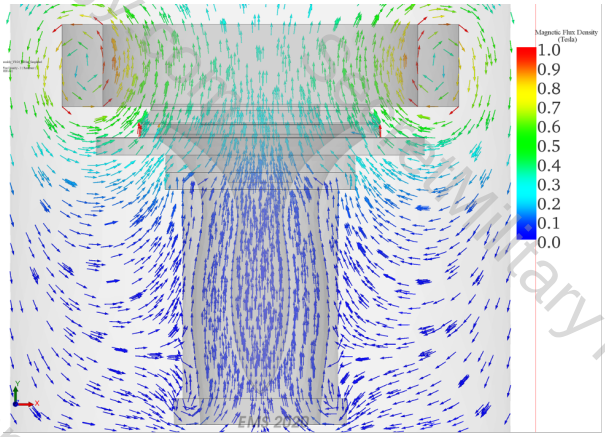

Figure 13 *Transient field results at t=5ms from 15kA, 10ms current pulse for a 4-axial turn by 2-radial turn coil at Location B.*

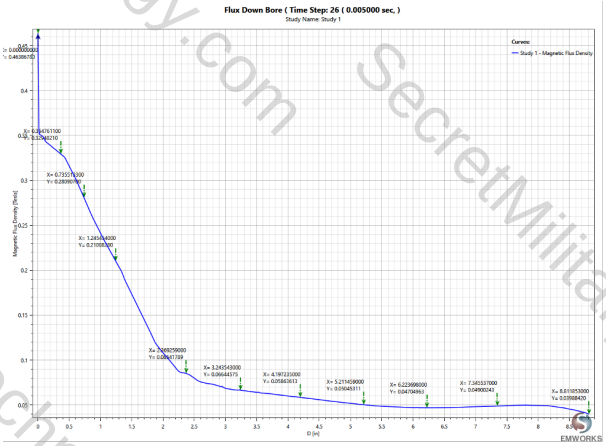

Figure 14 *Flux down bore of plasma gun at t=5ms from 15kA, 10ms current pulse for a 4-axial turn by 2-radial turn coil at Location B.*

3.2.2 Thermal Analysis

Transient thermal analysis was then done to check temperature rise and evaluate what degree of cooling was necessary. Results of transient analysis are shown in Figure 15 and show a negligible temperature rise of 0.15K from resistive losses due to eddy currents. Active cooling will therefore not be required. This led into experiments using a single magnet, passively cooled, wound around the ground tube of the plasma gun assembly, which are discussed below.

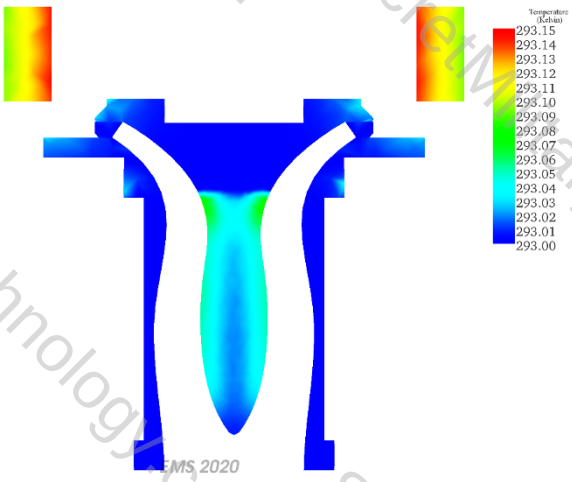

Figure 15 *Temperature rise after 10ms from a 80kA-turn magnet pulse.*

3.2.3 Mesh Analysis

A lot of the preliminary modeling discussed above was done with a coarse mesh with under 100k mesh cells to get results quickly. An evaluation was later done of results from using a coarse mesh (tens of thousands of mesh cells) versus a fine mesh (hundreds of thousands of mesh cells). Coarse versus fine mesh cells for a plasma gun model are shown in Figure 16. Figure 17 shows the dramatic difference of the field orientation and magnitude in the breech early in time. For some reason, the coarse mesh model develops strong field parallel to the gun electrodes in the breech early in time. This is most likely due to an error in the eddy current effects due to the coarse mesh. The orientation and magnitude of the breech field later in time is similar though. A fine mesh will be used in EMS for all modeling data presented in later sections to avoid the nonphysical effects exhibited early in time with a coarse mesh.

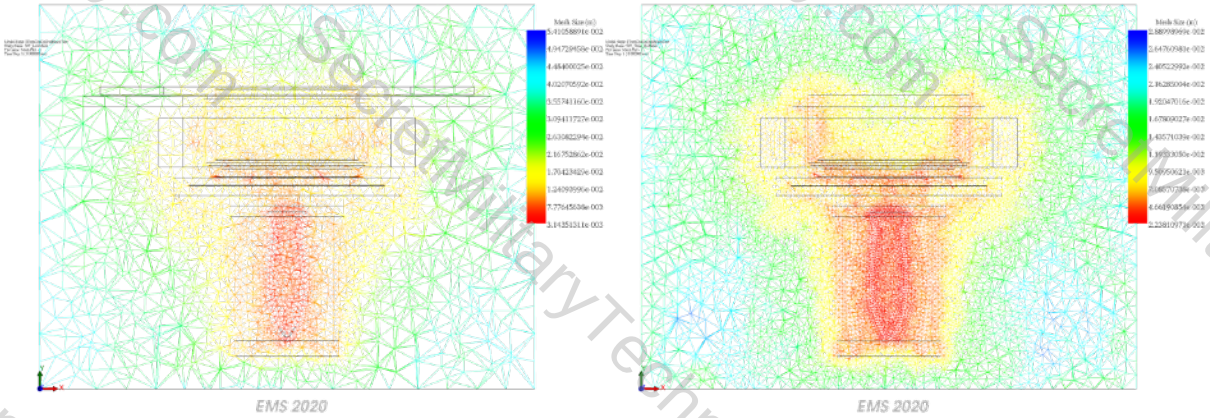

Figure 16 *Coarse (left) vs fine (right) plasma gun model mesh in EMS*

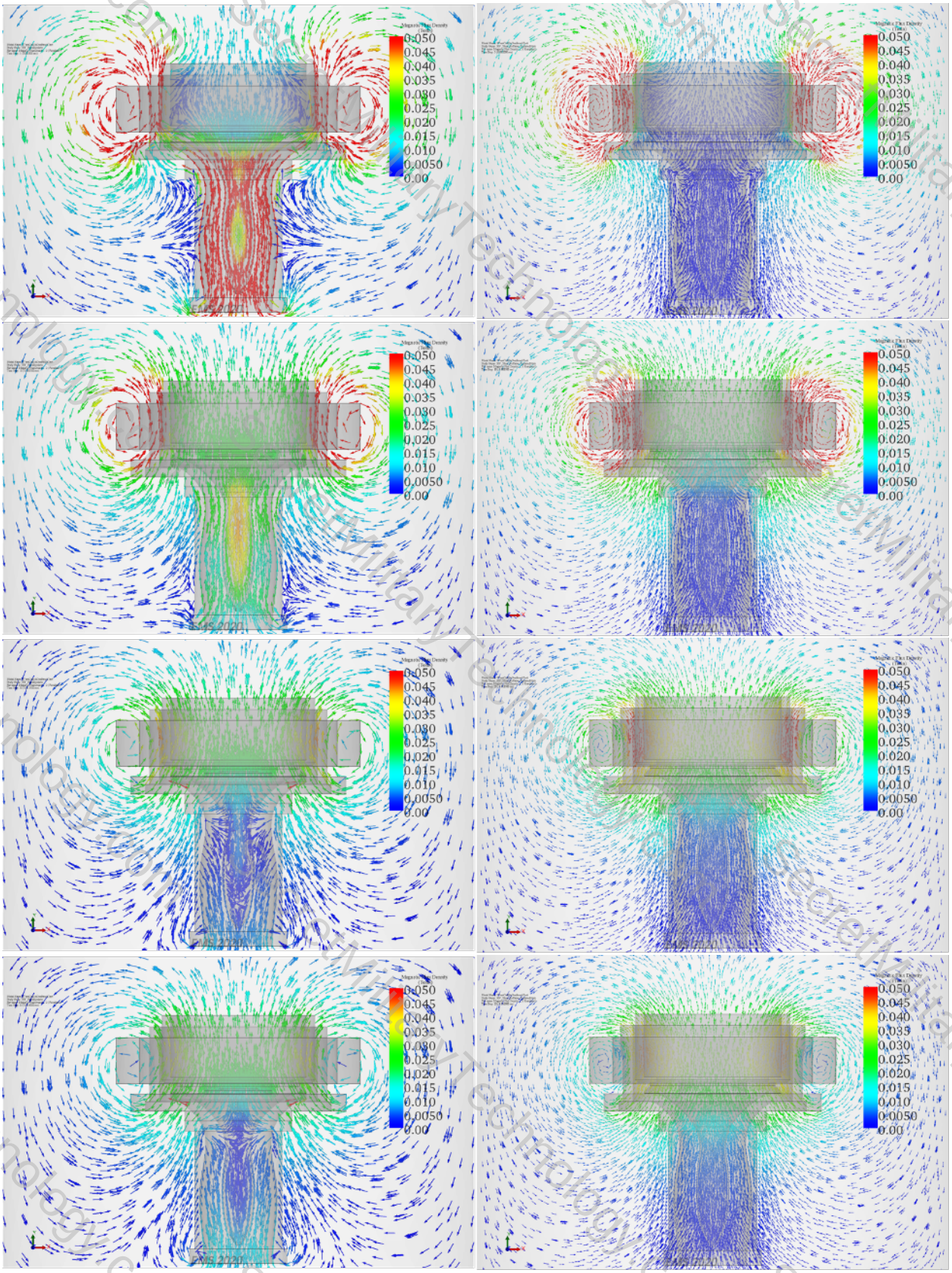

Figure 17 *B-field with coarse mesh (left) vs fine mesh (right) at t=2.0ms, 8.5ms, 13.5ms and 16.0ms.*

3.2.4 Effects on the Gas Valve

The effects of the magnet coil being developed on the gas valve of the gun were also modeled, as there was some concern that the magnetic forces from the coil could have a negative impact on the performance of the gas valve. An 8-turn magnet coil was used to model the magnetic effects on the gas valve, as shown in Figure 18. The magnet coil was placed in relative position to the gas valve coil and flyer plate, which are the gas valve components most susceptible to magnetic forces. Effects were observed from ∼6.5ms long magnet pulses of 5kA and 15kA, shown in Figure 19 for 15kA. Peak field on axis at 15kA was 5.1kG, as shown in Figure 20(a). Peak repulsive force is 4.3N (0.97lbs) at 5kA, where dB/dt= 38.6 T/s, and peak repulsive force is 15.5N (3.5lbs) at 15kA, where dB/dt = 116 T/s. Magnetic force versus time for a 15kA magnet pulse is shown in Figure 20(a). Ultimately the magnetic forces from the bias coil on the gas valve components are small enough to be considered negligible.

Figure 18 *Model used to study magnetic effects of coil on the gas valve from the gun.*

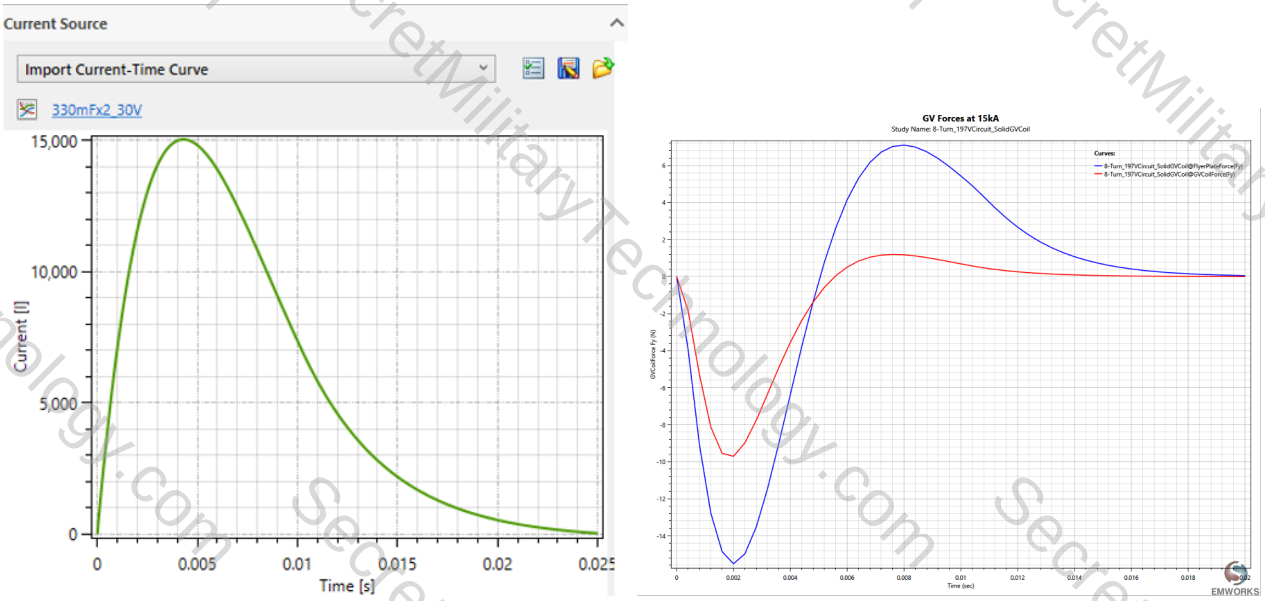

(a) 15kA magnet pulse used to study magnetic effects of coil on the gas valve.

(b) Forces on gas valve components from 15kA magnet pulse.

Figure 19 *Effects on Gas Valve*

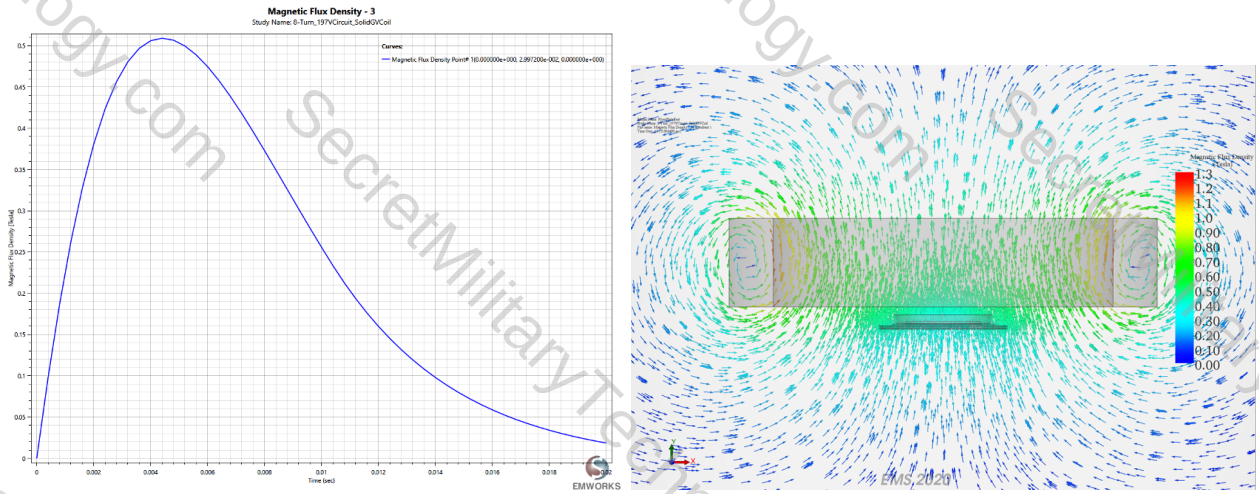

(a) cap1

(b) cap2

Figure 20 *Peak field from 15kA magnet pulse for an 8-turn magnet coil with gas valve flyer plate.*

4 Bias field coil (Task 2)

4.1 Initial Magnet Circuit with 8-Turn Magnet Coil

We have fabricated and mounted a suitable bias coil onto one of our HJ1 plasma guns, as shown earlier in Figure 1. The gun is mounted in a re-entrant manner on our vacuum tank, similar to how it is on the PLX vacuum tank. We chose to wind the bias coil around what is called the ground tube of the HJ1 gun based on electromagnetic modeling. This has the distinct added advantage that all components are external to the vacuum, eliminating costly vacuum power feedthroughs and the non-trivial problem of coil cooling in vacuum, both of which will likely be important for future implementation on PLX. This also provided flexibility in the design process to allow various configurations of the coil length, number turns, operating current, polarity etc. We investigated the efficacy of various coil configurations at the start of the program, looking at both low-turn-count/low-inductance configurations and high-turn-count/high-inductance configurations.

We had several options for driving the bias coil, but we chose to use commercially available electrolytic capacitors, which provided the ideal combination of current capacity, voltage and pulse width needed. Likewise, we went with an SCR circuit to control the long pulse coil current. The initially deployed magnet circuit model is shown in Figure 21(a). Corresponding simulated current and voltage plots from 60V of charge on the capacitors are shown in Figure 21(b). This particular circuit used 2 electrolytic capacitors in parallel, SCR switching, a crowbar diode and positive charging to energize an 8-turn magnet coil. The capacitors were rated for 330mF at 63V, for a total circuit capacitance of 660mF and total circuit energy of 1.3kJ. The SCR was rated for 18.7kA at 1.4kV and the diode was rated for 23kA at 1.8kV.

To test the circuit, semiconductor clamps were necessary for the SCR and diode. The semiconductor clamps were designed and built in-house for this experiment, shown in Figure 22, which allowed for dramatically reduced lead times for a clamp with specific dimensions and load calibration. Development was based on industry standard designs. These clamps used a spring washer system to set the load, along with sleeved bolts to provide the load. Load calibration was performed using precision electronic load cells from Omega.

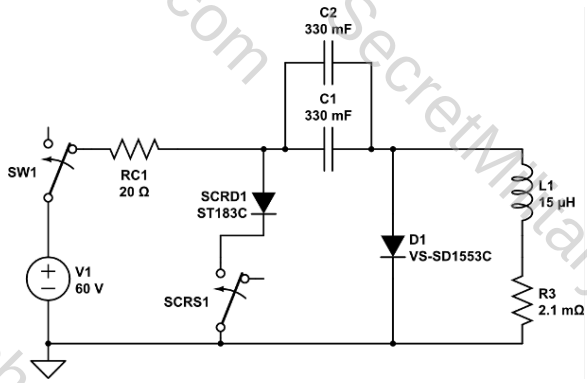

(a) Initially deployed circuit model for 8-turn magnet coil, along with current and voltage from 60V capacitor charge.

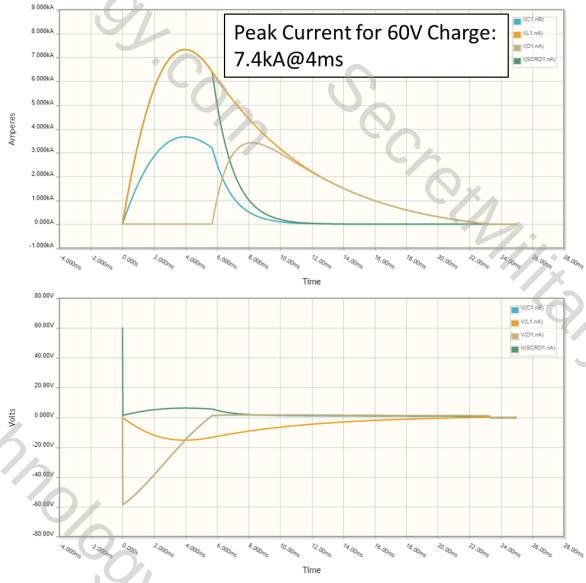

(b) Simulated current and voltage signals from initially deployed circuit model at 60V charge.

Figure 21 *Details of first tested circuit.*

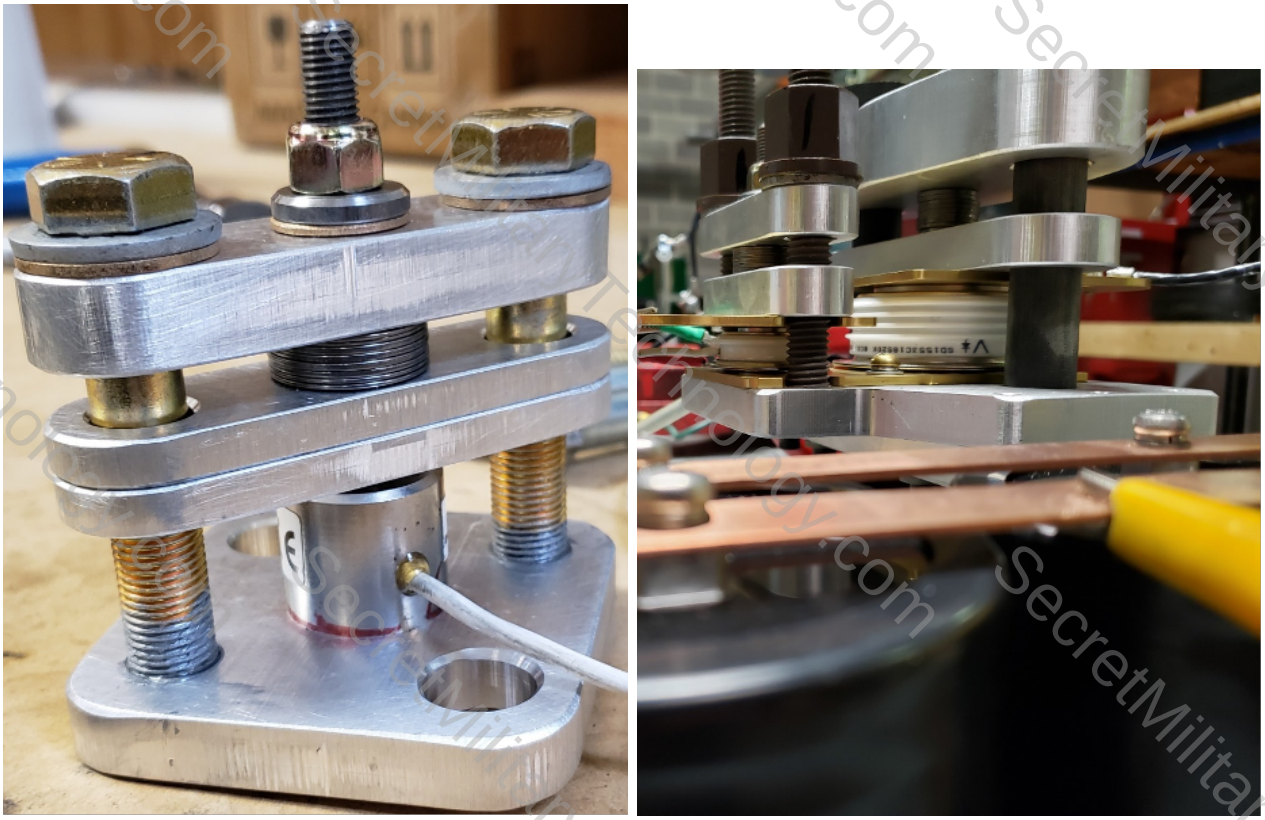

(a) Semiconductor clamp calibration using precision load cell.

(b) Semiconductor clamp deployed and in use with SCR and diode installed.

Figure 22 *Semiconductor clamp system.*

Shakedown testing of the magnet circuit was then performed using a commercially manufactured coil designed for high current, which allowed for circuit validation without the risk of magnet failure that could occur from a hand-wound coil, as shown in Figure 23. The commercial coils used had a total inductance of $386\mu H$ and resistance of $47.5m\Omega$. Although resistance and inductance are high, they are close enough to the ranges of interest to provide a good testo the magnet circuit. Low current test results are shown in Figure 24 and show very good agreement with SPICE simulations.

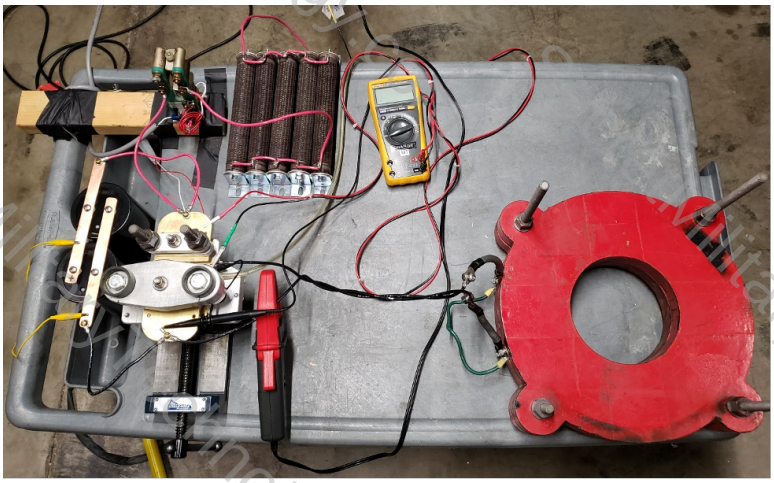

Figure 23 *Bench testing setup for initial magnet circuit with commercially manufactured coils.*

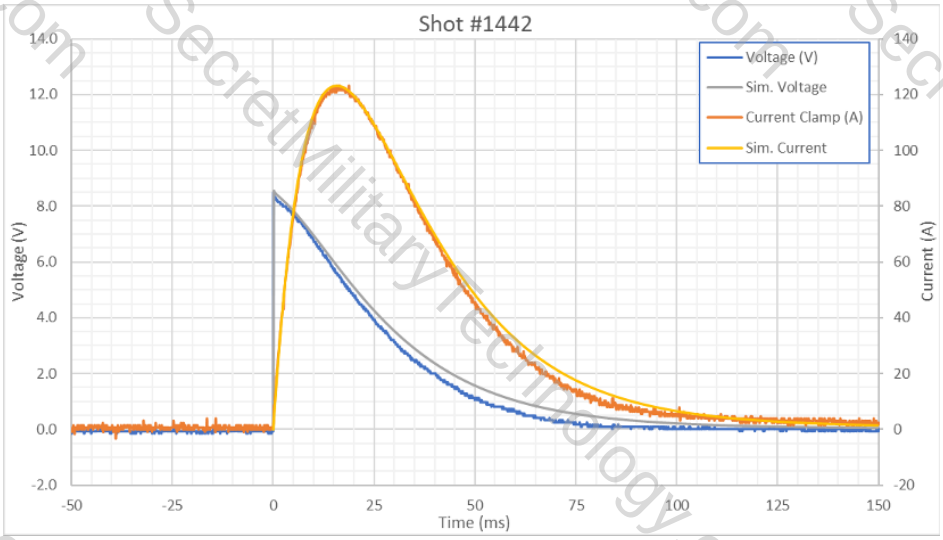

Figure 24 *Sample test results from initial circuit with commercially manufactured coils*

Further bench testing was performed with an 8-turn magnet coil wound from 2/0 THHN stranded building cable, shown in Figure 25. This particular cable was chosen because it provided the best combination of size and strength, but with limited flexibility, as a result of using much heavier gauge strands than standard welding cable. THHN cable is stiff and hard to wind, requiring a rigid winding jig mounted to a lathe. The winding jig is shown in Figure 26 along with 4- and 8-turn coils that were wound using it.

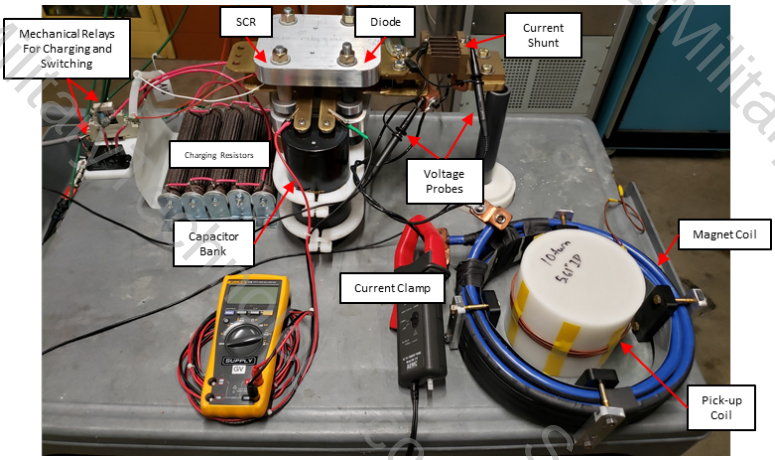

Figure 25 *Bench testing setup for initial magnet circuit with 8-turn magnet coil.*

Figure 26 *(Left) Winding jig used to fabricate initial test coils. (Center) 4-turn test coil wound from 2/0 THHN cable. (Right) 8-turn test coil would from 2/0 THHN cable.*

For initial testing, plastic and metal plates were bolted together to use as clamps to prevent the coils from unraveling from magnetic forces. In-house designed and built semiconductor clamps with integrated transmission line were used for the SCR and diode. Total circuit inductance and resistance were measured to be $22.8\mu H$ and $5.23m\Omega$, respectively. Measured magnetic field and magnet current are shown in Figure 27 and Figure 28 for two different capacitor charge voltages. These data show good agreement with EMS and SPICE simulations. A clamp on current meter was initially used to measure the magnet current, but was limited with a peak current rating of 1.5kA. A $75\mu\Omega$ shunt was later added to the magnet circuit to better measure higher currents.

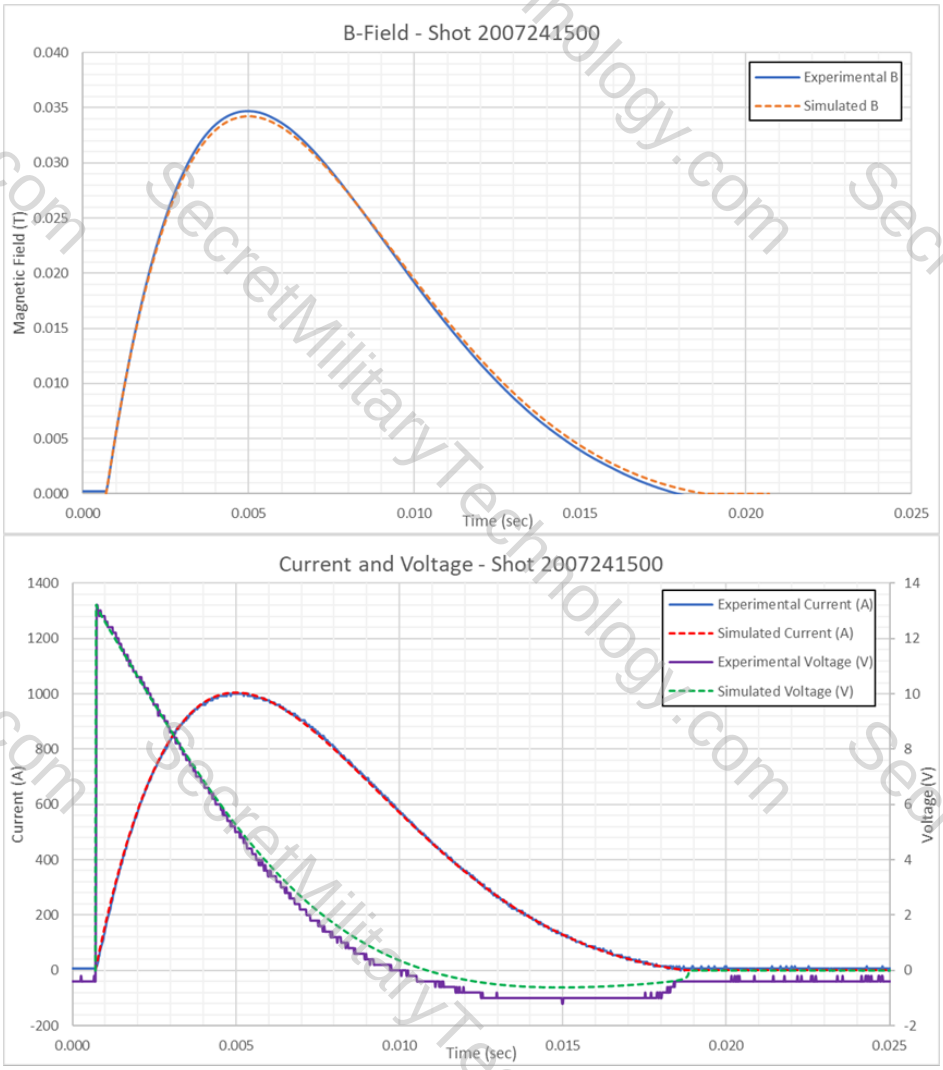

Figure 27 *Simulated vs experimental data from 1.0kA magnet pulse for 8-turn magnet coil. (Top) Magnetic field data. (Bottom) Corresponding current and voltage data.*

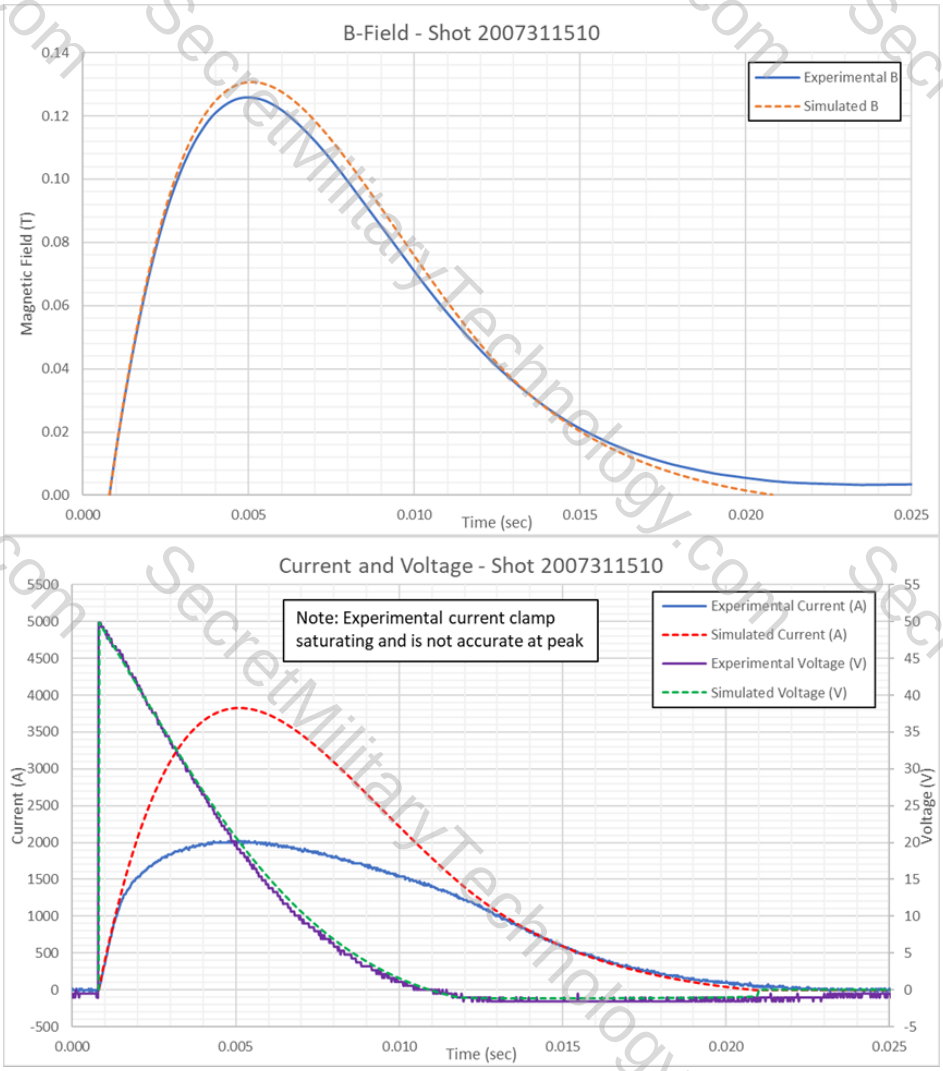

Figure 28 *Simulated vs experimental data from 3.8kA magnet pulse for 8-turn magnet coil. (Top) Magnetic field data. (Bottom) Corresponding current and voltage data.*

After validating the magnet coil and circuit on the bench, magnetized gun shakedown tests were performed, shown in Figure 29. Results showed 7.2kA peak magnet current at a capacitor charge voltage of 60V. This is significantly more current than observed during bench testing. This is because aluminum transmission line from the gun runs through the magnet center, reducing its effective inductance, resulting in a shorter pulse with increased current compared to bench testing. For the shot shown, the gun was fired 3.8ms after the magnet was fired, just below the current peak. This turned out not to be the best timing for firing the gun as eddy current effects significantly delayed the arrival of peak magnetic field into the breech.

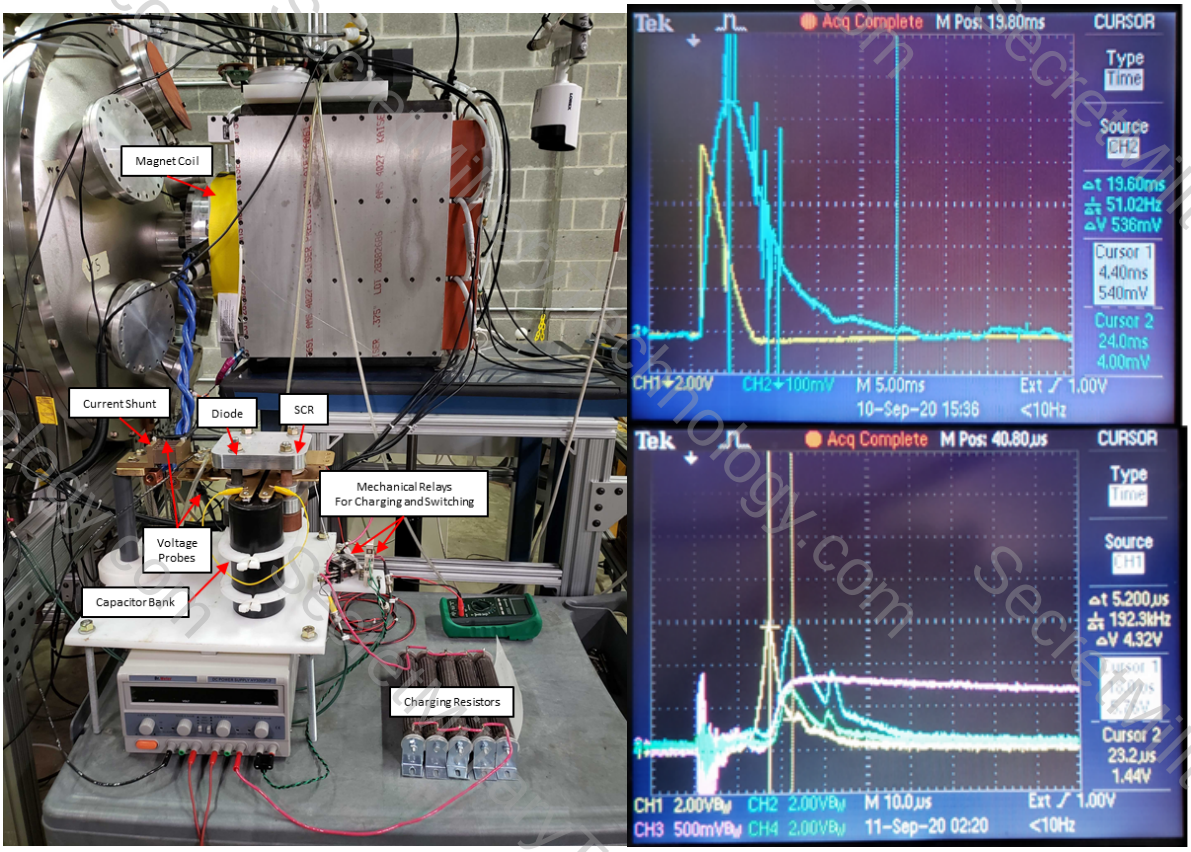

Figure 29 *(Left) Magnetized gun shakedown test setup. (Top-right) Experimental magnet current and voltage signals. (Bottom-right) Plasma jet photodiode signals*

An internal B-dot array and 100-turn pickup coil were both used to measure, map and verify the field in the breech. The internal B-dot array is shown in Figure 30. It consists of 16 individual 25-turn coils used to map the magnetic field down the axis of the gun. Figure 31 shows measurements from the internal B-dot array and modeling results of the magnetic field at and around the gas ports in the breech of the gun. Figure 32 shows data from the 100-turn pickup coil, along with the coil itself, which was used as a simple secondary diagnostic placed in the breech of the gun at the gas valve ports. The internal B-dot array was a complicated diagnostic, so the 100-turn pickup coil allowed for a simple sanity check to confirm that the data from the internal B-dot array was good and being interpreted correctly. The data overall shows good agreement with modeling and indicates that the gun would be better fired with a 14.2ms delay relative to the magnet firing, rather than the originally tested 3.8ms, as a result of magnetic diffusion.

Figure 30 *Internal B-dot array with a total of 16 individual 25-turn coils. (Top-left) CAD model showing location of each individual B-dot coil. (Top-right) Assembled B-dot array assembly. (Bottom-left) B-dot array assembly mounted on gun inner electrode. (Bottom-right) B-dot array assembly fully installed.*

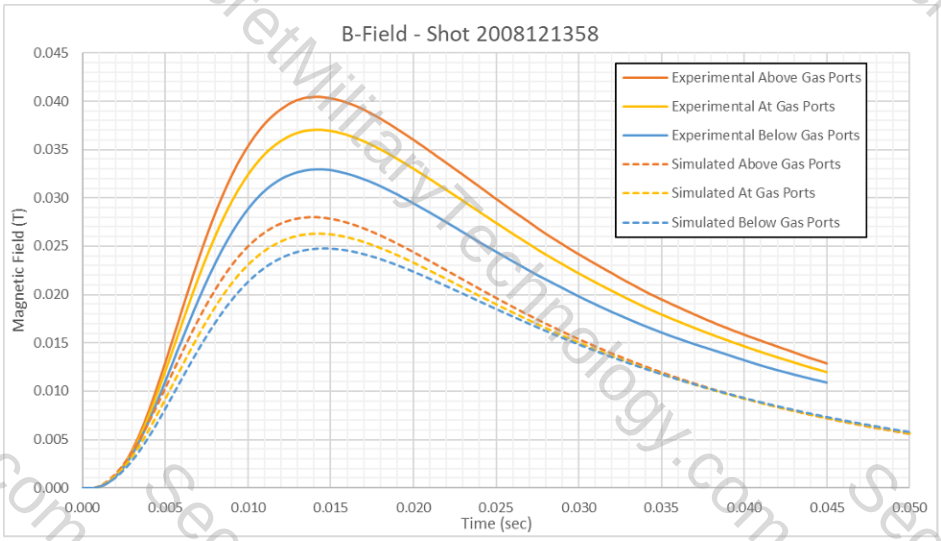

Figure 31 *Internal B-dot array experimental and simulated data from a magnet charge voltage of 60V for the 8-turn magnet coil.*

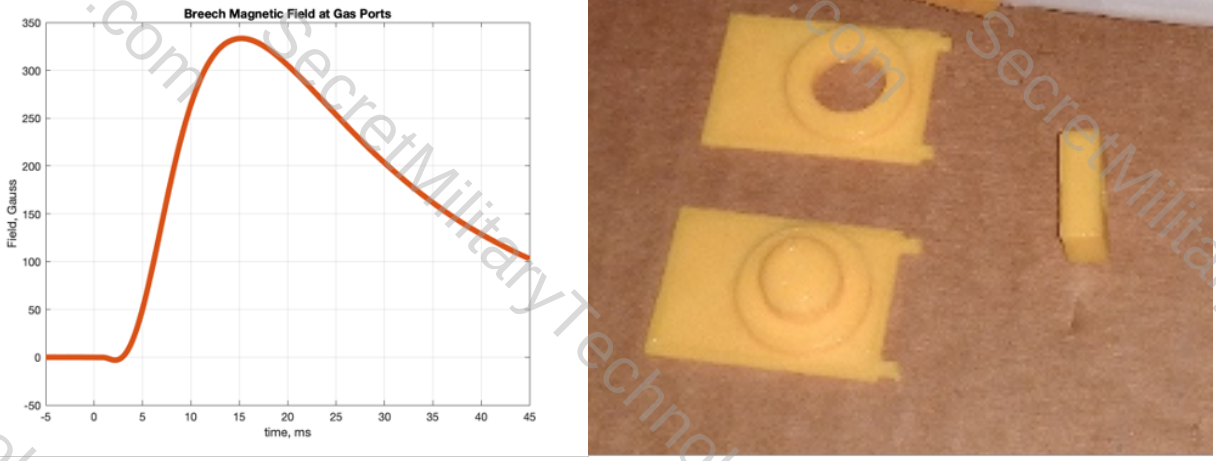

Figure 32 *(Left) 100-turn pickup coil data for a magnet charge voltage of 60V. (Right) 100-turn pickup coil mounted on plastic rod, along with 3D printed components used as a winding jig.*

4.2 Revised Magnet Circuit with 30-Turn Magnet Coil

The experimental results for the magnetized plasma jet using the initial magnet circuit and 8-turn coil were good, but more field in the breech was desired than the 300G to 400G that this initial configuration could provide. A revised magnet circuit was developed with significantly higher energy, along with a more inductive 30-turn magnet coil. The higher inductance was desired to extend the pulse, reducing magnetic forces and stresses as the result of a lower dB/dt for a given prescribed field value.

The revised magnet circuit model is shown in Figure 33, along with current and voltage plots from 350V of charge on the capacitors. The revised circuit used 17 electrolytic capacitors in parallel, SCR switching, a crowbar diode and positive charging to energize a 30-turn magnet coil. The capacitors were rated for 24mF at 350V, for a total circuit capacitance of 408mF and total circuit energy of 25kJ. This was a 19-fold increase in total circuit energy over the initially magnet circuit. The same SCR and diode as before were used, with the SCR rated for 18.7kA at 1.4kV and the diode rated for 23kA at 1.8kV. Effective coil inductance and resistance values were measured on the gun, which includes mutual inductance from the gun's transmission line. The simulated pulse shapes were fine-tuned against experimentally measured pulse shapes, requiring an additional $8.4m\Omega$ to be placed in series with the SCR switch for the model to match the experiment. The result is a current peak of 10.6kA at 8.5ms vs 7.4kA at 4ms with the initial circuit. Due to the increased turn count of the magnet, this represents a significant increase in the maximum amp-turns in the coil vs the initial circuit, 318 Amp-turns vs 35.2 Amp-turns, respectively, and thus should provide much a higher magnetic field. A partially manufactured version of this revised circuit is shown in Figure 34.

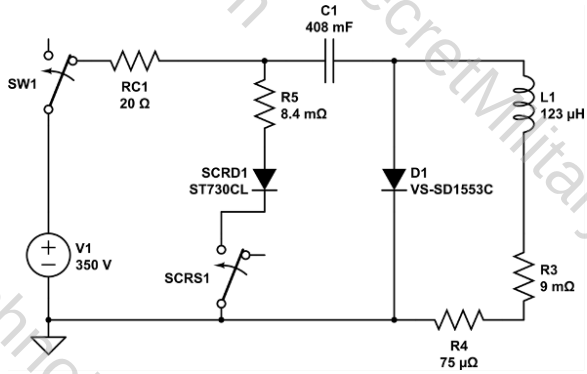

(a) Revised circuit model for 30-turn magnet coil, along with current and voltage from 300V capacitor charge.

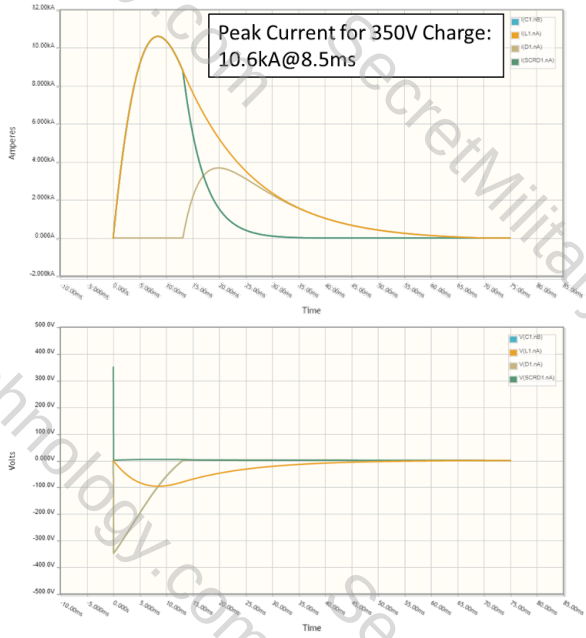

(b) Simulated current and voltage signals from initially deployed circuit model at 300V charge.

Figure 33 *Revised circuit model for 30-turn magnet coil, along with current and voltage from 300V capacitor charge.*

Figure 34 *Revised magnet circuit during construction for driving 30-turn magnet coil*

The SPICE circuit model results shown above were subsequently fed into EMS for comparison against the measured magnetic field in the breech. EMS results of the magnetic field at and around the gas ports in the breech of the gun are shown in Figure 35 and show an order of magnitude improvement in achievable breech field compared to the initial circuit and magnet combination, 3.1kG with the revised circuit and magnet vs ~300G with the initial circuit and magnet. The magnetic field now peaks at 28ms in the breech due to eddy current effects, shown in Figure 36. These eddy currents also result in large magnetic forces against the plasma gun's aluminum transmission line plates, as shown in Figure 37. At 350V magnet charge voltage, 86kN of peak force is momentarily present against the plasma gun's transmission line plates. This is reaching, but still within, the mechanical limits of the transmission line assembly. The magnet coil itself momentarily experiences 78kN of peak axial force, which includes forces from the rest of the gun as well, not just the transmission line plates.

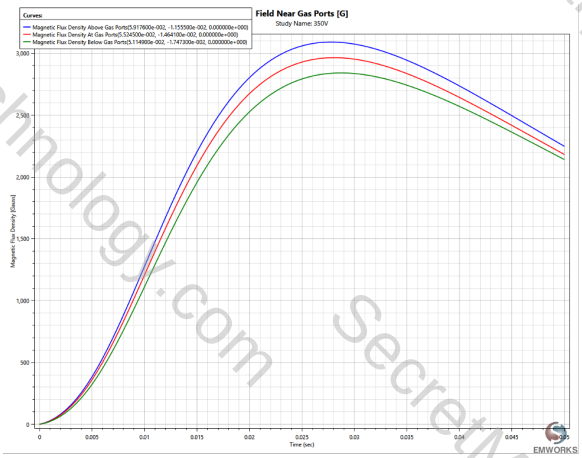

Figure 35 *EMS results for magnetic field at and around gas ports in the breech of the gun from a capacitor charge voltage of 350V for the 30-turn magnet coil.*

The eddy current effects also result in relatively poor coupling of field into the breech, as the eddy currents generated in the gun's aluminum transmission line that runs through the magnet center are large. Despite the poor coupling, modeling indicates that there is still

4mWb of flux linking gun electrodes in the breech, which is ultimately the desired amount of flux linkage. If more breech field is desired in the future, replacing aluminum with stainless steel in select portions of the transmission line to mitigate the effect of these eddy currents would allow a good deal more field to make it into the breech for a given applied external field, as shown in Figure 38 and Figure 39. This would allow for 6.8kG of peak field at 13ms in the breech with stainless steel versus 3.1kG at 28ms with aluminum at a magnet charge voltage of 350V, essentially allowing for more breech field without increasing magnet power. This translates to 9.2mWb of flux linking gun electrodes in the breech with stainless steel transmission line components versus the 4.0mWb achieved with aluminum components at the maximum magnet charge voltage of 350V. Magnetic forces are also significantly reduced for a given breech magnetic field, as shown in Figure 40 and Figure 41. With stainless steel, peak force against the gun's transmission line plates is reduced to 15kN versus the 86kN seen with aluminum at a magnet charge voltage of 350V. This translates to significantly reduced axial force seen by the magnet coil as well, down to 27kN peak with stainless steel versus the 78kN peak seen with aluminum.

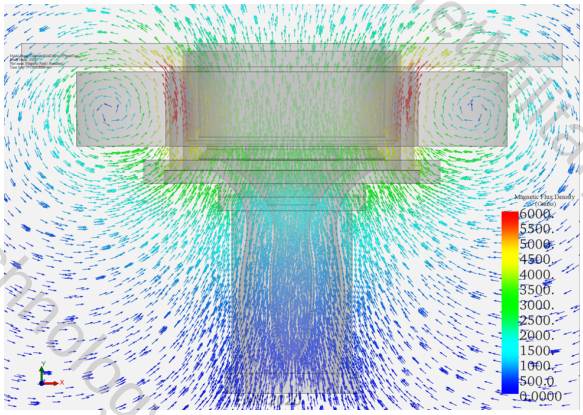

Figure 36 *EMS vector plot of peak magnet field at Δt = 28ms, when the breech field reaches its peak for the 30-turn magnet coil.*

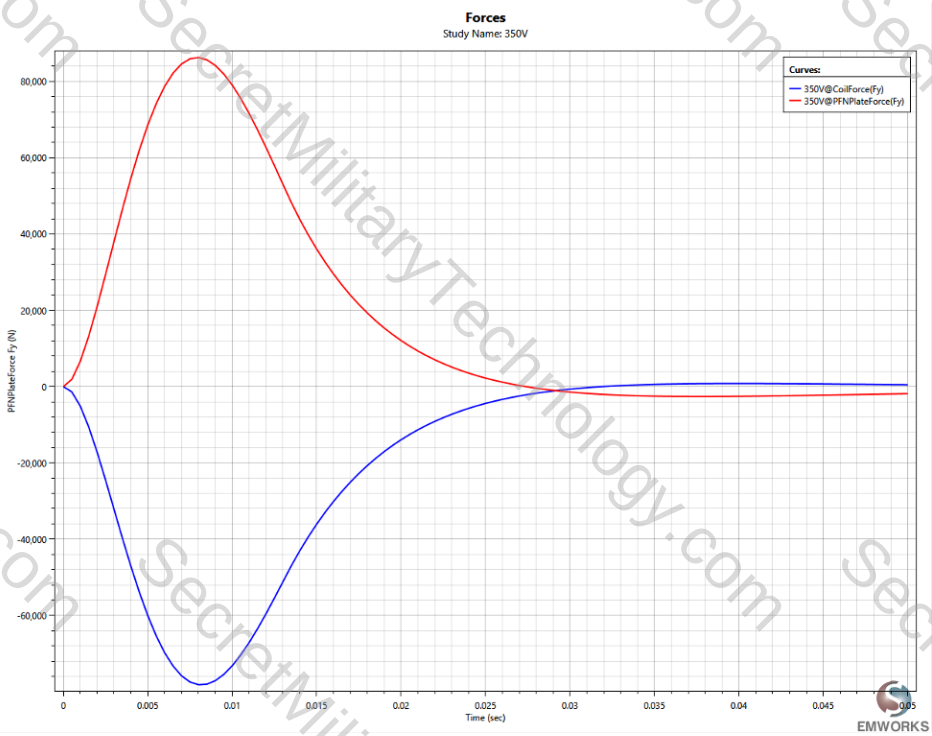

Figure 37 *Repulsive force between the magnet coil and the aluminum transmission line plates on the plasma gun from a capacitor charge voltage of 350V for the 30-turn magnet coil, which experience the largest forces from the magnet pulse.*

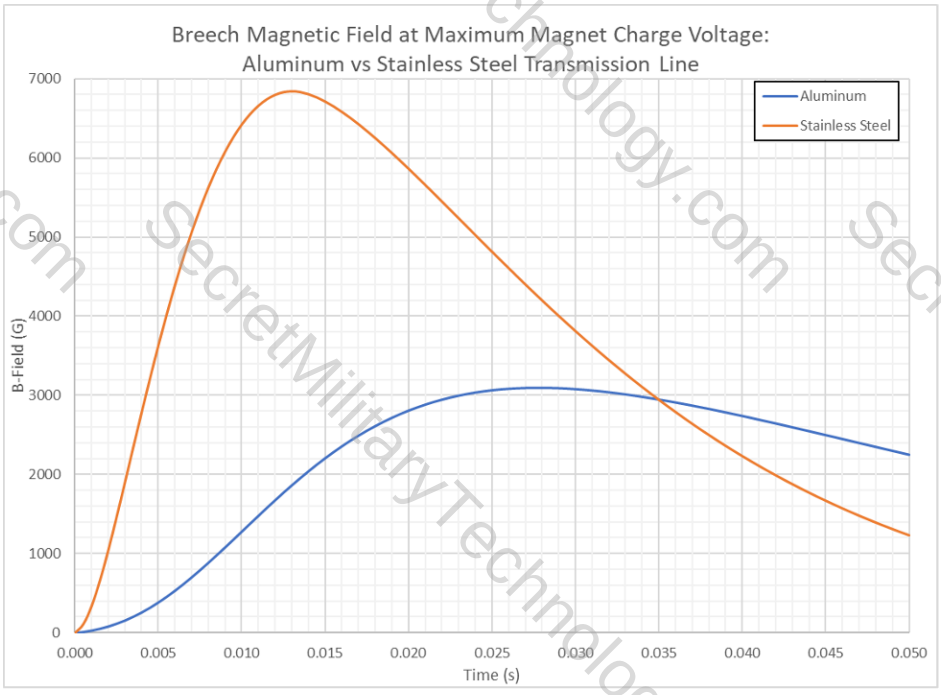

Figure 38 *Breech magnetic field with aluminum vs stainless steel plasma gun transmission line tubes and gun-side transmission line plates from a capacitor charge voltage of 350V for the 30-turn magnet coil.*

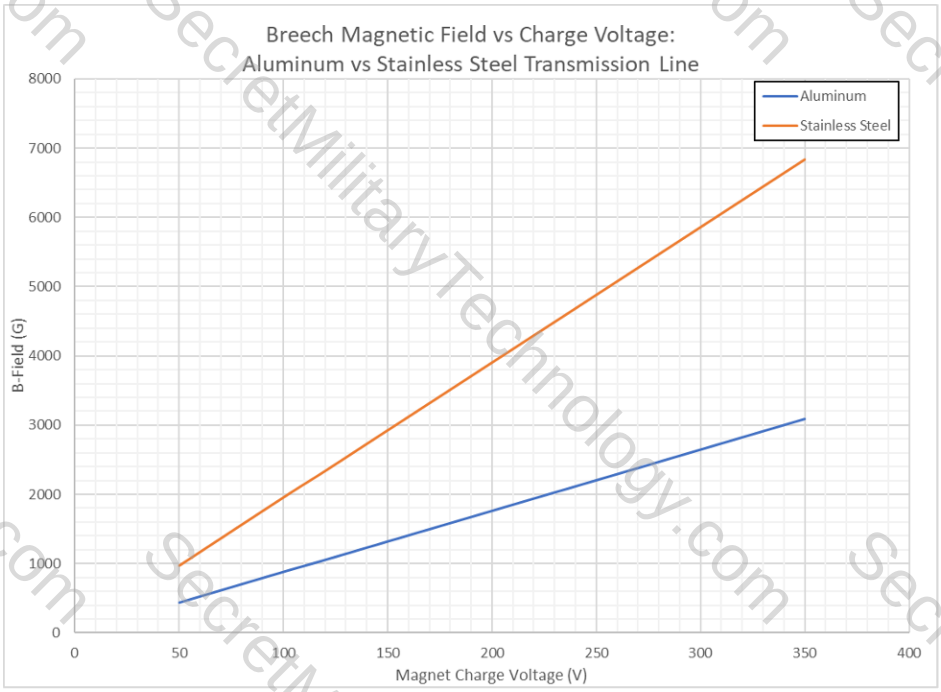

Figure 39 *Breech magnetic field with aluminum vs stainless steel plasma gun transmission line tubes and gun-side transmission line plates versus magnet charge voltage for the 30-turn magnet coil.*

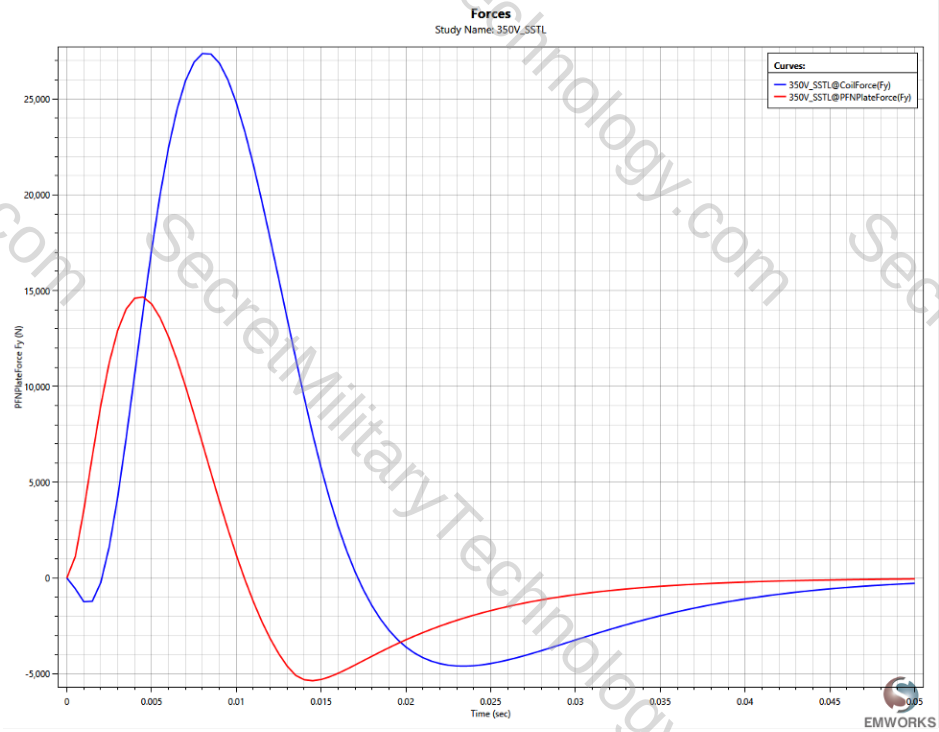

Figure 40 *Force between the magnet coil and stainless steel transmission line plates on the plasma gun from a capacitor charge voltage of 350V for the 30-turn magnet coil.*

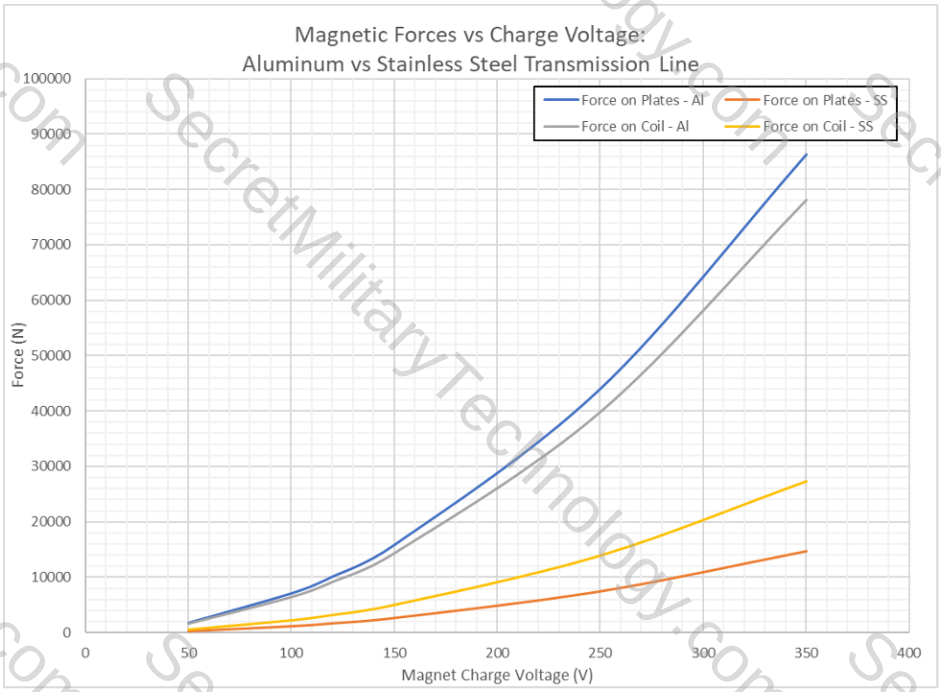

Figure 41 *Force between the magnet coil and either aluminum or stainless-steel transmission line plates on the plasma gun versus magnet charge voltage for the 30-turn magnet coil.*

The 30-turn coil required considerably more care in its manufacturing than the initial coils due to its potential for so much higher fields. The 30-turn magnet coil was wound from 2/0 THHN cable, using a modified version of the lathe mounted winding jig shown above. The winding process for the 30-turn coil is show in Figure 42. The wound coil was wrapped with fiberglass strapping tape between layers and two layers of 1/16" fiberglass weave around the OD. The fiberglass wrapped coil was then encapsulated using 20-3001 NC epoxy, which has a 5,700psi tensile strength, and vacuum degassed, as shown in Figure 43. Once encapsulated, the 30-turn coil was mounted on a gun for testing with the revised magnet circuit, as shown in Figure 44. The revised circuit was validated prior to testing using the same commercially manufactured coils used to validate the initial circuit.

Figure 42 *The 30-turn coil is wound manually at HyperJet with the help of a large lathe.*

Figure 43 *Fiberglass wrapped 30-turn coil epoxy encapsulation and vacuum degassing.*

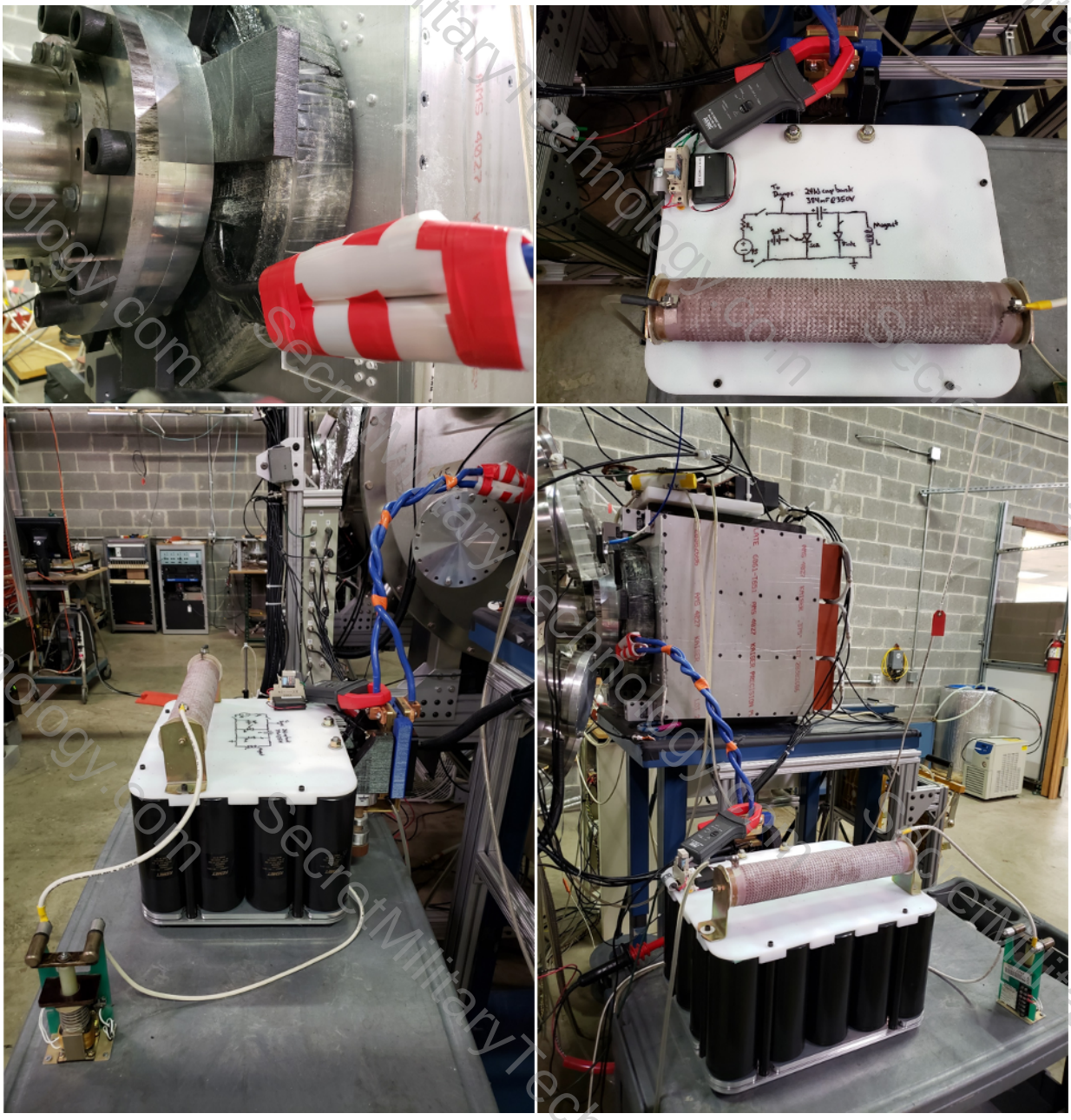

Figure 44 *Experimental setup for 30-turn coil testing, mounted on gun with revised magnet circuit.*

The 100-turn pickup coil discussed above was used to measure the resultant magnetic field in the breech from the 30-turn magnet coil. The experimental breech magnetic field and magnet current pulses are shown in Figure 45 and Figure 46 and compared against EMS and SPICE modeling results for two different capacitor charge voltages. These data show excellent agreement with the EMS and SPICE simulations and confirm that the gun would be best fired with a 28ms delay relative to the magnet firing with the 30-turn magnet coil.

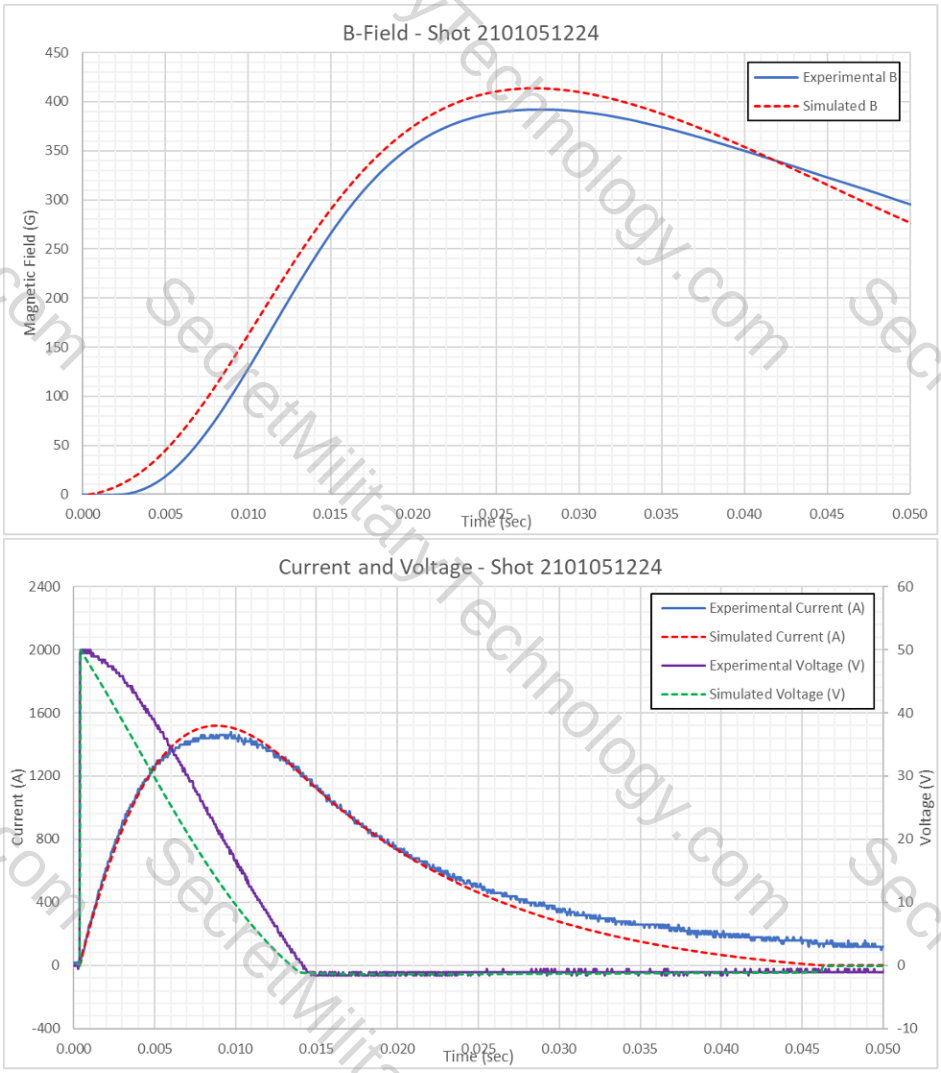

Figure 45 *Simulated vs experimental data. (Top) Breech B-field. (Bottom) Corresponding current and voltage pulses from 50V capacitor charge for 30-turn magnet coil.*

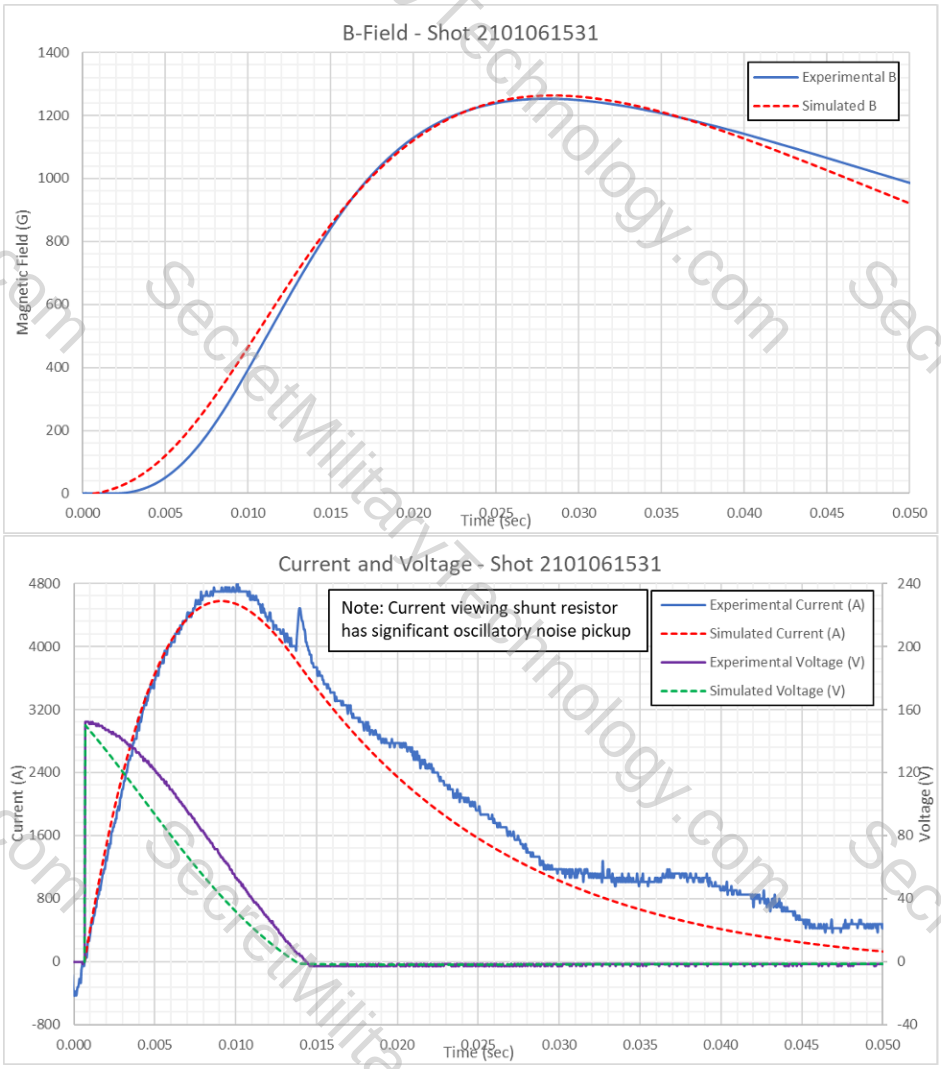

Figure 46 *Simulated vs experimental data. (Top) Breech B-field. (Bottom) Corresponding current and voltage pulses from 150V capacitor charge for 30-turn magnet coil.*

5 Diagnostics (Task 3)

5.1 Electrical Diagnostics

The key electrical parameters of the gun during operation are measured using either Rogowskis integrated using 100 microsecond time constant RC integrators, or Pearson current transformers. The voltages are measured by putting 2 $k\Omega$ high current resistors in parallel with the load, and measuring the current using 1V/A Pearson current transformers. The Gas Valve current is measured using a 0.01 V/A Pearson, and the current from each of the six PFN switches is individually measured using Rogowskis custom wound using a winding jig. Typical PFN current traces are shown in Figure 47.

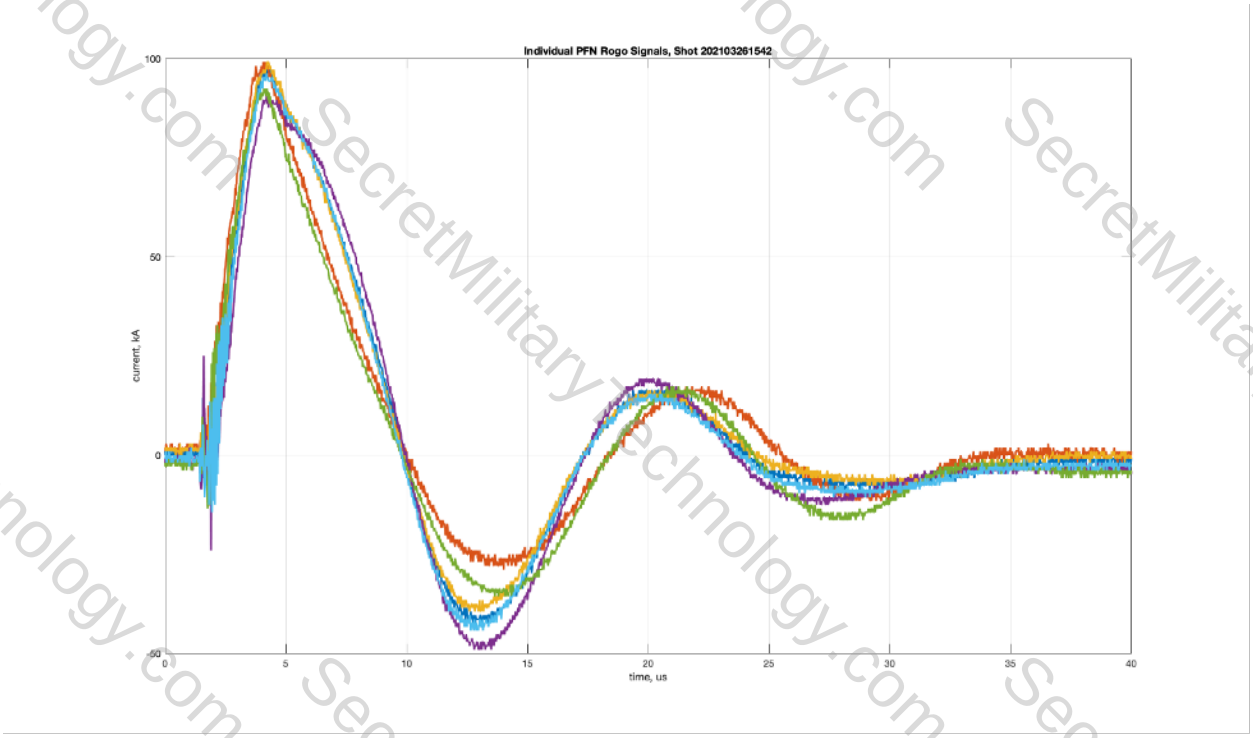

Figure 47 *Typical plasma gun PFN current traces from Rogowski coils for magnetized jets of He.*

5.2 Photodiodes

The photodiode velocimetry system has been upgraded for improved spatial resolution. The two photodiodes collect light from viewing volumes separated by 150 mm. The light is collected by two focusing collimators which convey the light into fibers that bring it to the Thorlabs PDA10A amplified PIN diodes located in the screen room for noise immunity. Velocity is inferred from the difference in arrival times at the two viewing volumes. This velocity is then used in the calculation of mass and width based on the interferometer signal. Typical traces are shown in Figure 48.

There is some ambiguity regarding the exact time of arrival at the viewing location since the shapes of the two photodiode signals differ. Accordingly, we are using 4 different methods of finding the time difference between the plasmoid arrival times at the photodiode viewing volume. These are (1) time to rise to 50% of peak value, (2) peak of the signal, (3) centroid of the top 10% of the signal, and (4) centroid of the top 25% of the signal. The first method gives the fastest velocities (shortest time difference) with the least deviation from shot-to-shot, whereas the remaining three tend to give slightly lower velocities with more spread in values from shot-to-shot.

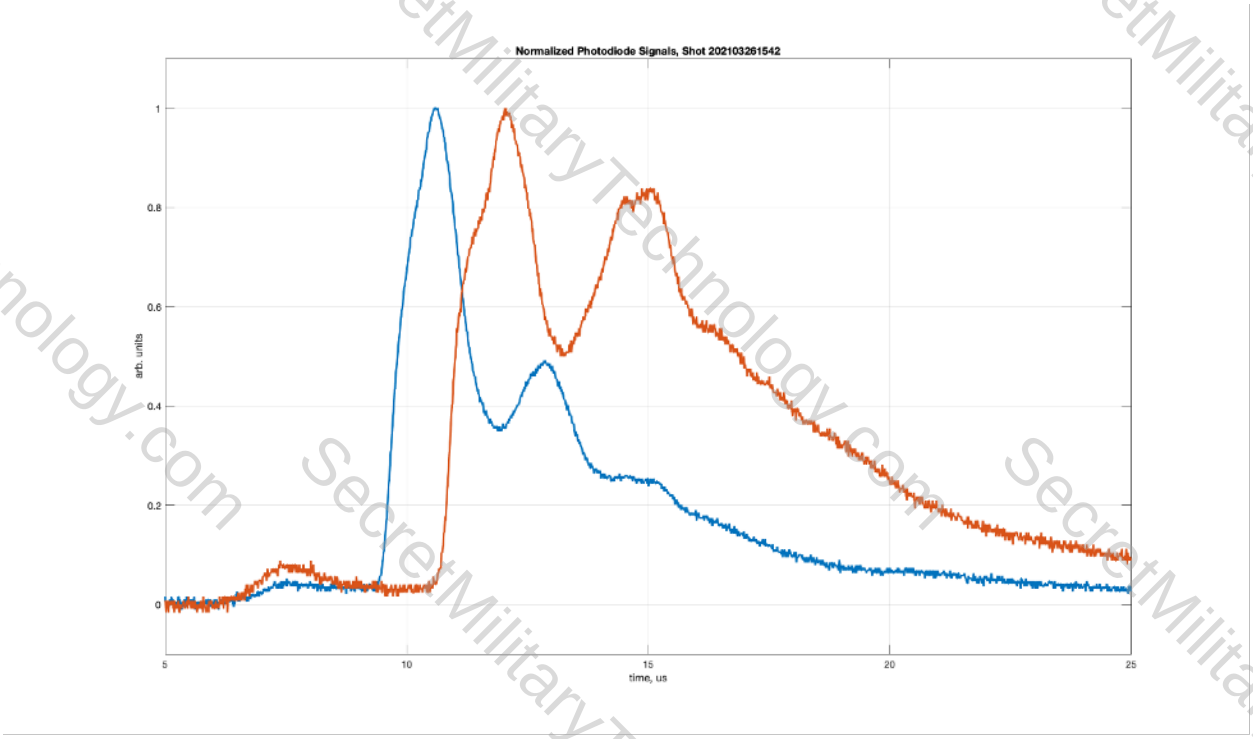

Figure 48 *Typical plasma gun photodiode signals for magnetized jets of He.*

5.3 Interferometer

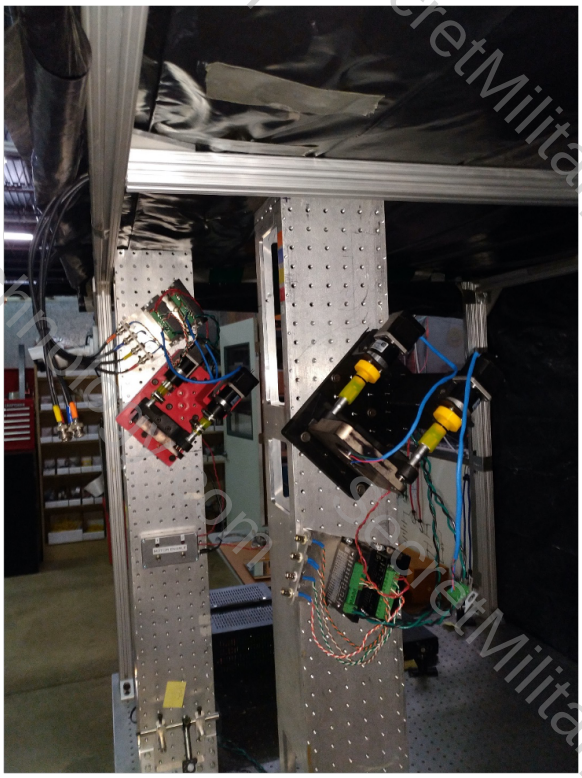

Figure 49 *Motorized mirror mounts developed for the HyperJet interferometer system.*

The interferometer is upgraded from the previous version, adding the capacity for a second channel at the center of the chamber if needed. The key elements for the second channel are in place, awaiting only a few additional mirrors (cost $500 total) to be brought into regular operation. The interferometer itself is a quadrature heterodyne system using a 635 nm HeNe laser, which has been designed for two channel operation, though only one channel is complete, as mentioned above. The beam is modulated at 40 MHz by an Acousto-Optic modulator which also serves as the splitter for the reference and sample beams. The sample beam is passed through the chamber off a retroreflector on a custom vibration isolation stand and returned to a polarizing beam splitter for recombination with the reference beam. The reference beam travels a path of the same length (within about 5 mm). A quarter wave plate is inserted into the sample beam so the first pass transforms the linearly polarized light (laser is polarized) into circularly polarized light, and on the return pass it transforms it into linearly polarized light at 90 degrees to the original polarization. This allows the recombination beam splitter to be placed so the horizontally polarized outgoing sample beam passes through undeflected, but the vertically polarized return beam is reflected by the splitter onto a path collinear with the reference beam. The reference beam is horizontally polarized, so to get an interference pattern we pass the combined beam through a polarizer at 45 degrees, picking off the relevant component of each contributing beam so they interfere and produce good modulation of the interference pattern. Rotating the polarizer slightly either side of 45 degrees changes the relative contribution of each beam, which is helpful since sometimes there is much less power in the sample beam than the reference beam, so tuning by rotating the polarizer allows us to make the two contributions to the interference pattern similar in magnitude so as to maximize depth of modulation. The interference signal is detected by a ThorLabs PDA10A PIN diode with >100 MHz bandwidth. The photodiode signal is sent to the demodulation circuit, where it is mixed with the reference output from the Acousto-Optic modulator driver, producing two output signals, one proportional to the cosine of the phase shift and one proportional to the sine. The phase is extracted by taking the arctangent of the ratio of these signals, and then it is a simple proportionality constant multiplier to obtain line integrated density. There is ambiguity in the arctan when the phase change exceeds 2π, which must be handled carefully to avoid spurious jumps in the signal.

The existing interferometer channel is 355 mm from the muzzle of the gun, halfway

between the photodiode viewing volumes. The noise on the interferometer signal due to the firing of the PFN switches has been dramatically reduced by moving the detector (a reverse biased PIN photodiode) into the screen room. In addition, a motor-controlled mirror has been added which allows the interferometer to be tuned from within the screen room. This is because over the course of a day of shooting the interferometer, signal quality tends to degrade as small shifts in the position of the optical table or retroreflector stand due to thermal effects or vibration from firing the gun accumulate, requiring tuning up every hour or so. The remote tuning allows this to be done without entering the HV bay, which requires de-arming the HV systems, saving time and reducing opportunities for errors. The motorized mirror mounts (2 channels) can be seen in Figure 49, the screen room control system in Figure 50, and a sample interferometer trace is shown in Figure 51.

Figure 50 *Screen room control system developed for motorized mirror mounts.*

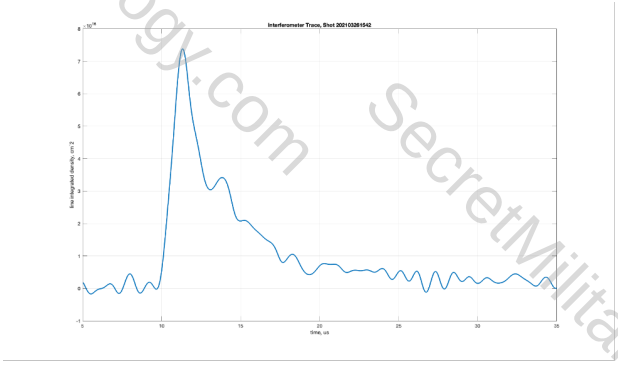

Figure 51 *Representative interferometer trace for magnetized jet of He.*

5.4 Spectroscopy

The spectrometer sent to HyperJet from LANL is operational with 4 fibers viewing the plasma, 2 parallel to the direction of motion, and 2 perpendicular. The parallel views are in fact 15 degrees off axis since the diagnostic fork is in the way, but primarily so that they are not looking directly into the muzzle of the gun, which would contaminate the signal with light from the ringing of the bank exciting residual gas in the gun. The spectrometer is shown in Figure 52.

The instrument is a 0.25 m Czerny-Turner configuration, with 3 gratings installed, 100 lines/mm, 150 lines/mm, and 300 lines/mm. This gives us 0.46 nm/pixel for the 100 lines/mm, and 0.155 nm/pixel for the 300 lines/mm grating. Currently we are using the 100 lines/mm grating to get survey information,

Figure 52 *LANL spectrometer*

but once we have found a good operating regime in hydrogen we will switch to the higher resolution gratings to improve sensitivity. We will look first for the H-alpha line, and if there is enough light we will look at H-beta, which should give us insight into the magnetic field strength due to Zeeman splitting.

The image from a shot using Helium is shown in Figure 53(a), with the corresponding lineout shown in Figure 53(b). The top two sets of lines are from the two parallel views. The third set of lines is from the perpendicular view, with the fourth set just off the bottom of the CCD, so not shown here.

(a) Spectrum from magnetized He plasma.

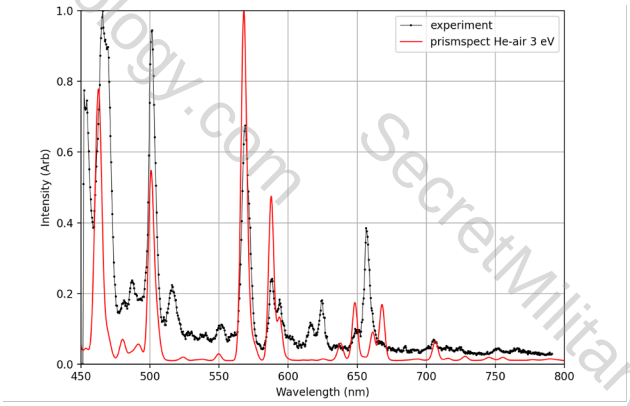

(b) Corresponding lineout from spectrum shown above along with mixed He/air PrismSpect fit.

Figure 53 *Spectrum of He plasma*

5.5 B-dot probes

The modular diagnostic fork system consists of three main assemblies: the head assembly, the rod seal assembly, and the back-end cable breakout assembly, as shown in Figure 54. A great deal of effort has been put into getting the best possible data out of the B-dot probes themselves. They are 3-axis probes, with 10 turn coils for each of the x, y, and z axes. The coils are wound on a custom 3D printed form shaped so that the centers of the coils are at the same position and the total cross-sectional area of each coil is the same. The coils are shielded from the plasma by a 10mm OD, 8mm ID closed-ended quartz tube mounted on an aluminum fitting which contains a plug for getting the signals out. The individual wires for each B-dot coil are twisted together, then each twisted pair is spread apart from one another and shielded with copper tape grounded through a pin in the connector to reduce the noise from outside electrical interference. All this fits inside the quartz tube cemented into the aluminum vacuum adapter subassembly. The orientation of the B-dots to the connectors were critical in maintaining a constant plane orientation of the B-dot coils. This fitting mates to a fork structure giving multiple probes for spatial resolution and the ability to replace B-dot probes with other probes such as a triple probe for electron temperature measurement (discussed in the next section). A picture of a 3-axis B-dot probe assembly is shown in Figure 55.

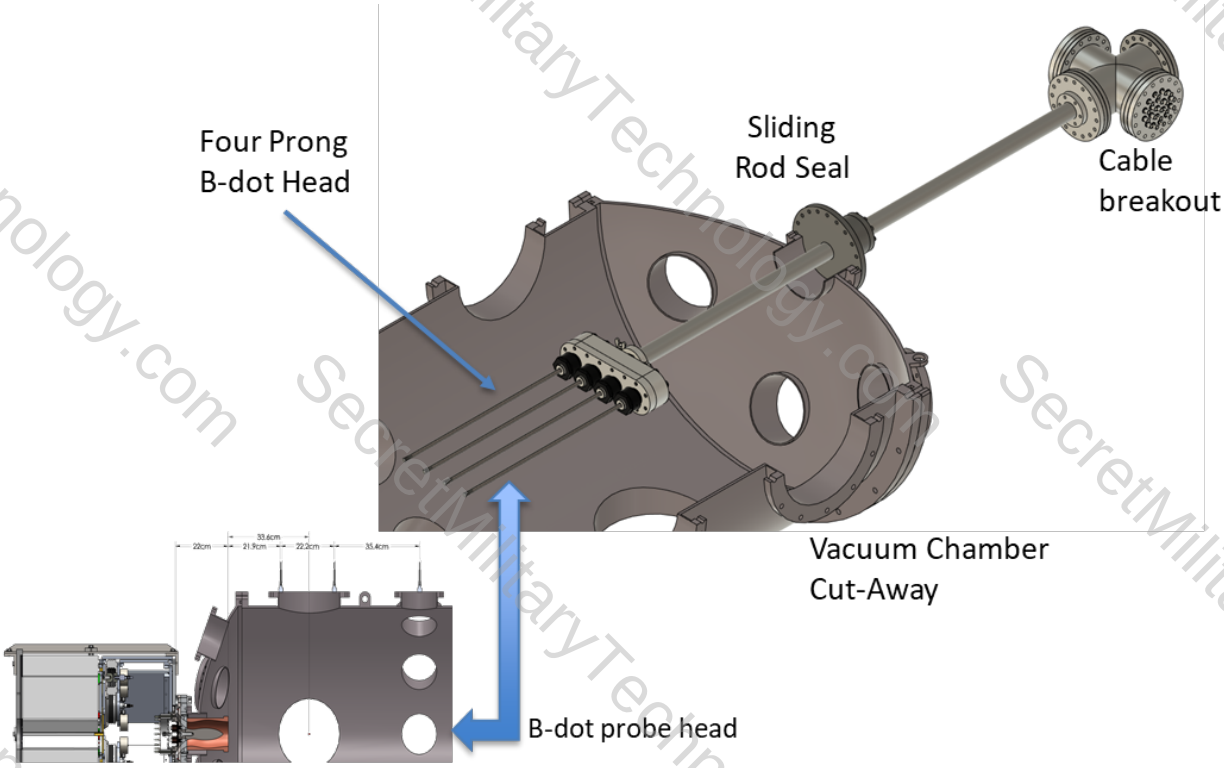

Figure 54 *HyperJet modular diagnostic fork system overview.*

Figure 55 *3-axis B-dot probe assembly*

The diagnostic fork system features a modular head for future diagnostic purposes, as shown in Figure 56. A cross-sectional view of the head assembly is shown in Figure 57. The modular head assembly design also allows the option to perform maintenance through the windows of the vacuum chamber. The individual probes are interchangeable/removable, in addition to the entire head. The modularity of the system should prove useful for making quicker changes to future designs.

Figure 56 *Modular diagnostic head assembly with B-dot probes*

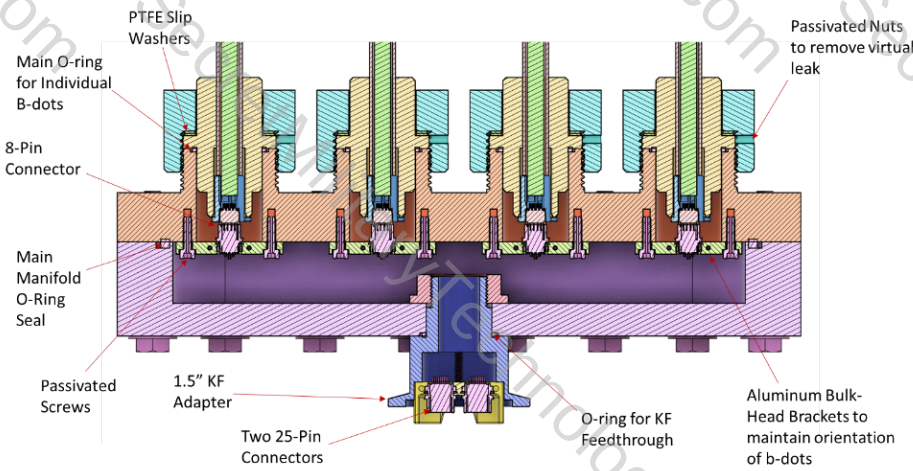

Figure 57 *Cross-sectional view of modular diagnostic head assembly.*

The rod seal assembly allows linear movement of the diagnostic stalk while under high vacuum, shown in Figure 58. A cross-section of the rod seal assembly is shown in Figure 59. The modular diagnostic fork system allows for differential pumping through the rod seal assembly while maintaining electrical connectivity with the B-dot coils. Differential pumping reduces relative pressure against vacuum seals into the chamber, allowing the main chamber to achieve high vacuum more easily. Component materials were generally chosen to reduce outgassing, although this could not be done for all the wires and connectors required by the electrical system, necessitating the use of differential vacuum pumping, rather than pumping the entire system to high vacuum.

Figure 58 *Diagnostic rod seal assembly*

The back-end cable breakout assembly is where all the diagnostic wires within the system transition to BNC connectors for monitoring and recording, shown in Figure 60. The cable breakout assembly is a vacuum cross featuring custom flanges with 38 BNC feedthroughs, of which the center conductors are wired to two 25-pin d-sub connectors, as shown in Figure 61. Using only the center conductors diminishes the likelihood of crosstalk between channels. The d-sub connectors then connect to a custom-made wire bundle consisting of coaxial cables, further reducing electromagnetic interference and keeping inductance low. The other ends of the coaxial cables are then attached to a 3d-printed connector which adapts to the two 25-pin connectors in the head assembly.

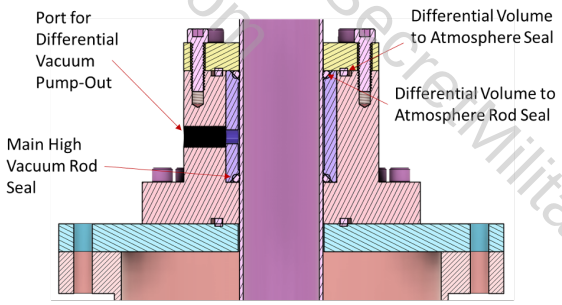

Figure 59 *Cross-sectional view of diagnostic fork system rod seal assembly.*

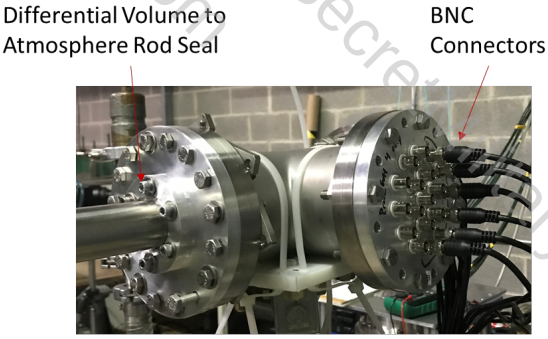

Figure 60 *Back-end cable breakout assembly of diagnostic fork system.*

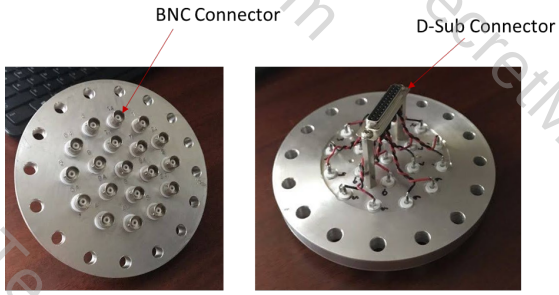

Figure 61 *Custom made BNC feedthrough flange with d-sub connector for back-end cable breakout assembly.*

The originally deployed diagnostic fork system is shown in Figure 62. The originally deployed fork structure has 4 locations for probes, as shown in Figure 63. The figure also shows the arrangement of the probes in the chamber, and the movable fork on the sliding rod seal assembly for scanning along the z-axis of the vacuum chamber. The small yellow fixture on the leftmost probe is a 3-axis Helmholtz calibration coils with 10-turns per coil developed for calibration of the probes in-situ. The form is 3D printed and fits precisely over the probe tips so that the center of the calibration coils is coincident with the center of the B-dot pickup coils.

Figure 62 *Originally deployed diagnostic fork system mounted on HyperJet vacuum chamber.*

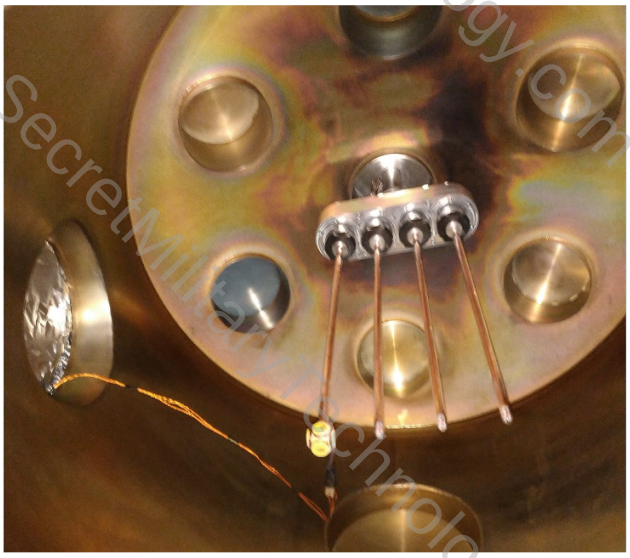

Figure 63 *Originally deployed 4-probe diagnostic head assembly in HyperJet vacuum chamber with 3-axis Helmholtz calibration coils attached.*

The calibration coils were modeled in EMS, as shown in Figure 64, to attain flux through X (inner-most coil), Y (middle coil) and Z (outer-most coil) b-dot coils per amp applied to the calibration coils. This was used to interpret the signal being seen on the B-dot probes during calibration.

The B-dot coils were modeled as flux surfaces centered between Helmholtz coils. The 10-turn Helmholtz calibration coils were modeled as coils wound with 24awg wire. The X and Y axis calibration coils are separated by 17mm. The Z axis calibration coils are separated by 23mm. Resultant flux through the X, Y and X flux surfaces of the B-dots from the corresponding Helmholtz calibration coils were 1.177×10^{-8} Wb/Amp, 1.375×10^{-8} Wb/Amp and 7.834×10^{-9} Wb/Amp, respectively. EMS plots of the resultant field for each axis are show in Figure 65.

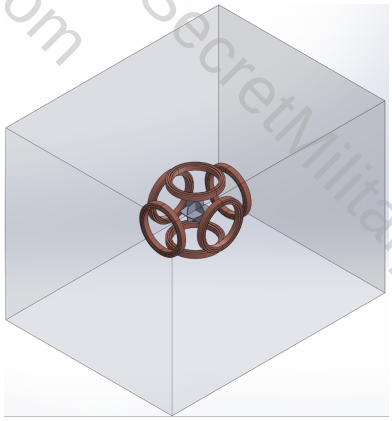

Figure 64 *3-axis Helmholtz calibration coils with 10-turns per coil solid model for EMS.*

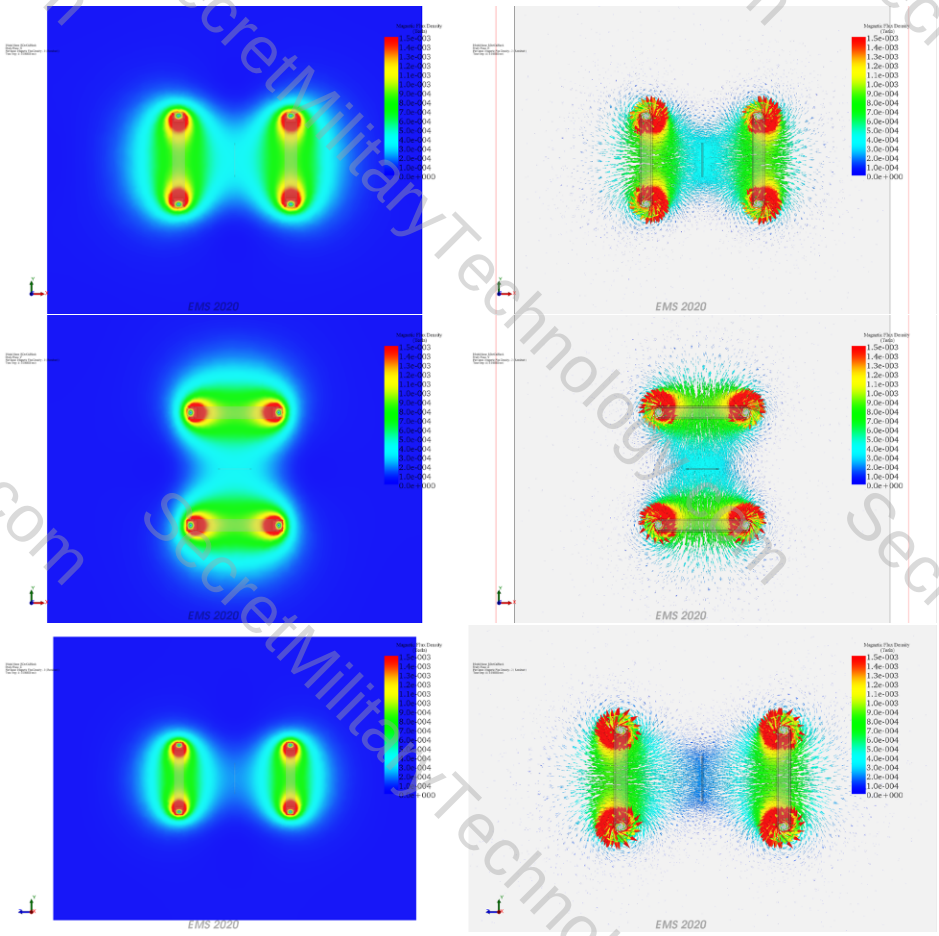

Figure 65 *B-field from 3-axis Helmholtz calibration coils for B-dot probes. (Top) Z-axis B-field. (Middle) Y-axis B-field. (Bottom) Z-axis B-field.*

A new diagnostic head assembly with a 3-probe fork has recently been deployed, along with an improved rod seal assembly and linear motion control. The reason for the change is to provide better high current connections for the triple probe, which can be placed on the center location or swapped out for another 3-axis B-dot probe, as well as allow for easier and more accurate positioning of the probes within the vacuum chamber. The new head is shown in Figure 66, along with two B-dot probes and the triple probe. The revised linear motion feedthrough carriage assembly is shown in Figure 67.

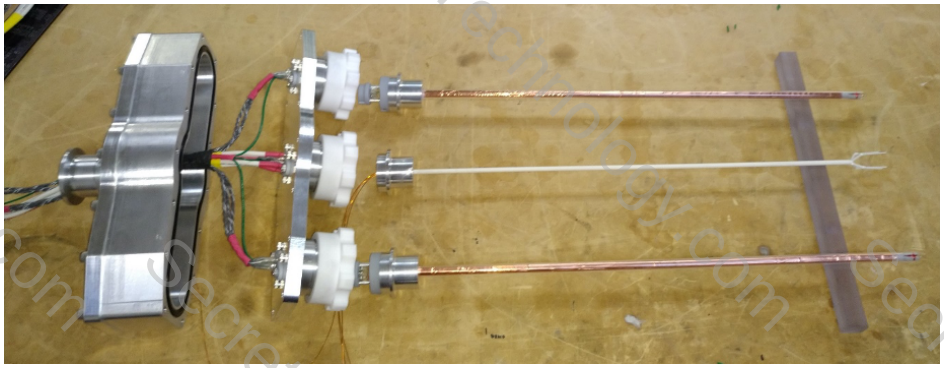

Figure 66 *Revised 3-probe diagnostic head assembly.*

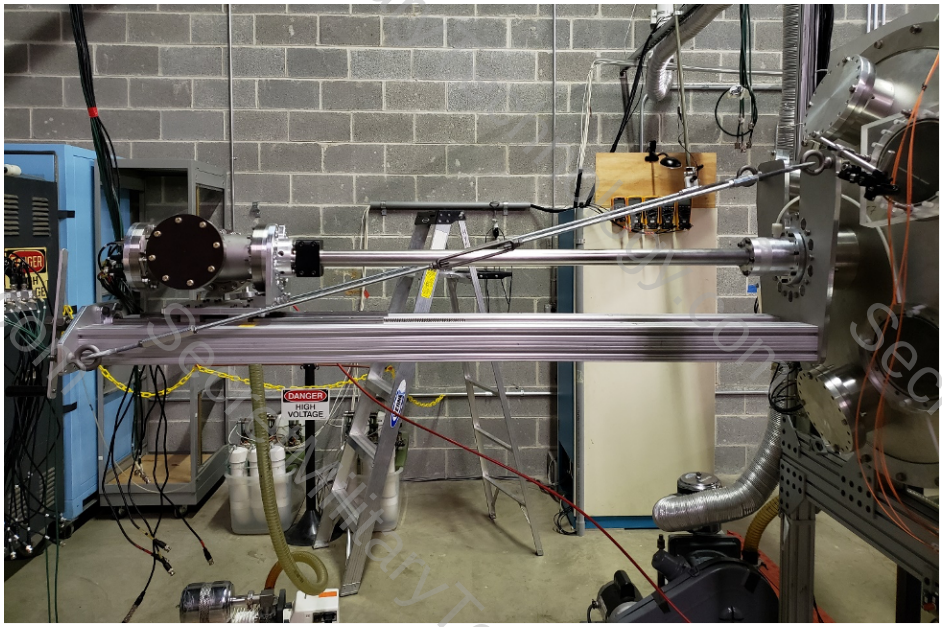

Figure 67 *Revised linear motion feedthrough carriage assembly.*

5.6 Triple Langmuir Probe

Experiments have begun in an effort to refine the triple probe measurements for electron temperature based on prior results from exploratory experiments. A new probe with 4 tips has been constructed, allowing a free probe tip to be able to double up on the floating potential measurement if desired. An image of the 4 tips is shown in Figure 68. One of the modifications going forward will be to make the tips shorter to reduce the current.

Figure 68 *HyperJet's 4-tip triple Langmuir probe.*

The circuit originally used for the exploratory experiments was biased to 18 Volts between the two non-floating tips by using two 9 Volt batteries in series, but this appears to be too high of a bias. Accordingly, we will be using arrays of 1.5 Volt D cell batteries, allowing us to vary the bias by adding and subtracting cells. The high-speed signal from the plasma requires that we use capacitors in parallel with the batteries so as not to load down the tips with the battery impedance. Current is measured using a 1 V/A Pearson current transformer.

The potential of the floating tip will be measured using a Tektronix P5200A differential probe with a 50 MHz bandwidth and the ability to measure millivolt signals on top of up to 1.3 kV bias. The need for a differential probe is largely due to the possible coupling of the plasma potential to the PFN current, which is still ringing by the time the plasma jet reaches the probe. It is not yet clear if the plasma is electrically connected to the PFN by the time it reaches the midpoint of the chamber where we take the triple probe measurements, but the possibility cannot be discounted.

Figure 69 *Tektronix TBS2000B differential probe and shielded box.*

The differential probe requires a dedicated oscilloscope placed in the HV bay since the probe cable is too short to reach the screen room. We have purchased a TBS2000B Tektronix oscilloscope for this purpose and placed it in a shielded box in the HV bay, with electrical isolation from the power lines to reduce noise. The box and differential probe assembly are shown in Figure 69.

5.7 Imaging

We have used a Nikon SLR camera to obtain time integrated (open shutter) images as shown in Figure 70, somewhat tilted due to mounting constrains on the camera. The camera shutter is open for the entirety of the shot, and the plasma is viewed through 3 layers of 90% neutral density filters to cut down light. As a result, the image contains light captured almost solely from the plasma.

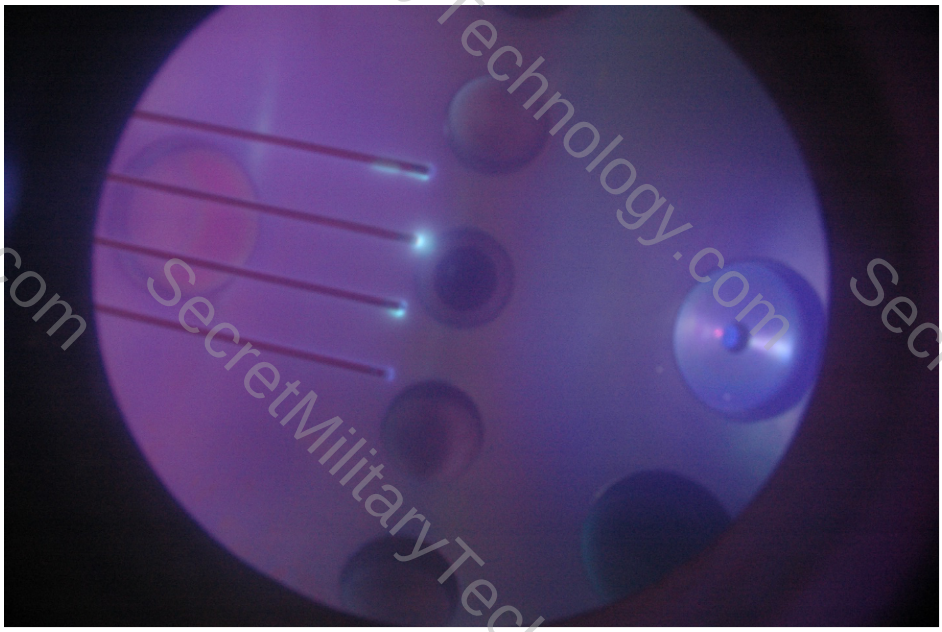

Figure 70 *Nikon open shutter image of magnetized He plasma jet striking B-dot probes.*

6 Experimental campaigns (Task 4)

Several experimental campaigns to explore and fine tune the operational envelope of the magnetized plasma jets were performed with extensive efforts to diagnose and understand the jets formed. During this effort, we investigated various biasing coil configurations, the details of which are discussed above in Task 2. The basic experimental setup for all magnetized jet experiments is shown in Figure 71. The magnetized plasma gun with 30-turn magnet coil is on the left, along with the 2 main photodiodes on the top middle-left, the interferometer beam on the chamber axis between the photodiode projections and the diagnostic stalk with B-dot probes on the right, with the B-dot probe tips at the center of the chamber.

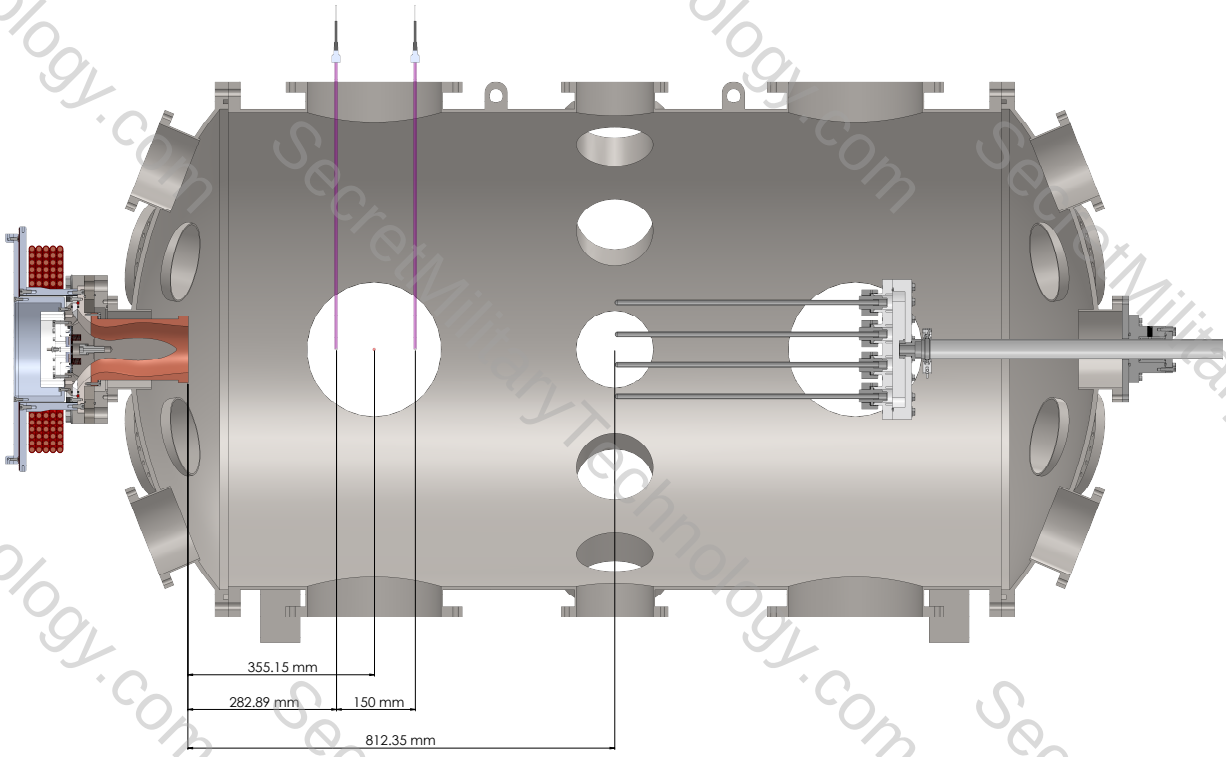

Figure 71 *Experimental setup for HyperJet magnetized plasma jet experiments. Magnetized plasma gun with 30-turn magnet coil is on the left, along with the 2 main photodiodes on the top middle-left, the interferometer beam on the chamber axis between the photodiode projections and the diagnostic stalk with B-dot probes on the right, with the B-dot probe tips at the center of the chamber.*

6.1 Initial Magnet Circuit and 8-Turn Magnet Coil

The experimental campaign with magnetized plasma jets began with the initial magnet circuit and 8-turn magnet coil described above in Task 2. The plasma gun was left exactly how it is configured for the liner guns as well, meaning $600\mu F$ main PFN capacitor bank and unmodified gas valve, the only difference being that the gas valve plenum was filled with Helium for these experiments as opposed to Argon. These experiments moved quickly at

first, focusing mostly on the degree of magnetization of the plasma. The first results from Helium plasmas are shown in Figure 72. Photodiodes show a velocity of 40 km/s for 27 psig gas valve plenum pressure. Lower pressures are faster, but noise from switches interferes with analysis. Interferometry is clear and very promising, similar in shape to what is seen with Argon plasmas. Exact densities require Gladstone-Dale coefficient for Helium ions.

Better results were achieved with a gas valve plenum pressure of 1 psig gas valve plenum pressure, providing the higher fields in the plasma and higher velocities than at the higher plenum fill pressures. B-dot data attained at this lower fill pressure is shown in Figure 73. . Note that the B-dots were 430mm from the muzzle of the gun for these data. The corresponding photodiode and interferometer data was too noisy to analyze and present. The two B-dot probes closest to the centerline show the strongest fields, showing 700G and 550G for probe 2 and probe 3, respectively. The peaks roughly correspond to peaks in the interferometry, which was taken at approximately the same axial location for these data. The beam passes between probes 2 and 3, which have a separation of 59 mm. The previously measured value of seed field in the breech is 300 Gauss for these magnetized runs from a magnet charge voltage of 60V. The gun was fired at a main PFN capacitor bank voltage of 4.5kV and gas valve capacitor bank voltage of 4.8kV, with a 14.2ms delay relative to the magnet firing. The only other timing event during the firing sequence is the delay between the firing of the gas valve and the main capacitor bank, which was 200μs here. These settings were found to give the best results with this magnet configuration.

When fired without the magnet, the B-dots still measure some field in the plasma jet, as shown in Figure 74. Significant field is still seen, but much less than when fired with the magnet. Again, relative timing of peaks matches interferometry well. It is notable that these signals are much longer in time than the seed field case. More photodiode data for velocimetry was needed to see if the plasma was longer or just slower, though the initial arrival times were the same between the two cases, suggesting the former.

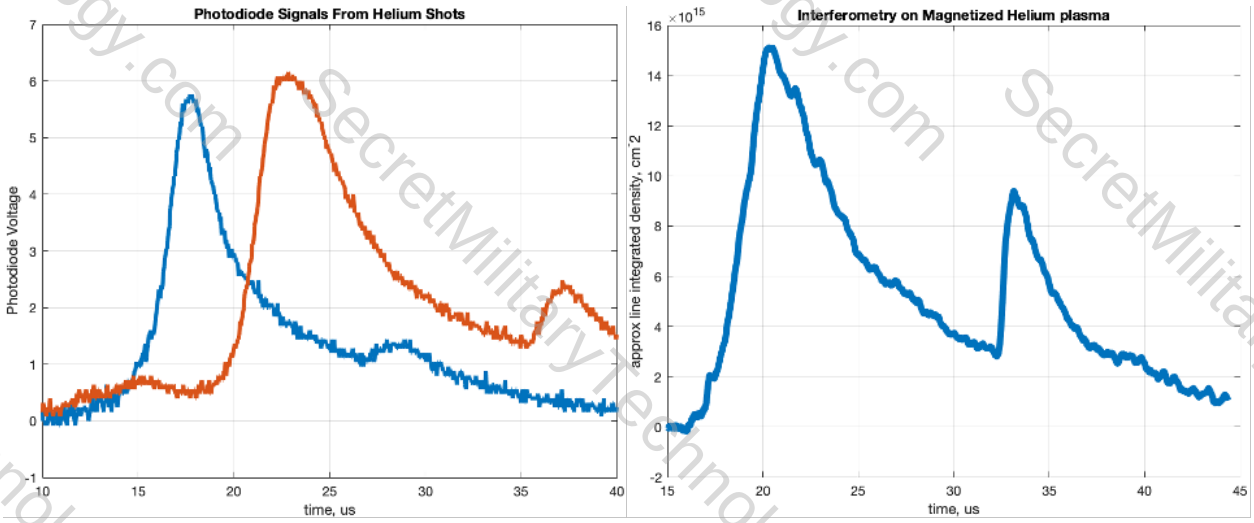

Figure 72 *First results from Helium plasmas with 8-turn magnet coil, 60V magnet charge, 14.2ms magnet to gas valve delay and 200μs gas valve to main bank delay. (Top-Left) Photodiode signals showing velocity of 40km/s for 27psig gas valve plenum pressure. (Top-Right) Corresponding interferometry, similar in shape to what is seen with Argon plasmas.*

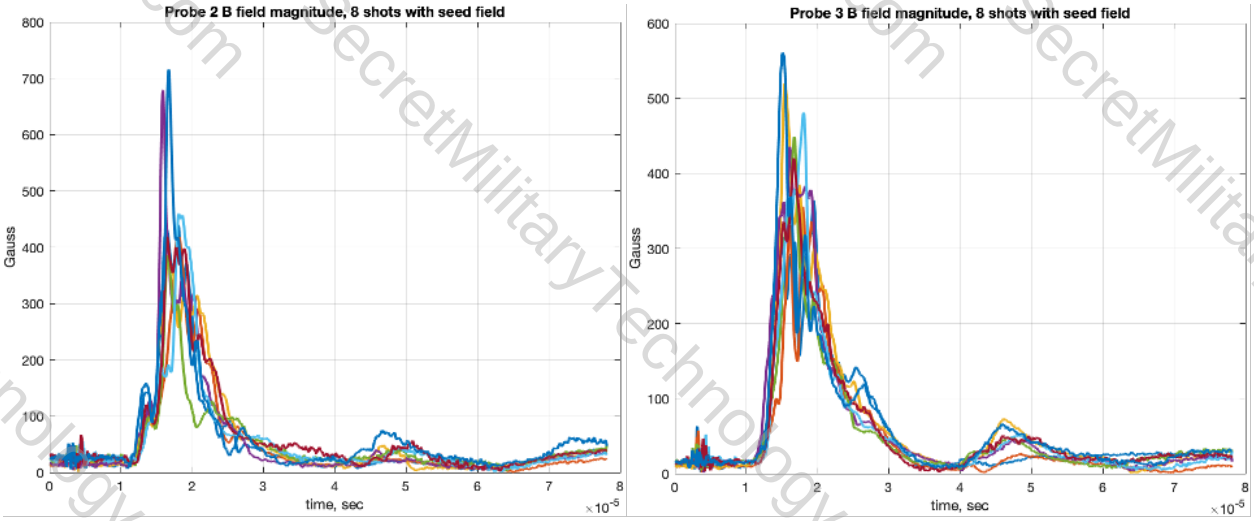

Figure 73 *First results from Helium plasmas with 8-turn magnet coil, 60V magnet charge, 14.2ms magnet to gas valve delay and 200μs gas valve to main bank delay. B-dots were 430mm from the muzzle of the gun for these data. (Top-Left) Photodiode signals showing velocity of 40km/s for 27psig gas valve plenum pressure. (Top-Right) Corresponding interferometry, similar in shape to what is seen with Argon plasmas. (Bottom-Left) B-field magnitude from B-dot probe 2. (Bottom-Right) B-field magnitude from B-dot probe 3.*

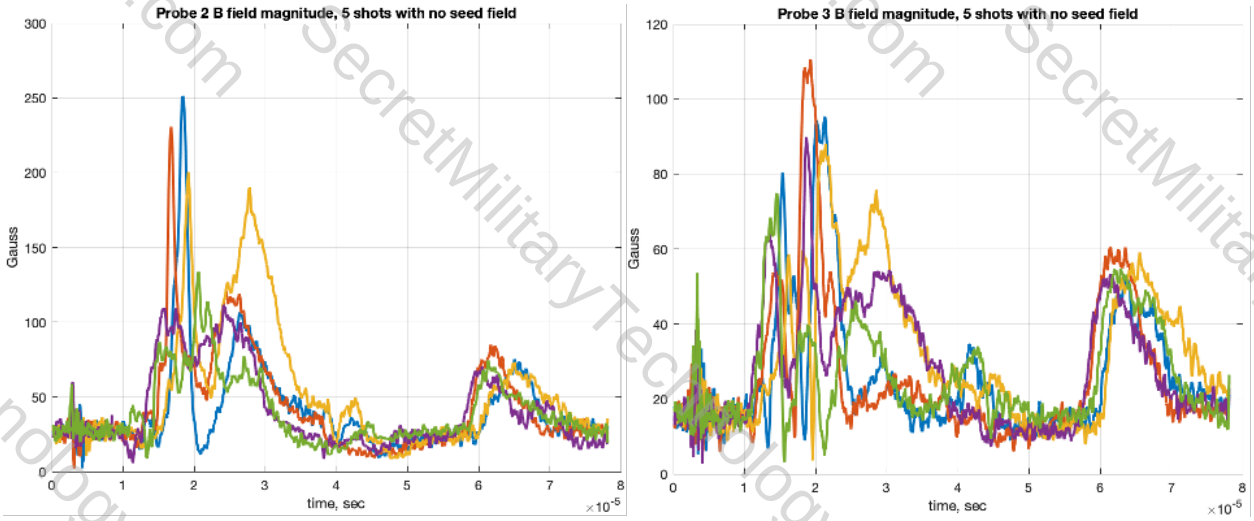

Figure 74 *B-dot signals from first Helium plasmas fired without the magnet. B-dots were 430mm from the muzzle of the gun for these data. (Left) B-field magnitude from B-dot probe 2. (Right) B-field magnitude from B-dot probe 3*

A scan was then done of measured field in the plasma versus magnet charge voltage, as shown in Figure 75. This shows a clear "turn-on" of magnetization of the plasma at a charge voltage of between 30V and 40V, and a what appears to be a quadratic rise in field after, which it should be since seed field is proportional to applied current which is proportional to the square of the voltage. The measured field magnitude on probe 2 for 20V, 30V, 40V and 50V magnet charge voltages are shown in Figure 76. Measured field results were good overall, but more field was still desired. This led to the implementation of a higher energy circuit paired with a more inductive coil.

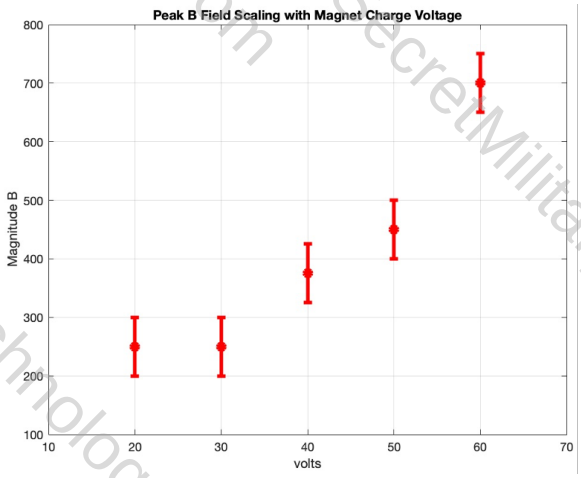

Figure 75 *B-dots were 430mm from the muzzle of the gun for these data.*

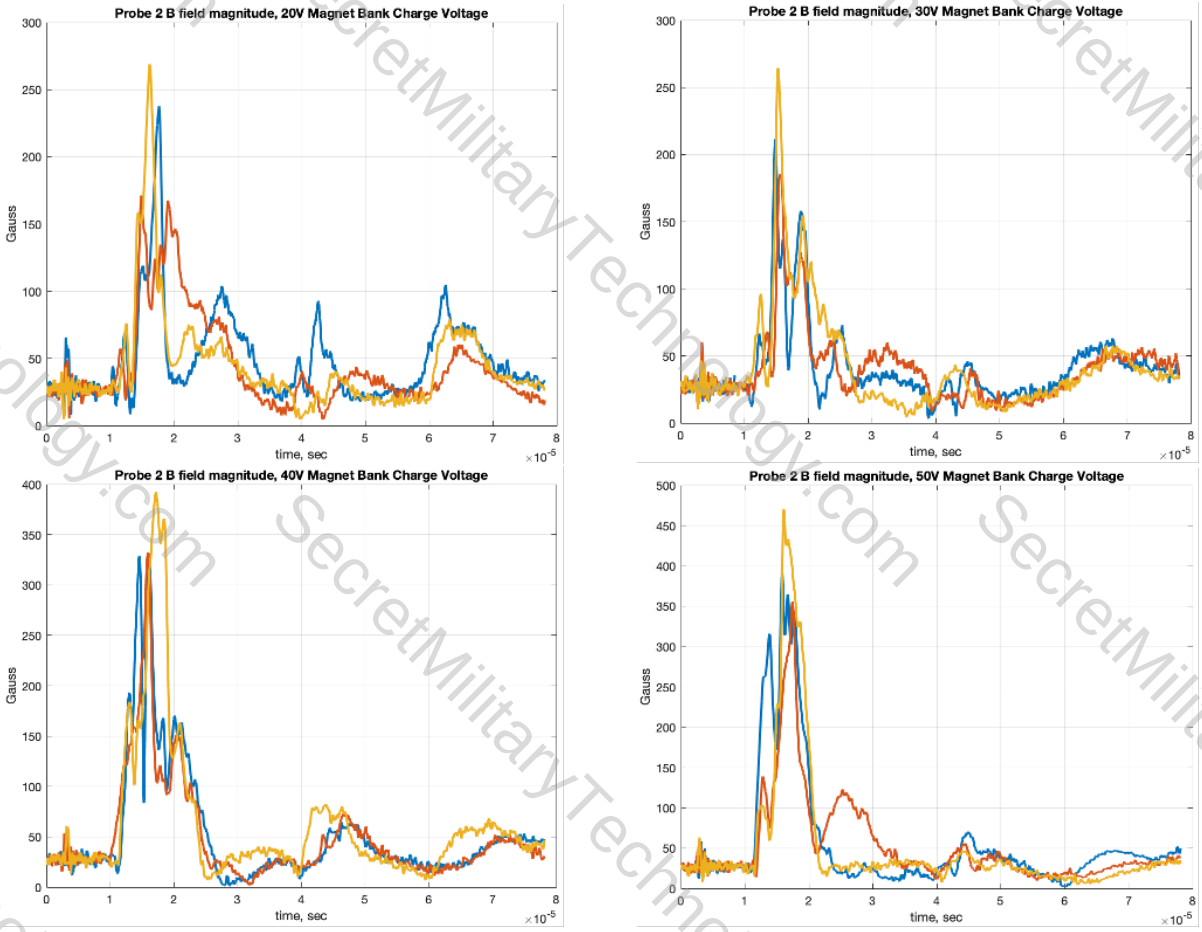

Figure 76 *Peak measured B-field in plasma at probe 2 from various magnet charge voltages. B-dots were 430mm from the muzzle of the gun for these data. (Top-left) 20V magnet charge. (Top-right) 30V magnet charge. (Bottom-left) 40V magnet charge. (Bottom-right) 50V magnet charge*

6.2 Revised Magnet Circuit and 30-Turn Magnet Coil

Note that all of the following data was taken with the B-dot probes at a distance of 800mm from the muzzle of the plasma gun or further, were as all the data above was taken with the B-dot probes at a distance of 430mm from the muzzle. The experimental campaign with magnetized plasma jets then continued with the revised magnet circuit and 30-turn magnet coil described above in Task 2 to get that much more field into the plasma. The plasma gun was again left unchanged from how it is configured for the liner guns. A magnet charge voltage of 120V was chosen as a starting point for this testing to limit mechanical stresses. This charge voltage still provides more than 3 times the seed field in the breech at 1kG than the initial circuit and coil combination did at full power, which was 300G. Scanning through the various settings led to the data shown in Figure 77 and Figure 78. Here the gun was fired with a 28ms delay relative to the magnet firing, at a main capacitor bank voltage of 4.9kV, at a gas valve capacitor bank voltage of 4.8kV, with a gas valve plenum

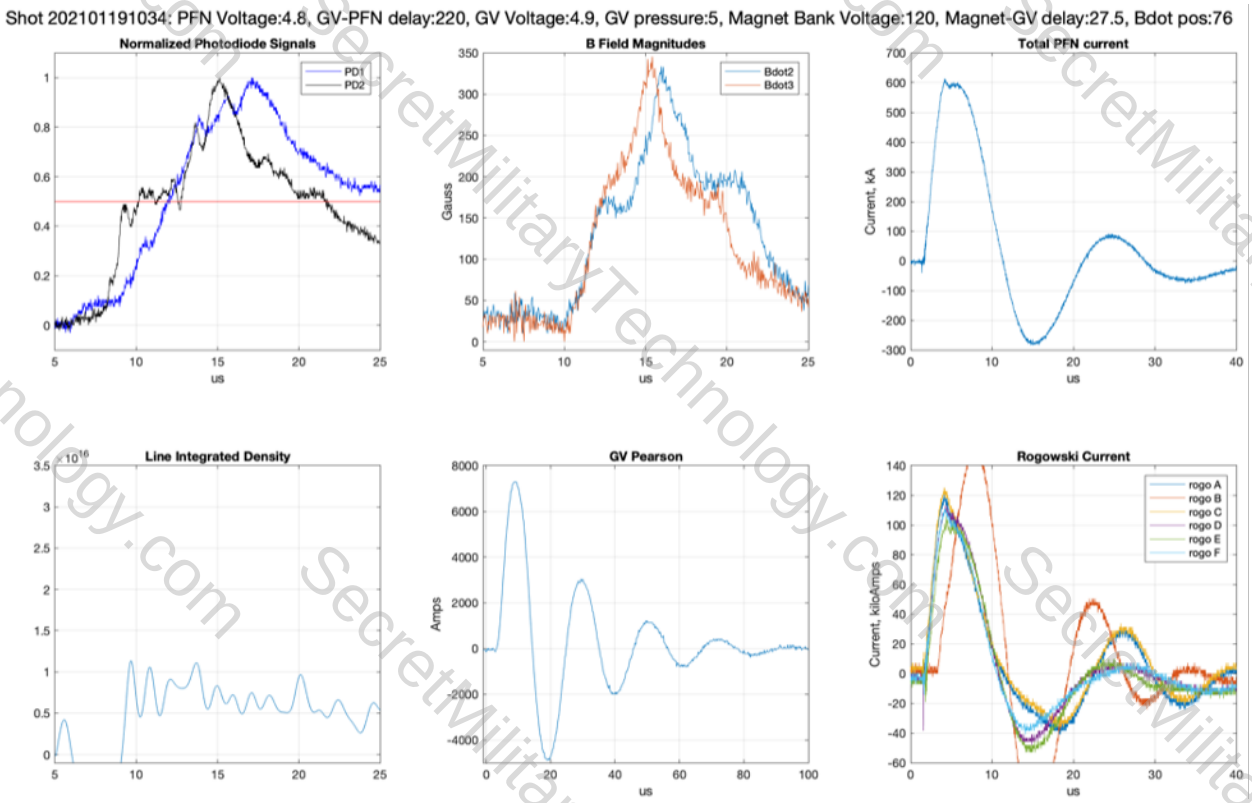

Figure 77 *Peak measured B-field with revised magnet circuit, 30-turn magnet coil, 600μF main capacitor bank and unmodified gas valve. B-dots were 800mm from the muzzle of the gun for these data.*

pressure of 5psig and with a 220μs delay between the gas valve and the main capacitor bank. Maximum observed field at the center of the vacuum chamber was as high as 350G with the new magnet configuration, as shown in Figure 77. Velocimetry proved difficult due to the large, irregular plasma jets observed from photodiodes and interferometry, shown in Figure 78, but was estimated to be in the 90km/s range. Dispensed mass measurements

also indicated that greater than $100\mu g$ of gas was being dispensed by the gas valve, which is significantly more than the $20\mu g$ minimum desired. In an effort to increase velocity and reduce mass, the main PFN capacitor bank was modified according to MACH2 simulations that indicated higher velocity was achievable with lower capacitance. This is most likely due the blowby instabilities becoming an issue at the higher peak currents provided by the higher capacitance. The gas valve was also modified to reduce its plenum volume in an effort to reduce dispensed mass for a given plenum fill pressure, while also increasing dispensed gas cloud density for a given dispensed mass.

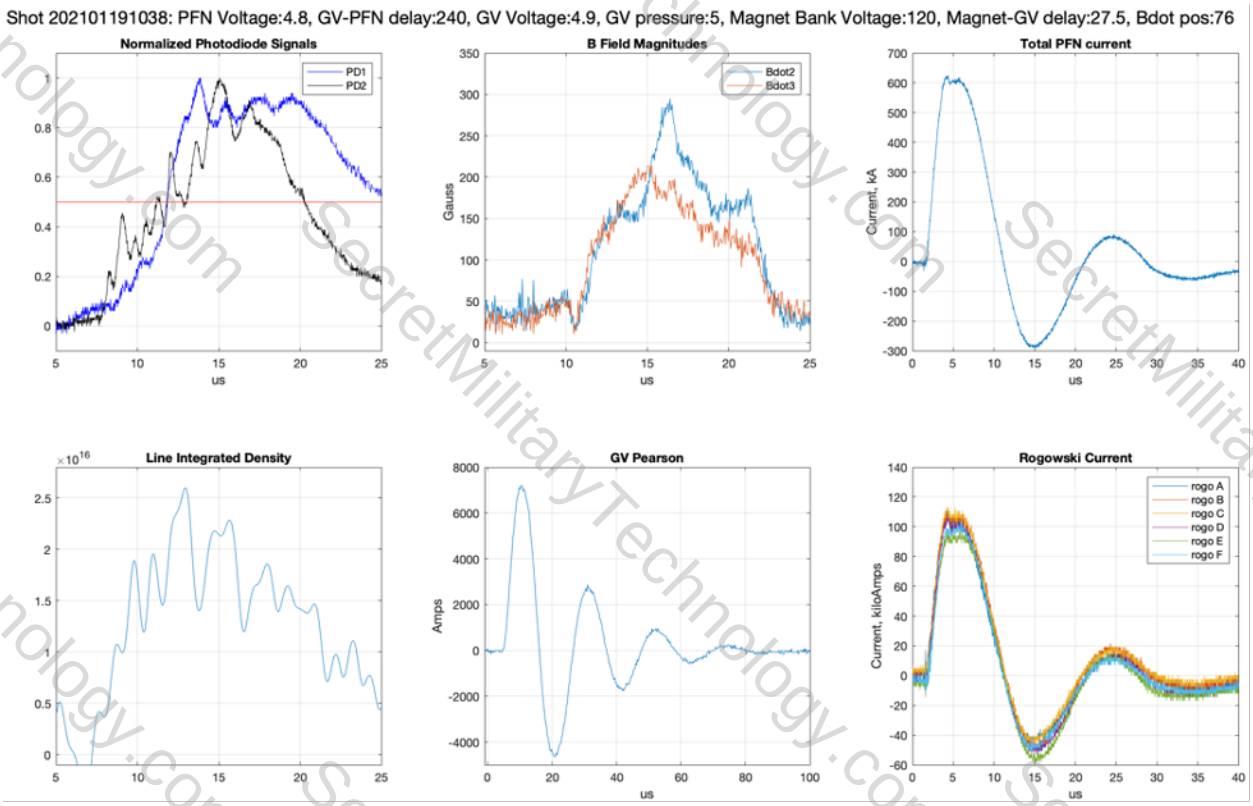

Figure 78 *Typical data with revised magnet circuit, 30-turn magnet coil, 600μF main capacitor bank and unmodified gas valve. B-dots were 800mm from the muzzle of the gun for these data.*

6.3 Modified Gas Valve and Reduced PFN Capacitance

Previous experiments seemed to indicate too much mass was being dispensed with too much current, resulting in slow jets and blowby instabilities. To resolve this, the gas valve was modified to reduce dispensed mass and capacitance was removed from the main PFN capacitor bank to reduce the peak accelerating current. Changes were made simultaneously in the interest of time.

The gas valve was modified by significantly reducing its plenum volume from 5.6cm^3 to 1.6cm^3, as shown in Figure 79, reducing dispensed mass by upwards of 70% for a given plenum fill pressure and gas valve capacitor bank charge voltage. This change worked well, allowing the gun to produce nice plasma jets at much higher fill pressures than were used in the initial experiments, so the modified valve was left in the gun for the remainder of experiments. The main PFN capacitor bank was modified by reducing it down to 200μF of capacitance, which amounted to removing 2 capacitors from each of the 6 banks of 3 caps, leaving 1 cap per bank. These changes showed immediate improvements in jet characteristics, as shown in Figure 80. Open shutter Nikon image of the magnetized Helium plasma jet striking the B-dot probes is shown in Figure 81. The photodiodes and interferometer traces are more well defined and have much sharper fronts than before, when the main capacitor bank had 600μF. Typical velocities were measured to be in the low to mid 90 km/s range based on the fronts of these signals, with a few shots exceeding 100km/s. This was achieved with a higher gas valve plenum fill pressure of 10psig Helium and shorter gas valve to main capacitor bank delay of 200μs. Longer delays produced heavier, slower plasma jets. No combination of settings was found that could consistently produce jets at or above 100km/s.

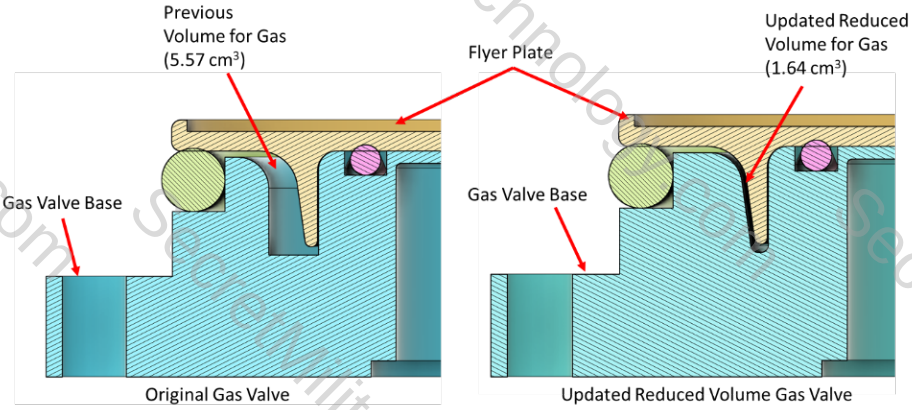

Figure 79 *Cross-sectional comparison of reduced plenum volume gas valve versus original design.*

The main PFN capacitor bank was modified again in an effort to increase velocities further. Capacitance was increased to 400μF, which was 2 capacitors per bank. This improved performance further, as shown in Figure 82. These data are from the first day of shooting with the 400μF configuration, showing an immediate and drastic improvement over previous data. Here the gun was fired with a 28ms delay relative to the magnet firing, at a main capacitor bank voltage of 4.9kV, at a gas valve capacitor bank voltage of 4.9kV, with a gas valve plenum pressure of 25psig and with a 180µs delay between the gas valve and the main capacitor bank. The longer delayed combined well with the increased capacitance,

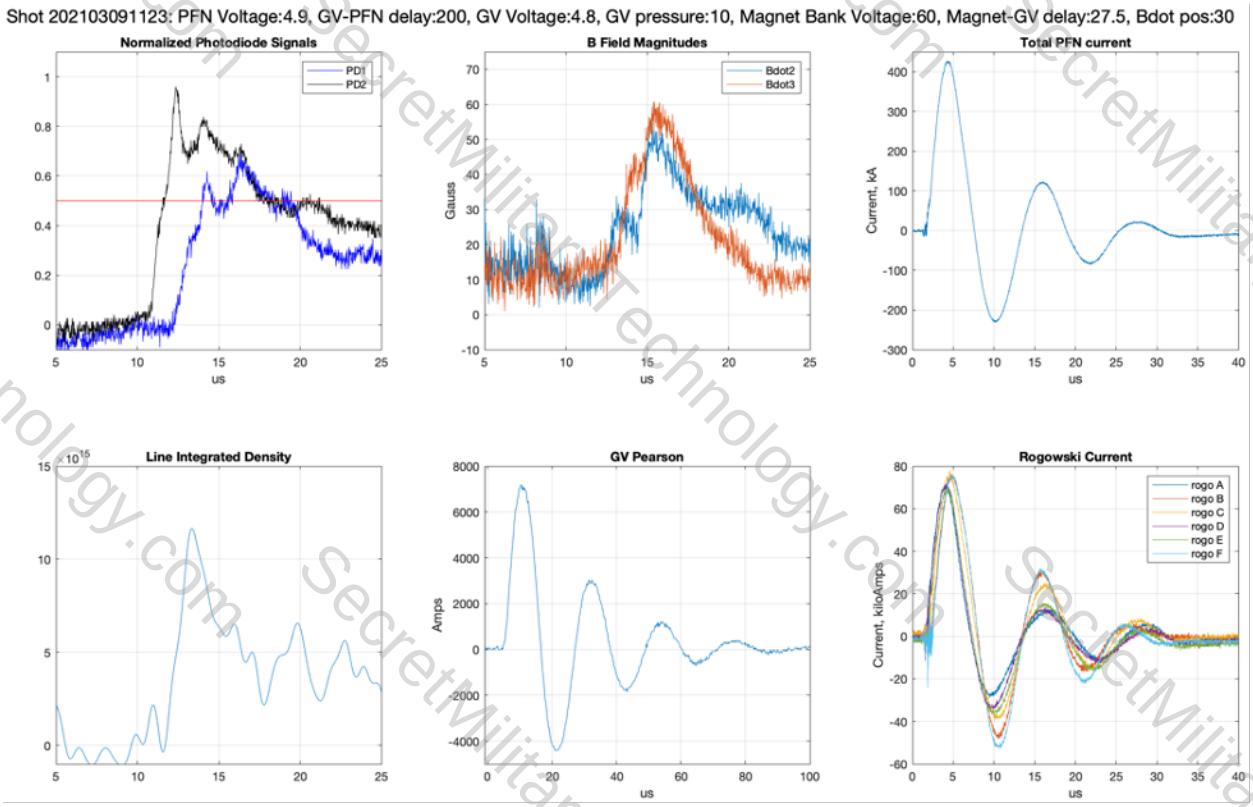

Figure 80 *Best shot from 200μF main PFN capacitor bank configuration with modified gas valve. B-dots were 800mm from the muzzle of the gun for these data*

allowing more mass to be accelerated faster, achieving a velocity of 135km/s. Along with much higher velocity, the peaks observed on the photodiode and interferometer traces were much more compact, well defined, and well correlated between the 3 diagnostics, as shown in Figure 83. Plasma jet length here was just 10cm, which is incredible. Magnetic field in the plasma was measured as ∼275G, which is not bad for a measurement at the center of the chamber. Though very good, this particular shot was not very repeatable at these settings. More investigation was required to find a group of settings that resulted in high quality magnetized plasma jets with good repeatability.

More parameter scans followed, with the greatest benefit coming from increasing the delay between the gas valve and the main capacitor bank. Better repeatability was observed once delays increased to about 250μs and above. Figure 84 shows data for a 250μs delay between the gas valve and the main capacitor bank, a main capacitor bank voltage of 4.9kV, at a gas valve capacitor bank voltage of 4.9kV and with a gas valve plenum pressure of 25psig. The resultant plasma jet had a velocity of 134km/s, jet length of 50cm, mass of 113μg, peak magnetic field of 325G and provided particularly good repeatability, as shown in Figure 85 with an overlay of 3 consecutive shots taken at the same settings. This excellent repeatability is further highlighted in Figure 86, showing a shot-to-shot jitter on the fronts of the photodiodes of less than 300ns. Repeatability was equally as impressive for the interferometry over these same 3 shots, as shown in Figure 87.

Repeatability was good at the settings described above, but length was still a bit long

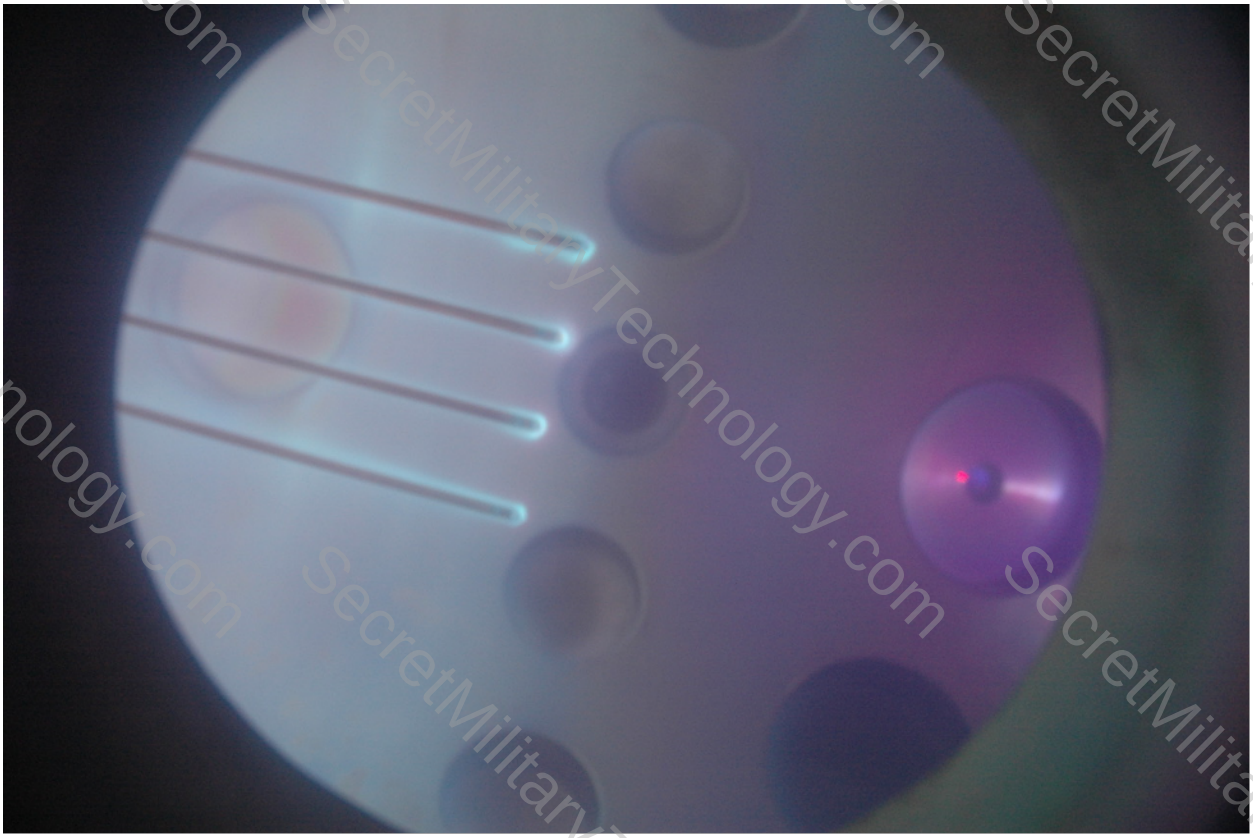

Figure 81 *Open shutter Nikon image of magnetized Helium plasma jet striking the B-dot probes from 200μF main PFN capacitor bank configuration with modified gas valve.*

at 50cm. A few more adjustments were made which allowed for more reasonable plasma jet lengths, as shown in Figure 88. For these data, there was a 240μs delay between the gas valve and the main capacitor bank, a main capacitor bank voltage of 4.9kV, at a gas valve capacitor bank voltage of 4.8kV and with a gas valve plenum pressure of 25psig. The resultant plasma jet had a velocity of 132km/s, jet length of 28cm, mass of 91μg and peak magnetic field of 203G. These jets were more compact and well correlated between the various diagnostics, as shown in Figure 89.

Length was much better at 28cm, but repeatability was not as good at the settings described immediately above. More tuning was performed to arrive at the data shown in Figure 90. For these data, there was a 275μs delay between the gas valve and the main capacitor bank, a main capacitor bank voltage of 4.9kV, at a gas valve capacitor bank voltage of 4.8kV and with a gas valve plenum pressure of 25psig. The resultant plasma jets were very high quality and showed excellent repeatability with an average velocity of 120±7.0 km/s, average jet length of 33±6.4cm and average mass of 106±13μg. A scan of the plasma magnetic field decay down the axis of the chamber was performed at these settings over the course of 15 shots, as shown in Figure 91. This showed a modest drop of 39% over a span of 200mm, implying that the plasma temperature is reasonably high. This assumption on temperature will be verified soon once the triple Langmuir probe is fully operational. The magnetic field decay scan also seemed to indicate an average field of 811G in the plasma

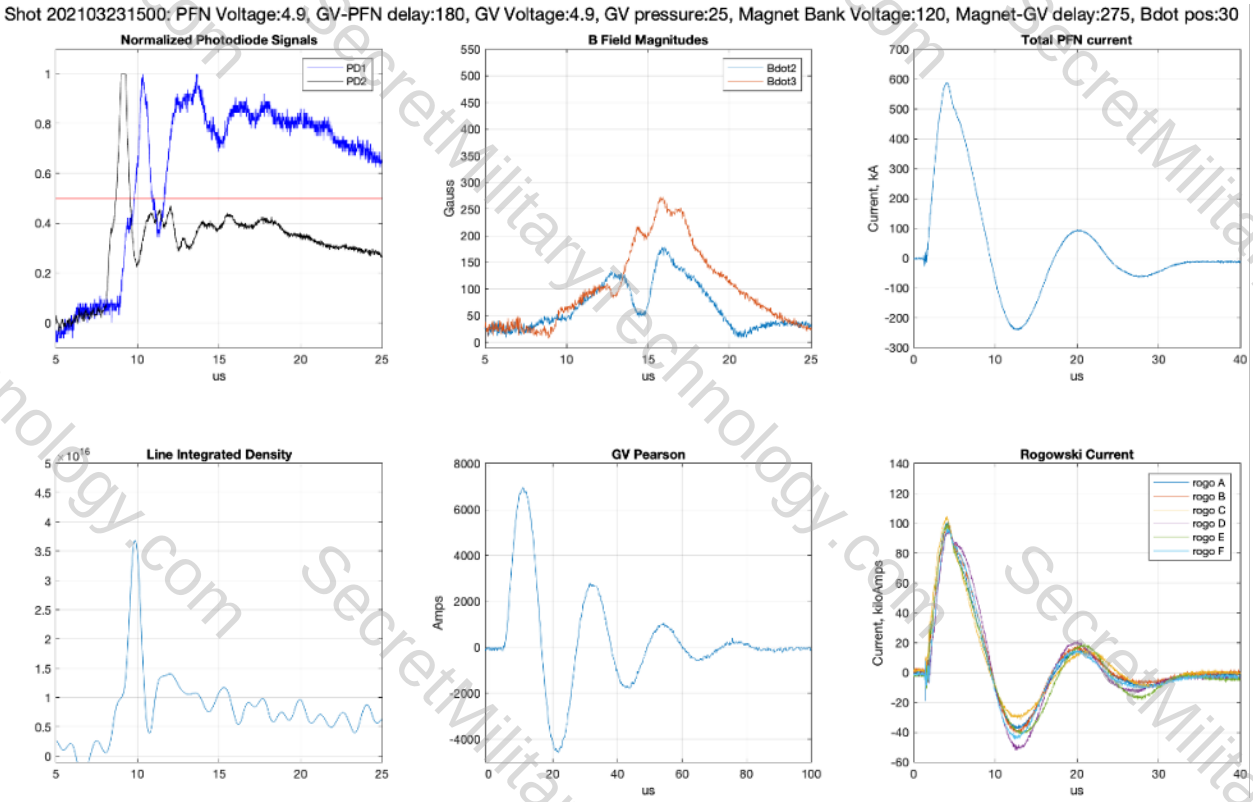

Figure 82 *Initial data from 400μμF plasma gun configuration showing excellent velocity at 135km/s, incredible plasma jet length at only 11.8cm and good magnetic field at ∼275G at the center of the chamber.*

as it exited the gun at these settings, assuming exponential decay of the field as the jet propagates the chamber. The velocity and mass of the jets over the course of the magnetic field decay scan are shown in Figure 92. Velocity shows a 5.8% variance and mass shows a 12% variance over these 15 shots at the same setting, showing excellent repeatability.

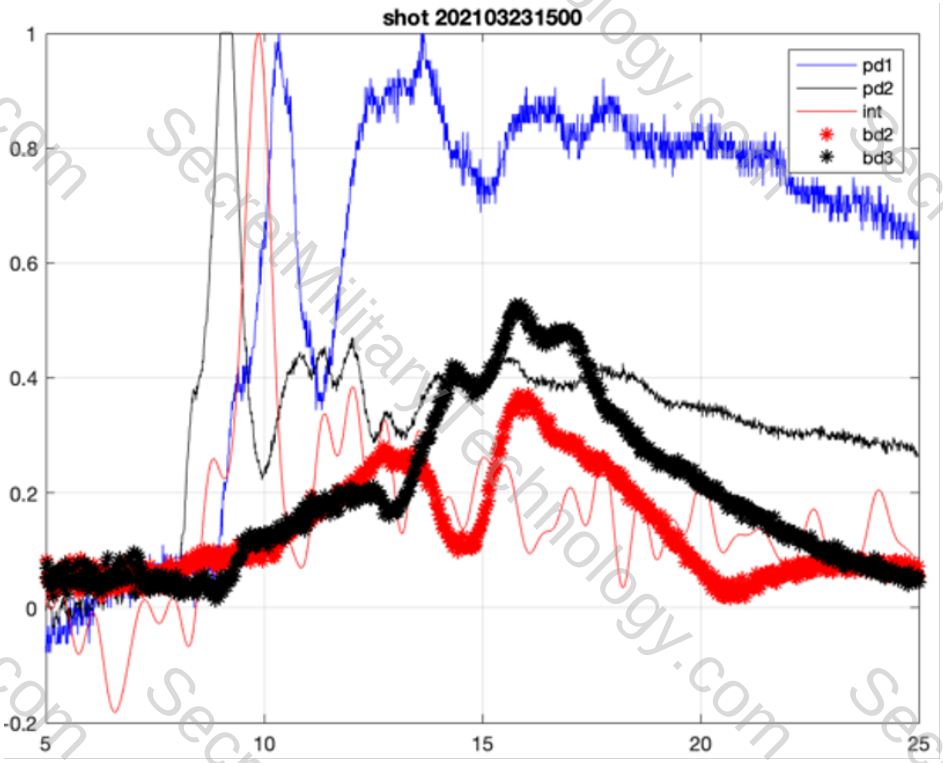

Figure 83 *Overlay of normalized photodiodes, interferometer and B-dots highlighting correlation of the plasma jet across the various diagnostics for initial data from 400μF plasma gun configuration.*

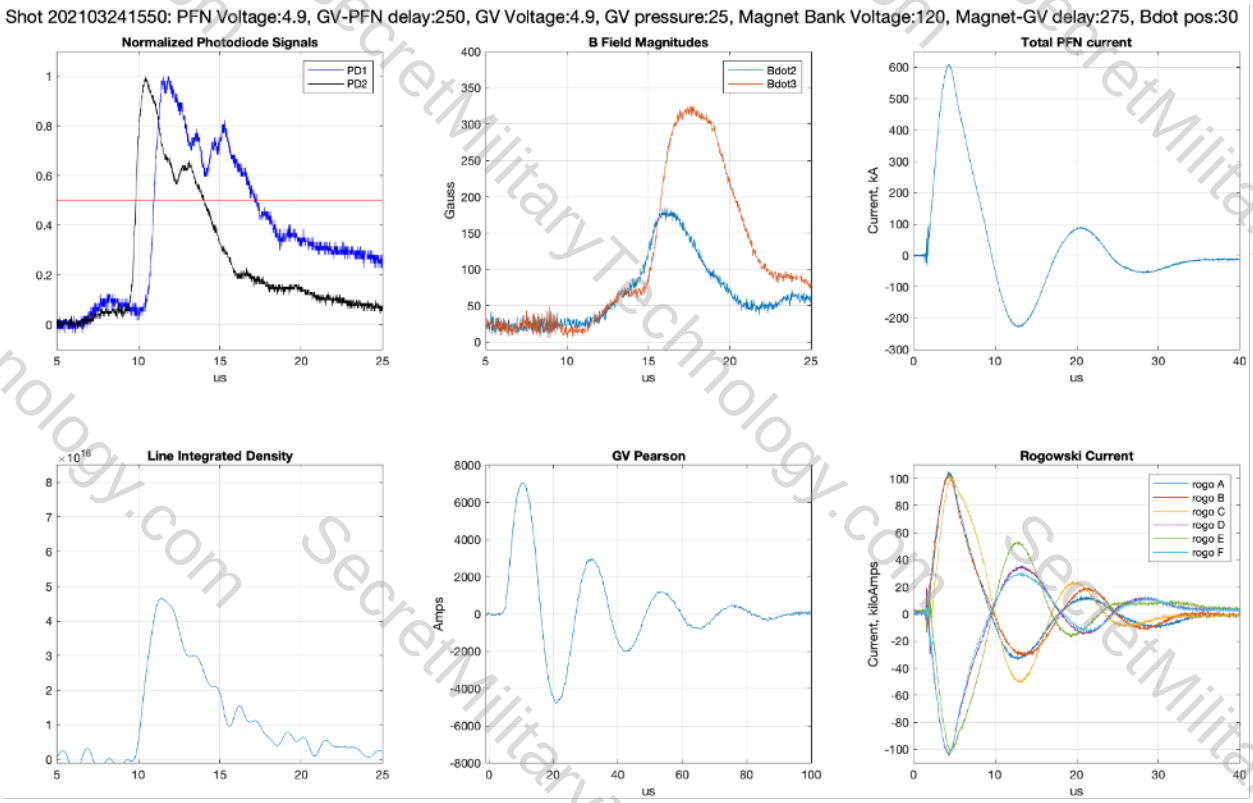

Figure 84 *Data from a 250μs delay with a velocity of 134km/s, jet length of 50cm, mass of 113μg, peak magnetic field of 325G and very good repeatability.*

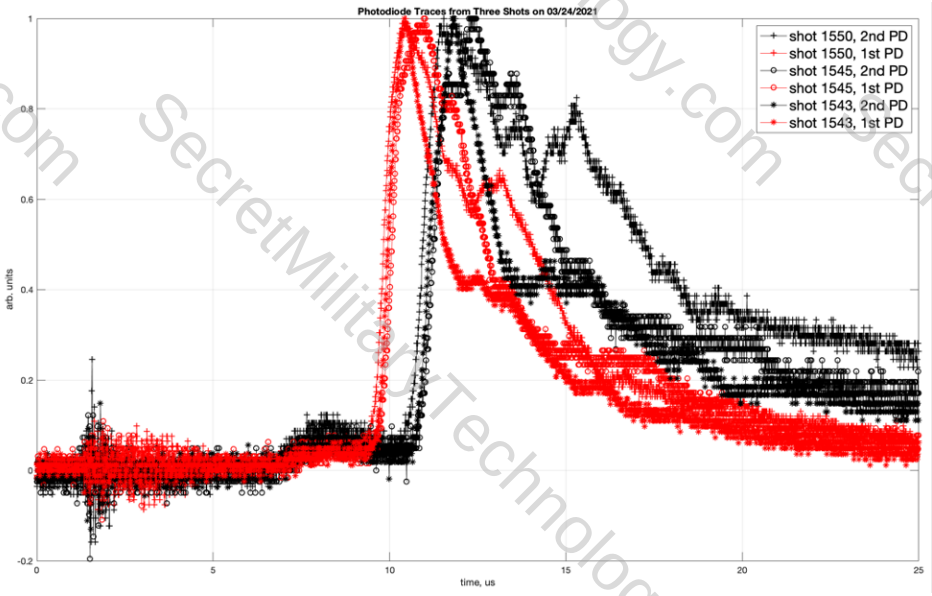

Figure 85 *Photodiode data from 3 shots taken at the same settings overlayed showing excellent shot to shot repeatability.*

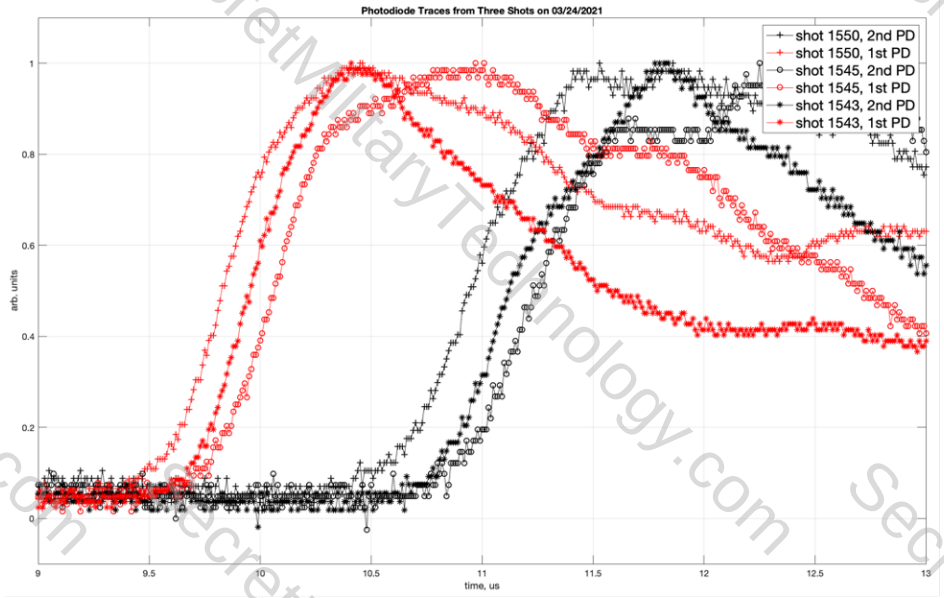

Figure 86 *Same 3 shot overlay as above on a shorter time base showing jitter of less than 300ns on the arrival fronts of the photodiode signals from one shot to the next*

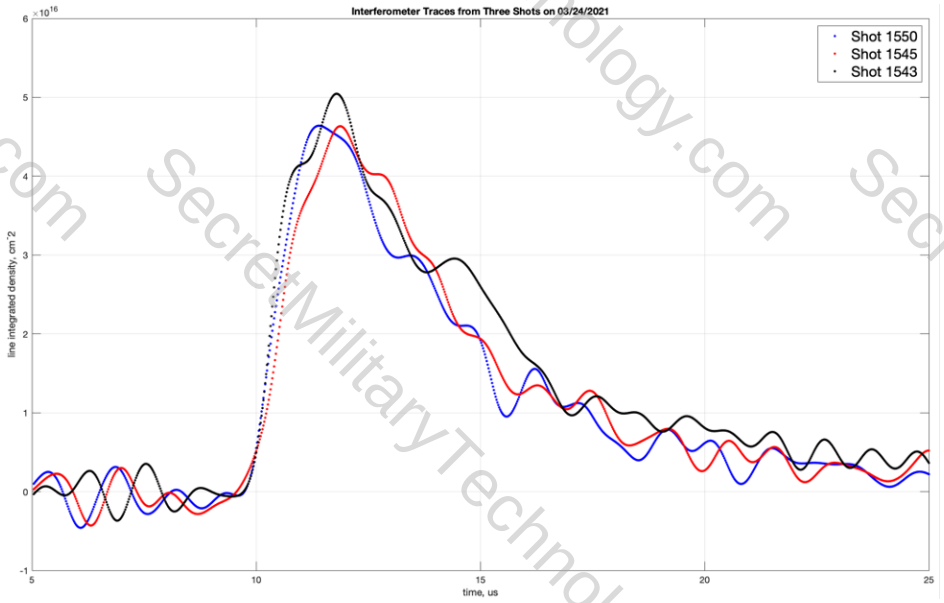

Figure 87 *Interferometry data from the same 3 shots as above overlayed showing excellent shot to shot repeatability.*

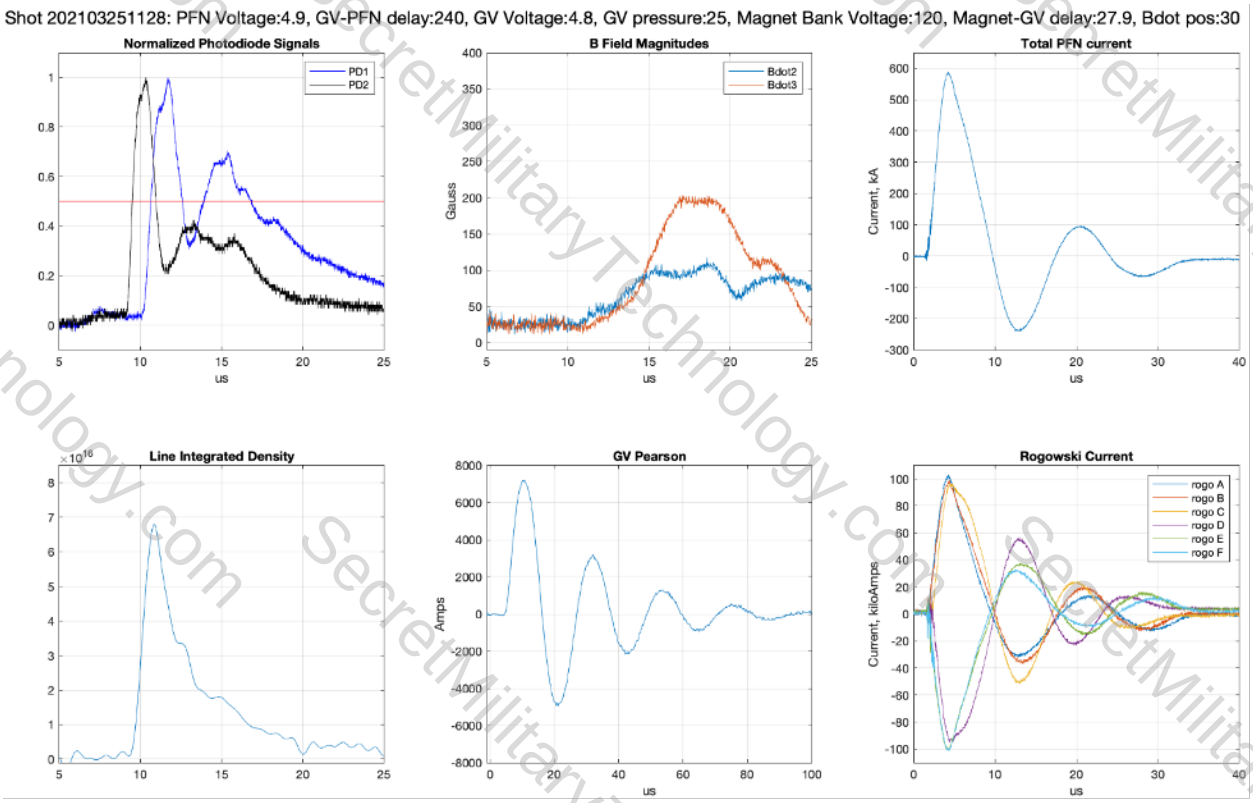

Figure 88 *Data from a 240μs delay with a velocity of 132km/s, jet length of 28cm, mass of 91μg, peak magnetic field of 203G.*

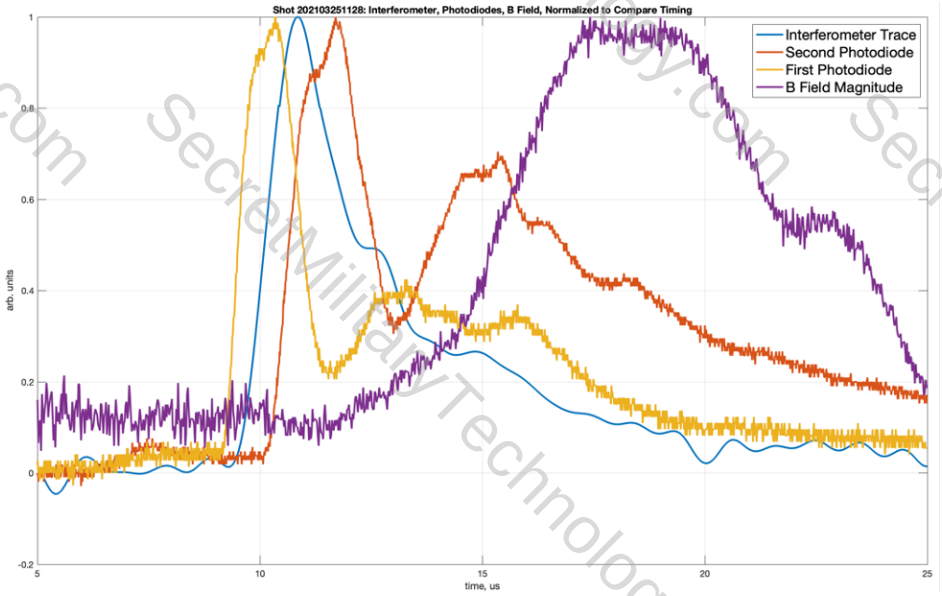

Figure 89 *Overlay of normalized photodiodes, interferometer and B-dot highlighting correlation of the plasma jet across the various diagnostics for a gas valve to main bank delay of 240μF.*

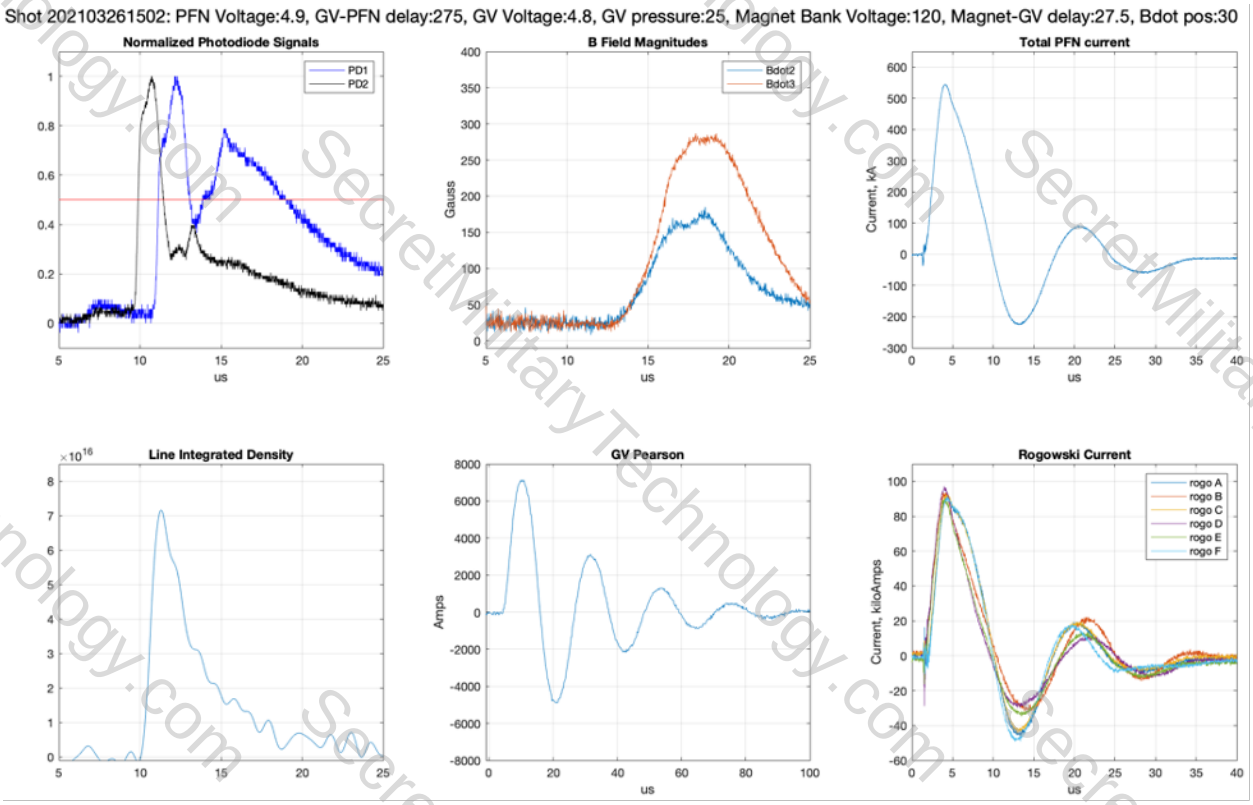

Figure 90 *Data from a 275μs delay with a velocity of 126km/s, jet length of 25cm, mass of 88μg, peak magnetic field of 275G and excellent repeatability.*

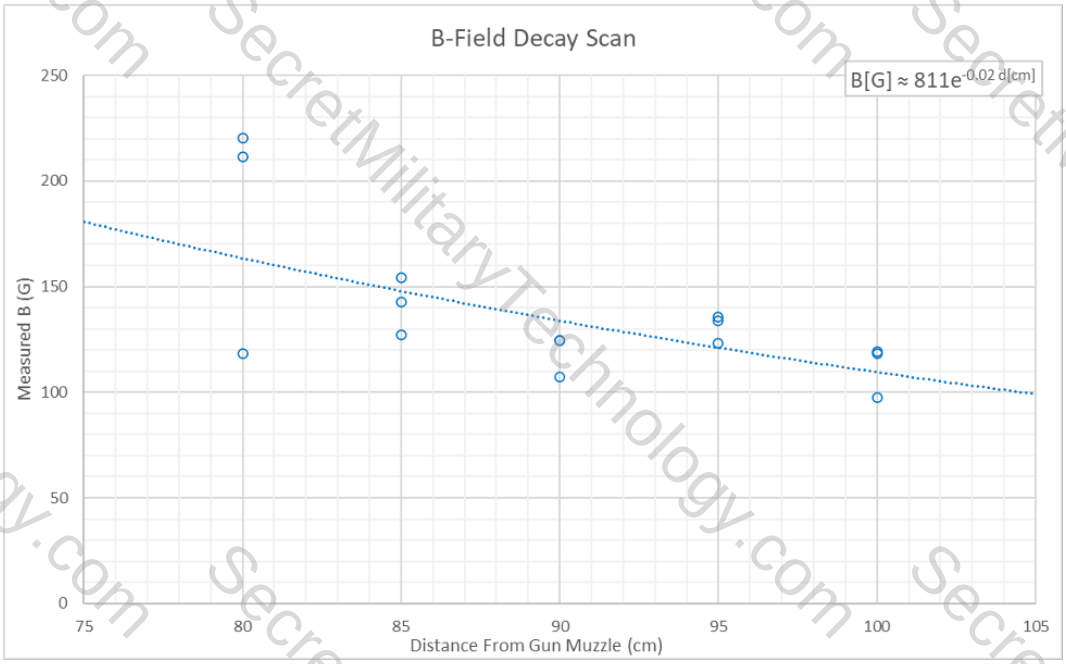

Figure 91 *Magnetic field decay scan performed down axis of vacuum chamber. Indicates a peak field of 811G seeded in the plasma jet exiting the gun.*

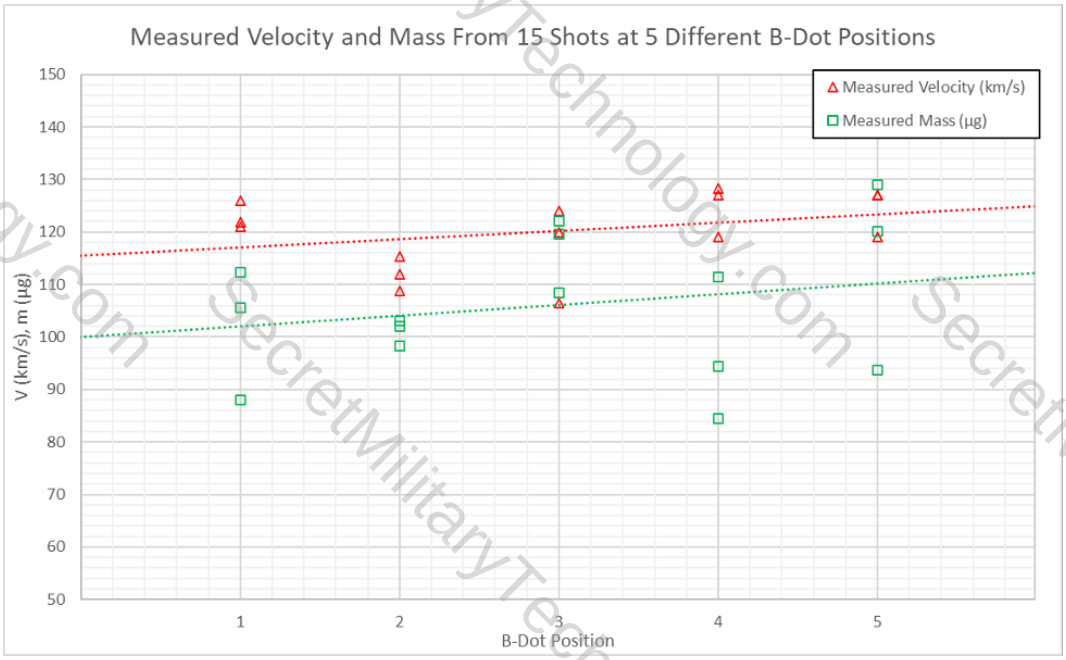

Figure 92 *Plasma jet velocity and mass over the course of the 15 shots from the B-field decay scan. Velocity shows a 5.8% variance and mass shows a 12% variance over these 15 shots at the same setting, showing excellent repeatability*

7 Summary

This effort has been an overall success. We met or exceeded almost all of the plasma jet parameters proposed, as shown in Table 2. Peak velocity and density targets were well exceeded, achieving magnetized plasma jet velocities of 135km/s and densities of $> 1.0 \times 10^{15}$cm^{-3} (line-integrated $> 8 \times 10^{16}$ cm^{-2}), which are 35% and 230% higher than the goals, respectively. Shot-to-shot repeatability is excellent, with a jitter of less than 300ns observed on the arrival fronts of the photodiode signals from one shot to the next. Average plasma jet lengths and velocities were on the order of what was desired, with an average length of 33cm traveling at an average velocity of 120km/s, but with jets as short as 11.8cm observed at velocities of 135km/s. Mass is much higher than the targeted goal, averaging 106μg per shot at repeatable settings, which is potentially very good because it means each target gun can accelerate more fuel to the desired velocity than the minimum desired. Magnetic field was somewhat lower than desired at a maximum so far of ∼811G, but not too far off the goal of 1000G. Average values, though, were typically in the 300-450G range. Work is still being done towards getting a temperature measurement, but we remain hopeful it is high based on the modest rate of decay of the magnetic field in the plasma as it propagates through the vacuum tank. Increasing the B field further and making temperature measurements will be continued on into the BETHE project where we will perform a two colliding jet experiment later in 2021.

Table 2 *Targeted parameters versus best achieved plasma parameters for target formation experiments*

		Goal	**Achieved**
Velocity	v(km/s)	> 100	> 135 km/s
Number Density	n(cm^{-3})	3.00E+14	>1.00E+15
Dispensed mass	m(μg)	20	>129
Length Scale	Lm (cm)	20	∼11.8
Magnetic Field	B(G)	1000	∼811 (typ. 300-450)*
Electron Temperature	T_i(eV)	5	not yet measured
Ion Temperature	T_i(eV)	5	not yet measured

*The 811G value was measured at the location of the interferometer, while the typical values are measured further downstream.

Despite the rough start to this project due to the pandemic lockdown, careful planning and extensive remote team work, along with generally good results along the way, allowed us to still meet the original proposed schedule. This began with the modeling effort that informed us to reconfigure the magnet coil from what was originally proposed, as well as providing guidance for modifications to the main PFN capacitor bank. EMS was used for electromagnetic modeling of the coil which indicated that it was best placed around the aluminum tubes of the gun transmission line, rather than around the chamber port as originally proposed. This allowed for more field in the breech for a given applied magnetic field and much better flux linkage between gun electrodes. An 8-turn coil was initially analyzed, but a 30-turn coil was ultimately implemented. The 30-turn coil allowed for a longer pulse, which was necessary to allow for enough magnetic diffusion time for a reasonable

amount of field to enter the breech. The longer pulse also helped to reduce mechanical stresses by having lower dB/dt. That being said, EMS indicated that magnetic forces were still fairly high, requiring significant reinforcement be applied to the coil during manufacturing to ensure safe operation. MACH2 modeling of the gun was performed as well, which indicated that less capacitance in the main capacitor bank could potentially provide improved plasma jet velocities due to better matching of the current to the plasma mass. This proved true, as testing with a $400\mu F$ bank provided markedly improved performance versus the original $600\mu F$ configuration of the liner guns.

Much care was placed in the diagnostics to ensure quality measurements while maintaining flexible diagnostic components. The optical diagnostics of photodiodes and interferometer were vital for velocimetry and mass measurements. Both were upgraded significantly for this project for improved precision and ease of use. The modular diagnostic fork system is newly developed for this program and used for both plasma magnetic field and plasma temperature measurements. The modular design of its head assembly allowed for a convenient diagnostic capable of both tasks by accepting both B-dot probes and triple Langmuir probes. Multiple probe locations allowed for sampling of the magnetic field or temperature at multiple points along the radius of the plasma jet. The rod seal assembly allowed for these measurements to be sampled along the entire axis of the vacuum chamber by allowing the head assembly to be linearly translated back and forth without affecting the vacuum pressure. The B-dot probes were used extensively, but the backend circuit for the triple Langmuir probe is still under construction and will be completed in the follow on BETHE project.

Final testing showed excellent results, with better than expected velocities and densities, as well as good plasma jet lengths and reasonable magnetic field values. This is encouraging for the BETHE project using the magnetized jet system developed in this SEED program. The 30-turn magnet coil with 25kJ magnet circuit paired well with the slightly modified version of the liner plasma guns developed during the ALPHA program, providing significant headroom in magnetic field for potential future experiments. For the plasma gun itself, with the 30-turn magnet coil installed, a 70% reduction in gas valve plenum volume and 33% reduction in main PFN capacitance was all that was necessary to allow it to provide dense, high velocity, well magnetized plasma jets that satisfactorily met the goals of this SEED program. Testing with hydrogen is now underway in the BETHE project.

8 Acknowledgments

We would like to thank Dr. Robert Ledoux and Dr. Colleen Nehl for many programmatic and technical discussions that helped to make this project a success. We appreciate their intense interest and support of this project. We would also especially like to acknowledge and thank Dr. Samuel Langendorf PI of the BETHE project at Los Alamos National Laboratory, who has been instrumental in keeping us focused and encouraging us onwards during a difficult year. His technical insights and advice have been extremely helpful during weekly and other Zoom meetings. Finally, we would like to thank ARPA-E for its financial support of this project.

References

[1] Thio, Y. F., Hsu, S. C., Witherspoon, F. D., Cruz, E., Case, A., Langendorf, S., et al. & Stoltz, P. (2019). Plasma-Jet-Driven Magneto-Inertial Fusion. Fusion Science and Technology, 1-18.

[2] Hsu, S. C., Awe, T. J., Brockington, S., Case, A., Cassibry, J. T., Kagan, G., et al. & Witherspoon, F. D. (2012). Spherically imploding plasma liners as a standoff driver for magnetoinertial fusion. IEEE transactions on plasma science, 40(5), 1287-1298.3)

[3] Hsu, S. C., Langendorf, S. J., Yates, K. C., Dunn, J. P., Brockington, S., Case, A., et al. & Samulyak, R. (2017). Experiment to form and characterize a section of a spherically imploding plasma liner. IEEE Transactions on Plasma Science, 46(6), 1951-1961.

[4] Langendorf, S. J., Yates, K. C., Hsu, S. C., Thoma, C., & Gilmore, M. (2018). Experimental Measurements of Ion Heating in Collisional Plasma Shocks and Interpenetrating Supersonic Plasma Flows. Physical review letters, 121(18), 185001.

[5] Zylstra, A. B., Yi, S. A., Haines, B. M., Olson, R. E., Leeper, R. J., Braun, T., et al. & Bhandarkar, S. (2018). Variable convergence liquid layer implosions on the National Ignition Facility. Physics of Plasmas, 25(5), 056304.

[6] Gomez, M. R., Slutz, S. A., Sefkow, A. B., Hahn, K. D., Hansen, S. B., Knapp, P. F., et al. & Jennings, C. A. (2015). Demonstration of thermonuclear conditions in magnetized liner inertial fusion experiments. Physics of Plasmas, 22(5), 056306.

[7] Hsu, S. C., & Langendorf, S. J. (2019). Magnetized plasma target for plasma-jet-driven magneto-inertial fusion. Journal of Fusion Energy, 38(1), 182-198.

[8] Hsu, S. C., & Bellan, P. M. (2005). On the jets, kinks, and spheromaks formed by a planar magnetized coaxial gun. Physics of plasmas, 12(3), 032103.

[9] Brown, M. R., & Bellan, P. M. (1990). Spheromak injection into a tokamak. Physics of Fluids B: Plasma Physics, 2(6), 1306-1310.

[10] S. Li, H. Li, (2003). A modern code for solving magneto-hydrodynamic equations. LA-UR-03-8926

[11] Degnan, J.H. et al, "Compact toroid formation, compression, and acceleration," Physics of Fluids B: Plasma Physics 5, 2938 (1993).

[12] Matsumoto, T. et al., "Development of a magnetized coaxial plasma gun for compact toroid injection into the C-2 field-reversed configuration device," Rev of Sci Instruments 87, 053512 (2016).

[13] Bellan, P.M., Spheromaks: A Practical Application of Magnetohydrodynamic Dynamos and Plasma Self-Organzation, Imperial College Press (2000).

[14] Michael H. Frese, MACH2: A two-dimensional magnetohydrodynamic simulation code for complex experimental configurations. Technical Report AMRC-R-874, Mission Research Corporation, 1987.